2017

NOVEL METHODS FOR QUANTIFYING SPATIO-TEMPORAL CHANGE IN GLACIATED AND SUBAQUEOUS ENVIRONMENTS

Jordan Mertes
Michigan Technological University, jrmertes@mtu.edu

NOVEL METHODS FOR QUANTIFYING SPATIO-TEMPORAL CHANGE IN GLACIATED AND SUBAQUEOUS ENVIRONMENTS

By

Jordan Robert Mertes

A DISSERTATION

Submitted in partial fulfillment of the requirements for the degree of

DOCTOR OF PHILOSOPHY

In Geology

MICHIGAN TECHNOLOGICAL UNIVERSITY

2017

This dissertation has been approved in partial fulfillment of the requirements for the Degree of DOCTOR OF PHILOSOPHY in Geology.

Department of Geological/Mining Engineering and Sciences

Dissertation Advisor:	*Dr. Jason D. Gulley*
Committee Member:	*Dr. Yushin Ahn*
Committee Member:	*Dr. John S. Gierke*
Committee Member:	*Dr. Thomas Oommen*
Department Chair:	*Dr. John S. Gierke*

This PhD work has been done in conjunction with Michigan Technological University's Department of Geological Mining and Engineering Sciences

Michigan Technological University

And the University Centre in Svalbard's Department of Arctic Geology

UNIS

Table of Contents

List of Figures

List of Tables

Preface

Chapter 1, “Evaluation of Structure from Motion Software to Create 3D Models of Late Nineteenth Century Great Lakes Shipwrecks Using Archival Diver-Acquired Video Surveys,” which was published in the *Journal of Maritime Archaeology* on October 15, 2014 (DOI: 10.1007/s11457-014-9132-x). The authors of this article are Jordan R. Mertes, Dr. Jason D. Gulley and Tamara L. Thomsen. My contribution to this papers was as primary investigator and main author. Dr. Gulley supervised my work and aided in manuscript writing and development. Tamara Thomsen took part in manuscript development and contributed imagery from surveys as well as background information pertaining to the acquisition of imagery and the history of the shipwrecks.

Chapter 2, “Rapid, Quantitative Assessment of Submerged Cultural Resource Degradation Using Repeat Video Surveys and Structure from Motion,” which was submitted to the *Journal of Maritime Archaeology* on October 24, 2016 and is currently under review. The authors of this article are Jordan R. Mertes, Dr. Jason D. Gulley, Caitlin N. Zant and Tamara L. Thomsen. My contribution to this paper was as primary investigator and lead author of the manuscript. Dr. Gulley supervised my work and contributed to manuscript development. Caitlin Zant and Tamara Thomsen performed the field data acquisition and aided in manuscript development by providing vital background information on the shipwreck and archaeological information.

Chapter 3, “Using Structure from Motion to create DEMs and Orthoimagery from Historical Terrestrial and Oblique Aerial Imagery,” which was submitted to the journal

Earth Surface Processes and Landforms on October 24, 2016 and is currently under review. The authors of this article are Jordan R. Mertes, Dr. Jason D. Gulley, Prof. Douglas I. Benn, Dr. Sarah S. Thompson and Dr. Lindsey I. Nicholson. My contribution to this paper was as primary investigator and lead author of the manuscript. Dr. Gulley and Prof. Benn supervised my work and both contributed to manuscript development. Dr. Thompson contributed to manuscript development and analysis. Dr. Nicholson contributed satellite imagery used for analysis as well as aided in manuscript development.

Chapter 4, "A Conceptual Model of Supraglacial Lake Formation on Debris-covered Glaciers Based on GPR Facies Analysis," which was published in the journal *Earth Surface Processes and Landforms* on October 19, 2016 (DOI: 10.1002/esp.4068). The authors of this article are Jordan R. Mertes, Dr. Sarah S. Thompson, Dr. Adam D. Booth, Dr. Jason D. Gulley and Prof. Douglas I. Benn. My contribution to this paper was as primary author & investigator. I collecting the field data, performed an analysis, assisted by Dr. Booth, and was the leading author of the manuscript. Dr. Thompson contributed to field data collection as well as manuscript development. Dr. Booth assisted in GPR data analysis and manuscript development. Dr. Gulley and Prof. Benn supervised my work and both contributed to manuscript development.

Acknowledgements

I would like to thank Michigan Technological University for providing funding for this research and for the awarded Fall Finishing Fellowship, without the support of both, this work would have never been possible. I would also like to thank the GMES department for supporting me while at MTU and while abroad working at the University Centre in Svalbard or on field work. The ability to be mobile has aided this research immensely and I thank the department chair Dr. Gierke as well as Amie Ledgerwood, Kelly McLean, Brittany Buschell, and Debra Charlesworth for helping this happen.

To the staff, administration and logistics department of the University Centre in Svalbard I must say Ti Tusen Takk for all of the support over the years. My time there will never be forgotten and neither will the people who make doing what we all do enjoyable and stimulating. Thank you to Venke, Berit, Klas, Fred, Lars Frode, Petre, Kjell Ivar, Sara, Wes, Lis, Chris, Lena, Graham, Heidi, Olafur, Nick, Penny, etc etc the list could go on forever.

A big thank you to the Gulley Research Group of MTU, specifically Charlie, Chuck and Toni. Your friendship and support while at MTU helped me get over many hurdles of doing a PhD. Charlie, your strong coffee kept me awake through most days (and nights), Chuck your never-ending optimism and upbeat personality never failed to pull me out of whatever slump I was in, and Toni, thanks for always breaking down and crying about your thesis work, at least I knew I wasn't the worst off.

I would also like to thank those friends I've made along the way who are not in academia. Specifically, all those "usual suspects" at the KBC and Puben. It meant a lot to me to be able to sit back, relax, have a pint or two and talk about everything not related to my work.

Mostly I would like to thank my family for always being supportive of this endeavor, for always encouraging me to pursue my dreams and for always calling on skype to check in. To my mother and fathers, I love you very much. To my wife, who has had the unfortunately opportunity of dealing with me during my PHD years, I love you and I would like to say thank you and of course sorry. To the rest of you, from now on you can all refer to me as "The Doctor".

Jason, Doug and Sarah, thank you for all your help. Thank you for believing in me. I hope we continue to work together while exploring the world of glaciers and all things interesting.

Abstract

In many scientific fields, it is important to actively develop new approaches to monitoring and quantifying changes within different systems. Often adapting existing tools or applying techniques from alternative fields can greatly improve our ability to monitor spatial and temporal changes. In this dissertation, I present four studies aimed at demonstrating new innovative ways at improving our ability to observe and quantify changes occurring on glaciers, submerged cultural resources (SCRs) and supraglacial lakes by using technology such as Structure from Motion + Multi-view stereo photogrammetry (SfM) and ground penetrating radar (GPR) surveying combined with facies analysis.

I have successfully reconstructed highly detailed 3D models of multiple large scale SCRs including the *Home*, *Hetty Taylor* and the *Wisconsin* using archival and newly acquired diver video footage. Comparison of digital measurement versus *in situ* measurements show low percent errors for most measurements, ranging from <1- 11% with only a few falling outside this range, verifying that the application to these data has been successful. A secondary survey was carried out on the *Wisconsin* in order to generate two models, one from 2006 and one from 2015. Differencing the digital elevation models has allowed us to quantify and map the spatial distribution of changes occurring through site degradation. In addition, comparison of the orthomosaics has allowed for the visual identification of changes occurring at the SCR such as disappearance of objects, shifting of material and increased colonization of mussels.

I have also applied the SfM technique to historical imagery of glaciers in the high-arctic, European Alps and the Himalaya in order to extract spatial information for periods where it may not exist or is limited in resolution. The digital elevation models extracted are of a high-resolution and have allowed for very detailed spatial change mapping. The SfM process was performed without *a priori* information and relied on GCP obtained from more recent high-resolution remote sensing datasets. Results show highly contrasting patterns of long term melt on both a regional and local scale.

Lastly, I have used GPR surveying techniques on the frozen Spillway Lake, Ngozumpa glacier, Nepal, in order to improve our understanding of the supraglacial lake subaqueous environment. These surveys have allowed for the extraction of high-resolution bathymetric data as well as detailed information pertaining to lakebed debris distribution. Identification of two specific radar signal facies and observations of near shore sediment structures have allowed for the creation of a new updated conceptual model of supraglacial lake development, incorporating not only lateral expansion, but also deepening processes and lakebed dynamics.

Introduction

If we lived on a planet where nothing ever changed, there would be little to do. There would be nothing to figure out. There would be no impetus for science. And if we lived in an unpredictable world, where things changed in random or very complex ways, we would not be able to figure things out. But we live in an in-between universe, where things change, but according to patterns, rules, or as we call them, laws of nature. If I throw a stick up in the air, it always falls down. If the sun sets in the west, it always rises again the next morning in the east. And so it becomes possible to figure things out. We can do science, and with it we can improve our lives.

— Carl Sagan

Cosmos

Observing, quantifying and monitoring spatio-temporal changes occurring within physical systems is an essential aspect of many scientific fields, such as: archaeology, biology, climatology, forestry, geomorphology and glaciology (Duncan et al., 2013, Fan et al., 2014, Ozainne et al., 2014, Ricevuto et al., 2014, Hölbling et al., 2016, Rabatel et al., 2016). Indeed, it is only through observations and measurements that scientists can gain a broader understanding of the active processes driving change. Logistical and economic constraints can, however, combine to limit effective observations and thus change detection. This dissertation focuses on the development and application of novel techniques to quantify change in the fields of maritime archaeology and glaciology. The primary goal of this dissertation is to demonstrate that, by taking advantage of new or improved techniques and technology, or in applying existing techniques to new applications and areas, it is possible to extend both the temporal and spatial extent of observations.

This dissertation is composed of four studies, each of which have either been published in a peer-reviewed journal or submitted for review for publication. Three of the studies in this dissertation use the technique Structure from Motion + Multi-view Stereo photogrammetry (SfM). While SfM is a relatively new technique, it has already seen extensive use in both glaciology and archaeology as a means for generating ultra-high resolution digital elevation models (DEMs) and fully 3-D models of cultural resources, using personally acquired imagery from terrestrial and aerial perspectives (Verhoeven et al., 2012, Green et al., 2014, Immerzeel et al., 2014, Ryan et al., 2015). Unlike traditional photogrammetric surveys, however, SfM does not require collection of camera position and/or orientation information for every image. Camera relative positions and orientation, as well as lens parameters can be back calculated after matching features across overlapping image pairs and determining the image perspective positions. After initial alignment, it is possible to extract more matched features and build a sparse 3-D point cloud of the object of interest using multi-view stereo algorithms (Agisoft, 2014).

Additionally, SfM can use randomly positioned imagery as long as there is enough overlap for the software to successfully match features. This aspect of SfM is highly beneficial in the field of maritime archaeology where submerged cultural resources (SCRs) often have a more elaborate 3-D form and require more flexible surveying patterns. Likewise, in the field of glaciology, where features such as ice cliffs and hummocks can be captured through a combination of nadir and oblique images, using SfM modeling can improve the overall digital representation. By limiting the requirement

for evenly spaced and overlapping imagery, it is possible to use handheld methods and even incorporate video as a means for acquiring dense imagery sets.

Using SfM in both the subaqueous environment and glacial environment can enable researchers to perform highly detailed surveys faster, thereby decreasing field time (e.g. dive time or time at altitude), reducing overall costs and limiting overall physical stress (Mertes et al., 2014). In both systems, measurements and surveys can be hindered by physical constraints on the researcher themselves, such as exposure to adverse pressures (i.e. increased pressures at depth and decreased pressures at altitude), extreme temperatures (i.e. decreased temperatures at depth and at higher altitudes or polar regions) as well as the volume of work involved in completing surveys in a given timeframe. Divers surveying SCRs have to carry their air supply, and, depending on the depth, much of their time in the water may be expended during decompression stages which increase in time as bottom time increases (Van Liew and Flynn, 2005). Conversely, working on glaciers at high altitudes means reduced oxygen supplies (e.g. ~50% less at 5500 m a.s.l than at sea level) and valuable fieldwork time must be spent acclimatizing (Peacock, 1998).

Depending on the accuracy needed in the final SFM model, as well as whether or not it is georeferenced or just scaled in a relative coordinate system, different approaches can be taken for acquiring ground control points (GCPs). Unfortunately in the subaqueous environment the use of GPS is limited due to the attenuation of electromagnetic signals through the water column (Dhanak and Xiros, 2016). Therefore, acquisition of highly precise GCPs must be done using hand measurements and the triangulation of survey

points across the wreck site. However, the triangulation of many points on larger SCRs can be a time-consuming process (Bass, 1966). Yet, it is entirely possible to identify reliable points in a model by using previously attained measurements (assuming no change), easily positioned scale bars, or from precise detailed maps, thereby limiting the time spent performing *in situ* GCP collection. In the field of glaciology, with the access to high-resolution remote sensing data becoming much easier, it is possible to also forgo field GCP collection. Instead, GCPs can be identified and measured through other sources with their positional accuracy being dependent on the data used (e.g. orthoimagery and DEMs).

As many larger SCRs are left *in situ* due to size, cost of retrieval or fragility, they remain subject to environmental and anthropogenic processes which control rates of deterioration over time (Oxley and Gregory, 2002, Edney, 2016). Managers must therefore actively monitor the SCR and could greatly aid from SfM. In a similar fashion to detecting changes over glacier surfaces, using DEMs of SCRs can help to identify areas of change by subtracting models from different time periods. Prior to SfM, archaeologists and SCR managers would need to have performed extensive repeated traditional surveys involving tape measures, plane tables and subsequent triangulation of points, to map the SCR (Bass and Katsev, 1968). Now however, managers can install stable GCPs and easily perform repeated photographic/video surveys of the SCR, allowing rapid DEM production, alignment, differencing and change detection.

Another benefit of using SfM is its ability to work with most any digital imagery that contains multiple perspectives of an area of interest. This has great potential for

extracting geometric information from archival imagery. Many early photographic surveys of SCRs and glaciers were done primarily for the purpose of recording visual information. However, in some cases, sufficient imagery may have been acquired, or film taken, to allow for extracting spatial information, even though extraction of spatial information was not the original intended purpose. With SfM it is now possible to use photo and video archives as datasets and extract the important spatial data recorded within them. These data allow us to quantify changes that have occurred since the images were first acquired, ultimately unlocking the past and helping to fill in observational gaps in the spatio-temporal record.

The use of SfM in both subaqueous and glacial systems is not however without its challenges. As the initial alignment of imagery using SfM relies primarily on identifying corresponding features within image pairs, the acquired imagery must have sufficient texture (e.g. variation in tone, illumination, contrast) for this to occur. For example, using SfM to map snow covered glaciers is often problematic due to the predominantly white, low contrast nature of the imagery. Images obtained over clean ice glaciers can provide more opportunities, given the sun angle does not create direct reflections. Imagery obtained over debris-covered glaciers, where surface cover is highly heterogeneous, can work well in the SfM workflow. However, feature extraction may not work well in shadowed regions located around larger debris clasts or on certain ice cliffs with aspects facing away from direct sunlight.

In the subaqueous environment, sunlight penetration decreases with depth and surveyors must rely on artificial light which may only illuminate features within a certain angle and

proximity. Similarly, obliquely obtained imagery of SCRs may capture not only the SCR in the foreground but also the water surface, thereby causing a large spread in brightness which can cause over or under exposure of key objects. Variations in distance to object can also cause changes in the illumination and texture of objects in the acquired imagery. On larger SCRs, sets of imagery acquired from two different distances can be difficult to align. Turbidity is one of the most difficult environmental factors to overcome when performing a SfM survey in the subaqueous environment. Little can be done to overcome this factor other than to acquire imagery from a closer distance, significantly increasing the survey time and the amount of imagery required to cover the site.

In addition to obtaining reliable imagery, another challenging aspect of SfM model generation in both systems is that of ground control and scaling. Not only does accurate ground control allow for a better self-calibration of the camera model, or internal orientation (i.e. focal length, distortion coefficients) as well as external orientation (i.e. reference system X,Y,Z, roll, pitch and yaw), but it also improves the resulting accuracy of the final model. Having good ground control thereby improves our ability to extract measurements and quantify changes. Yet, as previously mentioned, the preclusion of GPS measurements in the subaqueous system means precise positional data must be measured and trilaterated by hand which can involve multiple people and more dives. In the absence of precise GPS measurement, a more rapid way to scale models of SCRs is through the use of scale bars, or a smaller sample of known measurements which can be applied to the model.

In the glacial system, on the other hand, positional information can be obtained from GPS surveys of field sites to be mapped, or from external orientation information embedded in survey imagery. Using previously acquired imagery that does not have this type of information means it must be extracted from other data sources. For this purpose, it can still be possible to obtain ground control from more recent, high-resolution visual and spatial data sets (e.g. DEMs, orthoimages). By identifying reliable features which appear to have undergone little to no change (e.g. boulders, peaks) glacier models can be geographically positioned and co-registered to the secondary data source.

In some systems, however, the use of SfM and visual data does not work due to environmental factors that limit the use of optical techniques. For this reason, the fourth study presented in this dissertation uses ground penetrating radar (GPR) to explore the subaqueous environment of supraglacial lakes on debris-covered glaciers. GPR is used as a means of investigating inaccessible subsurface systems (e.g. rock, ice, buried ruins) as well as bathymetric mapping of freshwater lake systems (Murray et al., 1996, Neubauer et al., 2002, Pälli et al., 2002, Goodman, 2009, Singh et al., 2010, Bælum and Benn, 2011, Sambuelli and Bava, 2012, Watanabe et al., 2013, Zhao et al., 2013, Mackay et al., 2014). Bathymetry can be extracted from remote sensing imagery on lakes with low turbidity such as those found on Greenland (Sneed and Hamilton, 2007, Fitzpatrick et al., 2014). However, in regions such as Nepal where many glaciers are heavily debris-covered, the high turbidity of many lakes precludes using optical methods. Therefore, most surveys that have been previously conducted on larger supraglacial lakes were done using weighted lines or echo sounders (e.g. Kadota, 1994, Thompson et al., 2012). These

surveys can involve a substantial amount of field time often resulting in low resolution spatial information (e.g. 10s of meters between measurements). In addition, these methods reveal little about the lakebed debris distribution and makeup. The use of GPR can greatly increase the quantity and quality of spatial data collected on supraglacial lakes in a fraction of the time.

GPR relies on measuring the two-way travel time and reflectance of transmitted electromagnetic signals. Many modern GPR systems have robust “rough terrain” antennae which, when coupled with the data processor, can be easily operated by single or double person teams and used in a variety of environments. Portable GPR systems allow for rapid data acquisition with minimal effort across landscapes and frozen lake surfaces, which is key for surveys in high altitude environments. “Facies analysis”, which is a qualitative method of characterizing different styles of GPR signal reflectivity, can allow mapping consistent features having similar reflection geometry. Combined with observations of structures within the survey vicinity, it is possible to infer what the identified GPR facies may in fact be (Mertes et al., 2016). Repeated GPR surveys can therefore allow for a more detailed understanding of supraglacial lake deepening rates as well as the debris redistribution processes occurring. With the addition of common midpoint surveys, which allow for the determination of the velocity of the material being investigated, it would also be possible to easily and efficiently map lakebed debris thickness, a key parameter in modelling lake deepening rates.

By applying well-established tools such as GPR, to environments where they have seen little use, or by using more recent techniques such as SfM with archival datasets, it

becomes possible to observe and quantify spatio-temporal changes in subaqueous and glacial systems in new ways. The chapters of this dissertation use these tools and techniques to focus on important questions regarding change detection in both systems. The chapters are:

Chapter 1. *Evaluation of Structure from Motion Software to Create 3D Models of Late Nineteenth Century Great Lakes Shipwrecks Using Archival Diver-Acquired Video Surveys*, published in the Journal of Maritime Archaeology, October 15, 2014. Using the SfM technique of model building can greatly aid maritime archaeologists in overcoming many of the logistical and financial constraints of performing detailed *in situ* field surveys. While SfM has previously been used to model smaller SCR sites, the technique had not been applied to SCRs at the shipwreck scale and archived video data had not been used as an imagery source for model creation. This study addresses the question: **can archival video surveys of SCRs be used as a source of imagery in the SfM workflow to produce reliable 3D models of large shipwrecks?** Archived video imagery that was originally used to produce down-looking mosaics for scientific and public outreach reasons was used as inputs to create a spatially-registered, 3D SfM model. GCPs and other positions were gathered from a planimetric wreck map produced from detailed hand surveys. Comparison of measurements made on the SfM models with the *in-situ* surveys demonstrate that SfM could potentially be used to accelerate SCR surveys.

Chapter 2. *Rapid, Quantitative Assessment of Submerged Cultural Resource Degradation Using Repeat Video Surveys and Structure from Motion*, submitted for

review to the Journal of Maritime Archaeology October 21, 2016. As SCRs are subject to degradation from environmental and anthropogenic sources, it is crucial that managers can easily and efficiently survey and quantify degradation magnitudes, causes and patterns. This study addresses the question: **can spatio-temporal changes to a SCR be quantified using video surveys and the process of digital elevation model differencing?** In the field of glaciology DEM differencing is a common method to calculate the spatial changes occurring over a given time period. By subtracting the elevation values of a more recent DEM from those of an earlier DEM it is possible to identify areas where the glacier surface has been lowered (positive differencing values) or been raised (negative differencing values). The method can be adapted to find differences on DEMs of any surface given proper alignment. Two models of the Great Lakes shipwreck, the *S.S. Wisconsin*, were built using the SfM technique and diver-acquired video surveys that were collected approximately 10 years apart. The models were co-registered and aligned, then afterwards differenced. The final models, orthomosaics and difference map allowed for rapid, high-resolution scene comparison and change detection.

Chapter 3. *Using Structure from Motion to create DEMs and Orthoimagery from Historical Terrestrial and Oblique Aerial Imagery*, has received reviews from the journal Earth Surface Processes and Landforms February 20th, 2017, which are currently being implemented. In many regions around the world the lack of ongoing or consistent glacial observations and field measurements means there are distinct gaps in our spatio-temporal record of glacier change. In many glaciated regions,

however, there may exist photographic observations (e.g. aerial surveys, terrestrial surveys, tourist pictures) from which detailed spatial information can be extracted. This study addresses the question: **is it possible to extract high-resolution georeferenced DEMs from historical, archived glacier imagery with minimum a priori camera information?** The SfM technique was applied to archived historical imagery of glaciers in three geographic regions from three different periods. The imagery perspectives range from highly oblique aerial, mixed aerial and oblique terrestrial and range in camera format and image quality. GCPs were extracted from modern high-resolution imagery and terrain datasets. These models allow us to quantify the long term spatial changes occurring on these glaciers, using datasets that up until recently remained only visual sources of information.

Chapter 4. *A Conceptual Model of Supraglacial Lake Formation on Debris-covered Glaciers Based on GPR Facies Analysis*, published in the journal Earth Surface Processes and Landforms, October 19, 2016. The subaqueous environment of supraglacial lakes on heavily debris-covered glaciers remains a poorly understood area due not only to the difficulty in working in such environments, but also the high lake turbidity which limits visual investigation. The question being addressed in this study is: **can GPR surveys across frozen supraglacial lake surfaces, in combination with the technique of "facies analysis" and local observations, improve our ability to map lake bathymetry and the spatial distribution of lakebed debris?** Observations on the formation and evolution of supraglacial lakes on debris-covered glaciers have, for the most part, been aimed at areal expansion as

well as bathymetric mapping using point echo sounding and/or weighted lines. Yet, due to remote and logistically difficult locations there have been few attempts at repeat mapping of lakes in the Nepal Himalaya. To overcome the time-consuming point surveys, and to improve the speed, quantity and spatial information extracted from lake surveys, we employ ground penetrating radar on the frozen lake surface that allows us to not only extract bathymetric data, but also visualize the spatial distribution of specific radar signal facies. By interpreting these facies as different debris types we observe along the shores, we are able to describe the distribution of lakebed debris and develop an improved conceptual model of the processes and changes involved with supraglacial lake growth.

References

Bælum K, Benn D. 2011. Thermal structure and drainage system of a small valley glacier (Tellbreen, Svalbard), investigated by ground penetrating radar. The Cryosphere **5**: 139-149

Bass GF. 1966. Archaeology under water. Frederick A. Praeger: New York

Bass GF, Katsev ML. 1968. New tools for underwater archaeology. Archaeology **21**: 164-173

Dhanak MR, Xiros NI. 2016. Springer Handbook of Ocean Engineering. Springer

Duncan JMA, Biggs EM, Dash J, Atkinson PM. 2013. Spatio-temporal trends in precipitation and their implications for water resources management in climate-sensitive Nepal. Applied Geography **43**: 138-146. DOI: http://dx.doi.org/10.1016/j.apgeog.2013.06.011

Edney J. 2016. A Framework for Managing Diver Impacts on Historic Shipwrecks. Journal of Maritime Archaeology **11**: 271-297. DOI: 10.1007/s11457-016-9165-4

Fan Y, Weisberg PJ, Nowak RS. 2014. Spatio-temporal analysis of remotely-sensed forest mortality associated with road de-icing salts. Science of The Total Environment **472**: 929-938. DOI: http://dx.doi.org/10.1016/j.scitotenv.2013.11.103

Fitzpatrick AAW, Hubbard AL, Box JE, Quincey DJ, Van As D, Mikkelsen APB, Doyle SH, Dow CF, Hasholt B, Jones GA. 2014. A decade (2002–2012) of supraglacial lake volume estimates across Russell Glacier, West Greenland. The Cryosphere **8**: 107-121. DOI: 10.5194/tc-8-107-2014

Goodman D. 2009. GPR methods for archaeology. Seeing the unseen. Geophysics and landscape archaeology: 229-244

Green S, Bevan A, Shapland M. 2014. A Comparative Assessment of Structure from Motion Methods for Archaeological Research. Journal of Archaeological Science **46**: 173-181. DOI: 10.1016/j.jas.2014.02.030

Hölbling D, Betts H, Spiekermann R, Phillips C. 2016. Identifying Spatio-Temporal Landslide Hotspots on North Island, New Zealand, by Analyzing Historical and Recent Aerial Photography. Geosciences **6**: 48

Immerzeel W, Kraaijenbrink P, Shea J, Shrestha A, Pellicciotti F, Bierkens M, De Jong S. 2014. High-resolution monitoring of Himalayan glacier dynamics using unmanned aerial vehicles. Remote Sensing of Environment **150**: 93-103. DOI: 10.1016/j.rse.2014.04.025

Kadota T. 1994. Report for the field investigation on the Tsho Rolpa glacier lake, Rolwaling Valley, February 1993–June 1994. WECS Report N **551.489 KAD**:

Mackay SL, Marchant DR, Lamp JL, Head JW. 2014. Cold-based debris-covered glaciers: Evaluating their potential as climate archives through studies of ground-penetrating radar and surface morphology. Journal of Geophysical Research: Earth Surface **119**: 2505-2540

Mertes J, Thomsen T, Gulley J. 2014. Evaluation of Structure from Motion Software to Create 3D Models of Late Nineteenth Century Great Lakes Shipwrecks Using Archived Diver-Acquired Video Surveys. Journal of Maritime Archaeology **9**: 173-189. DOI: 10.1007/s11457-014-9132-x

Mertes JR, Thompson SS, Booth AD, Gulley JD, Benn DI. 2016. A conceptual model of supra-glacial lake formation on debris-covered glaciers based on GPR facies analysis. Earth Surface Processes and Landforms: n/a-n/a. DOI: 10.1002/esp.4068
Murray T, Gooch DL, Stuart GW. 1996. Structures within the surge front at Bakaninbreen, Svalbard, using ground-penetrating radar. Annals of Glaciology **24**: 122-129
Neubauer W, Eder-Hinterleitner A, Seren S, Melichar P. 2002. Georadar in the Roman civil town Carnuntum, Austria: an approach for archaeological interpretation of GPR data. Archaeological Prospection **9**: 135-156
Oxley I, Gregory D. 2002. Site management. In *International Handbook of Underwater Archaeology*. Springer; 715-725
Ozainne S, Lespez L, Garnier A, Ballouche A, Neumann K, Pays O, Huysecom E. 2014. A question of timing: spatio-temporal structure and mechanisms of early agriculture expansion in West Africa. Journal of Archaeological Science **50**: 359-368. DOI: http://dx.doi.org/10.1016/j.jas.2014.07.025
Pälli A, Kohler JC, Isaksson E, Moore JC, Pinglot JF, Pohjola VA, Samuelsson H. 2002. Spatial and temporal variability of snow accumulation using ground-penetrating radar and ice cores on a Svalbard glacier. Journal of Glaciology **48**: 417-424
Peacock AJ. 1998. Oxygen at high altitude. BMJ : British Medical Journal **317**: 1063-1066
Rabatel A, Dedieu JP, Vincent C. 2016. Spatio-temporal changes in glacier-wide mass balance quantified by optical remote sensing on 30 glaciers in the French Alps for the period 1983–2014. Journal of Glaciology **62**: 1153-1166
Ricevuto E, Kroeker KJ, Ferrigno F, Micheli F, Gambi MC. 2014. Spatio-temporal variability of polychaete colonization at volcanic CO2 vents indicates high tolerance to ocean acidification. Marine Biology **161**: 2909-2919. DOI: 10.1007/s00227-014-2555-y
Ryan JC, Hubbard AL, Box JE, Todd J, Christoffersen P, Carr JR, Holt TO, Snooke NA. 2015. UAV photogrammetry and structure from motion to assess calving dynamics at Store Glacier, a large outlet draining the Greenland ice sheet. The Cryosphere **9**: 1-11. DOI: 10.5194/tc-9-1-2015
Sambuelli L, Bava S. 2012. Case study: A GPR survey on a morainic lake in northern Italy for bathymetry, water volume and sediment characterization. Journal of Applied Geophysics **81**: 48-56
Singh K, Kulkarni A, Mishra V. 2010. Estimation of glacier depth and moraine cover study using ground penetrating radar (GPR) in the Himalayan region. Journal of the Indian Society of Remote Sensing **38**: 1-9
Sneed WA, Hamilton GS. 2007. Evolution of melt pond volume on the surface of the Greenland Ice Sheet. Geophysical Research Letters **34**: L03501. DOI: 10.1029/2006GL028697
Thompson SS, Benn DI, Dennis K, Luckman A. 2012. A rapidly growing moraine-dammed glacial lake on Ngozumpa Glacier, Nepal. Geomorphology **145**: 1-11. DOI: 10.1016/j.geomorph.2011.08.015
Van Liew H, Flynn E. 2005. Decompression tables and dive-outcome data: graphical analysis. Undersea & hyperbaric medicine **32**: 187

Verhoeven G, Doneus M, Briese C, Vermeulen F. 2012. Mapping by matching: a computer vision-based approach to fast and accurate georeferencing of archaeological aerial photographs. Journal of Archaeological Science **39**: 2060-2070. DOI: http://dx.doi.org/10.1016/j.jas.2012.02.022

Watanabe T, Matsuoka N, Christiansen HH. 2013. Ice-and Soil-Wedge Dynamics in the Kapp Linné Area, Svalbard, Investigated by Two-and Three-Dimensional GPR and Ground Thermal and Acceleration Regimes. Permafrost and Periglacial Processes **24**: 39-55

Zhao W, Forte E, Pipan M, Tian G. 2013. Ground penetrating radar (GPR) attribute analysis for archaeological prospection. Journal of Applied Geophysics **97**: 107-117

Chapter 1. Evaluation of Structure from Motion Software to Create 3D Models of Late Nineteenth Century Great Lakes Shipwrecks Using Archival Diver-Acquired Video Surveys[1]

Abstract

Here we demonstrate the ability to use archived video surveys to create photorealistic 3-D models of submerged archeological sites. We created 3-D models of two 19th century Great Lakes shipwrecks using diver-acquired video surveys and Structure from Motion (SfM) software. Models were georeferenced using archived hand survey data. Comparison of hand survey measurements and digital measurements made using the models demonstrate that spatial analysis produces results with reasonable accuracy when wreck maps are available. Error associated with digital measurements displayed an inverse relationship to object size. Measurement error ranged from a maximum of 18% (on 0.37 m object) and a minimum of 0.56% (on a 4.21 m object). Our results demonstrate SfM can generate models of large maritime archaeological sites that can be used for research, education and outreach purposes. Where site maps are available, these 3-D models can be georeferenced to allow additional spatial analysis long after on-site data collection.

[1] The material in this chapter was previously published in the Journal of Maritime Archaeology, 15th October 2014.

Introduction

Traditionally, archeologists have surveyed sites using tools such as simple tape measures, compasses, levels and theodolites; through recent technological advancement, their tools have evolved to include laser range finders, GPS, aerial photography and laser scanning (Howard, 2006). Many of the tools used for terrestrial archaeology are not only time and labor intensive (Henderson et al., 2013) but are often difficult to perform accurately in an underwater environment, for example, detailed trilateration of deep sites (Bass, 1966, Green, 1973). Unlike their terrestrial counterparts, marine archeologists are subject to strict time constraints when conducting site characterizations and surveys. Depth, water temperature and breathing gas supply constrain diver bottom time. In addition, financial constraints typically limit ship availability to support prolonged site surveys. Both time constraints on divers and the cost of ship time can greatly reduce the time available for underwater site characterization relative to terrestrial locations. As a result, cost of survey equipment and efficiency are paramount to the maritime archaeologist (Skarlatos et al., 2012).

In recent decades, maritime archeologists have experimented with alternative site characterization techniques to increase data acquisition efficiency and minimize dive time requirements. New techniques primarily include stereo and multi-image photogrammetry (originally used in terrestrial topographic mapping), sonar mapping and the use of remotely operated vehicles (ROVs) (Henderson et al., 2013). These techniques provide complementary data for site characterization, but each is subject to limitations related to data resolution or equipment cost.

Photogrammetry allows the extraction of 3-D information from overlapping images of objects or field sites. By analyzing the parallax between image pairs one can extract the relative topography within the scene. For 3-D information to be extracted, images must contain sufficient overlap, generally 60% along the survey track and 20% between survey tracks (Ludvigsen et al., 2006, Drap et al., 2007, Drap, 2012), and each image must be taken from locations that are surveyed into a defined reference measurement system. Camera orientation information such as roll, pitch, yaw, and position information; X, Y, Z, must also be known so that positions of discrete points within different images can be co-registered. This allows for extraction of 3D information and creation of photorealistic, georeferenced 3D site models (Pollio, 1968).

Stereo photogrammetric mapping of underwater sites was originally tested in 1963 at Yassi Ada (Bass, 1966). Later refinement led to more widespread adoption of the technique for archeological research (Pollio, 1968, Rosencrantz, 1975). While this technique decreased the overall time divers spent underwater, post-processing required labor-intensive manual matching of individual points between imagery. This manual matching method limited widespread adoption of the technique until the later part of the 20th century when digital cameras and photogrammetry software packages automated much of the post processing (McCarthy and Benjamin, 2014).

Side scan sonar has been another important development allowing for rapid underwater site surveys and greatly improving the ability to locate sunken artifacts (Bass and Katsev, 1968). Because of these attributes, it is one of the most powerful tools in underwater

archaeology (Klein, 2002). While side scan sonar generates 3-D survey products, spatial resolution is coarse, and artifacts and noise must be carefully removed to yield a final product (Singh et al., 2000). Recent attempts have been made to combine 3-D acoustic and photogrammetric data to produce high resolution 3-D models of underwater sites, causing minimal site disturbance (Drap et al., 2014). This method, however, employs 3-D sonar scanners at a cost of over 50,000USD, exceeding the budget of many archaeologists.

Maritime archaeologists are using remotely operated vehicles (ROVs) with increasing frequency. Scientific literature and popular media have both documented the effectiveness of ROVs to aid in the discovery of and photographic surveying of underwater sites, particularly those that exceed the depths accessible using SCUBA. Two of the most notable ROV studies are the *Argo* investigation of the steamship *Titanic* and the battleship *Bismark* (Ballard and Michel, 1985, Ballard, 1989). Photographs from these ROV-based expeditions have produced some of the best resolution 2-D mosaics of entire shipwrecks. The newer, smaller ROV *Jason* has even surveyed interior portions of the *Titanic*. While ROVs are useful tools for photographic and video surveys, the data collected can only provide 2-D information about the site.

Photogrammetry, sidescan sonar and ROV data collection techniques provide highly-detailed information, but the high cost of equipment can often exceed the budget constraints of smaller research groups. Recent advances in computer performance and software allow photographic surveys conducted using consumer-grade photographic

equipment to be transformed into georeferenced, photorealistic 3D models. The new method, known as Structure from Motion (SfM) or multi-image photogrammetry, is based on many of the same underlying principles as photogrammetry, and can be used for creating 3-D models from 2-D images. Unlike photogrammetric surveys, however, SfM surveys do not require collection of camera location and orientation information during image acquisition. Instead, camera positions and attitude are determined through feature matching across all image combinations, which are then used to create a 3-D point cloud of photographed objects (Agisoft, 2014). SfM uses multiple overlapping images, taken from many different angles, to construct 3-D models. Models initially have an arbitrary coordinate system, but if the images used include identifiable surveyed ground control points, it is possible to transform the model into the known coordinate system. Because the technique only requires consumer-grade camera equipment, a computer and SfM software, the financial costs of SfM are well within the budget of smaller research teams (McCarthy and Benjamin, 2014).

SfM has been increasingly used to document terrestrial sites, such as: Schwarzenbach, Austria (Doneus et al., 2011), Casa Valentini, Italy (Verhoeven, 2011), Tel Akko, Isreal (Olson et al., 2013), Boudelo, East Flanders (De Reu et al., 2013), St. Andrew's Church, Jevington (Green et al., 2014) and Rubha an Fhaing Dhuibh, Scotland (McCarthy and Benjamin, 2014). Documenting an entire site using terrestrial or small UAV systems has proven to be very fast and inexpensive method to create highly accurate models used for measurements, public outreach and as educational tools. Conversely, SfM has rarely been used in maritime studies and early experiments required the use of cumbersome

equipment. For example, Ludvigsen et al. (2006) developed a system for photographic mapping of a 19th century shipwreck off the western coast of Norway that required the use of a ROV, camera and lighting system mounted on 10 m x 10 m metal frame , which moved on a rack and rail system. The frame was suspended approximately 1-2 m above the stern of the ship and allowed the acquisition of two sets of photographs, approximately 250-270 in number. The photographs were processed using SLAM and SfM to create high-resolution surface models and mosaicked scenes.

In contrast, McCarthy and Benjamin (2014) demonstrated the ability of the SfM method to produce detailed models of a small cluster of cannons and an anchor using off-the-shelf, consumer-grade, handheld underwater cameras . The accuracy of their digital measurements when compared to manual measurements ranged from 0-56%, with the largest percentage error occurring on the smaller measurements. Measurement error when conducting *in situ* measurements is believed to be the cause of this skew, as the precise location of the measurements varies slightly. Due to small measurement differences between the field and the digital model, smaller measurements end up with a larger percentage error.

Studies such as Ludvigsen et al. (2006), McCarthy and Benjamin (2014) and Henderson et al (2013) have demonstrated the ability of SfM to characterize archaeological sites of varying sizes using automated mechanical image acquisition and diver based image acquisition, when SfM modeling is the primary goal of the study. Many underwater archeological sites have been subjected to photographic and video surveys, with the goal

of creating 2-D photomosiacs, but the possibility of using SfM to extract 3-D information from archived imagery has not yet been assessed. In addition, few studies have used SfM to create 3-D models of large-scale underwater archeological sites, such as shipwrecks, using video surveys.

Numerous studies illustrate successful 3-D model generation from video sequences with SfM software in a terrestrial setting (Nicosevici and Garcia, 2008, Sedlazeck et al., 2009, Beall et al., 2010) however use as a highly efficient replacement for underwater archeological surveys has not been fully explored. In this paper we aim to demonstrate that archived video surveys of shipwrecks can be can be used as input for SfM analysis and yield highly accurate and detailed 3-D models of shipwrecks. We present two highly detailed 3-D models of 19th century shipwrecks in Lake Michigan (Figure 1.1 A, B, C), derived from diver collected video. We use video stills as inputs to SfM software for model creation and offer an initial assessment of the ability of the technique to be used as a measurement tool by comparing digital measurements with measurements made as part of the initial site hand surveys.

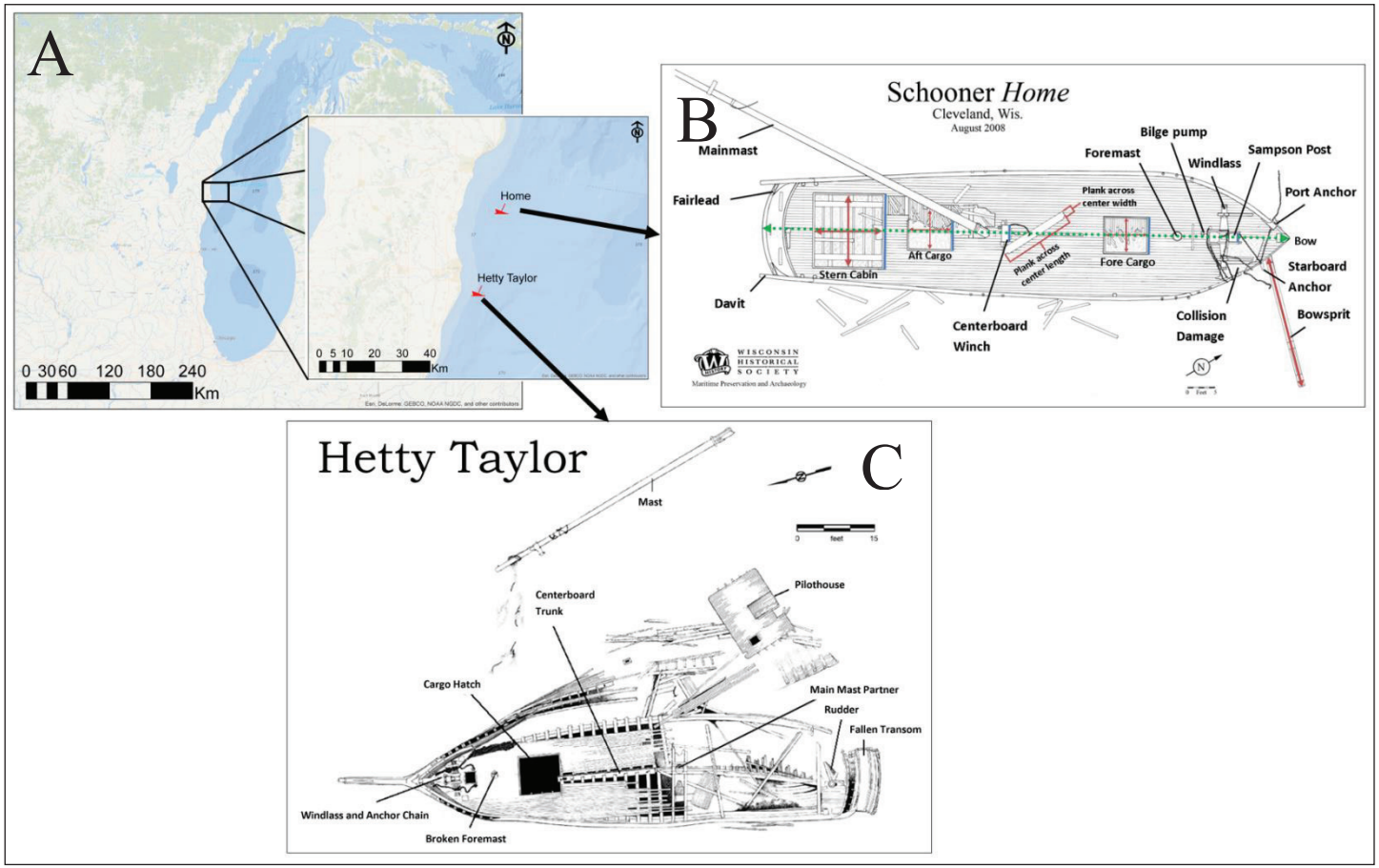

Figure 1.1: Overview of shipwreck locations (A) along with detailed wreck maps produced from manual underwater measurements (B, C) (Data source: Wisconsin Historical Society). The colored lines on the wreck map of the schooner Home indicate measurements reproduced in this study.

Study Sites

The Schooner Hetty Taylor

The remains of the 2-masted schooner *Hetty Taylor* rests 8 km east of Sheboygan, Wisconsin, in 32 m of water. Built in Milwaukee, Wisconsin, in 1874, the *Hetty Taylor* was lost 26 August 1880 in a sudden squall while in route from Milwaukee to Escanaba, Michigan. The wreck lies in a trough of sand, which has intruded into many areas of the vessel. Overall, the shipwreck exhibits excellent preservation, with the bow, most of the fore deck, and the entire port side intact. The starboard side is splayed open and constitutes part of a larger debris field that includes the top of the deckhouse, afterdeck, and a variety of timbers. A single mast, dislodged by contemporary salvage efforts, lays adjacent to the debris field.

The *Hetty Taylor* is a rare example of once common class of Great Lakes commercial craft, the small coasting schooner that provided economic and cultural links between the isolated communities of Northern Lake Michigan's maritime hinterland and thriving metropolises of southern Lake Michigan. Although common in Wisconsin history, intact small schooners from her period are an archeological rarity. The *Hetty Taylor* was listed on the National Register of Historic Places on 1 June 2005 (Meverden and Jensen, 2004).

The Schooner *Home*

The 2-masted schooner *Home* lies upright and intact in 52.7 m in Lake Michigan, 17.7 km southeast of Manitowoc, Wisconsin. Shipwright William B. Redfield constructed the schooner in Sandusky, Ohio, in 1843. She measured 29.8 m, with 7.2 m beam. The *Home* served as a lakeshoring vessel on Lake Erie primarily carrying grain and merchandise

between Sandusky, Ohio, and Buffalo, New York, for owner Captain Morris Tyler. She spent her last five years of operation on Lake Michigan working in the lumber trade. While in route to Chicago, Illinois, from Manitowoc, Wisconsin, the *Home* was lost in an early morning collision with the schooner *William Fiske* on 19 October 1858.

Today the *Home* rests with a one-degree port list and a 4-degree bow-down attitude. Although, the foremast was broken at deck level and salvaged in commercial fishing nets, the mainmast remains on the wreck. It has been unstepped from the keelson and toppled towards the port quarter and now lies at an angle across the port rail. Several of the deck planks and mast partners were sprung around the mast hole when it toppled. Evident on her deck is a windlass, Sampson post, forward scuttle, single acting bilge pump, centerboard winch, forward and aft cargo hatches, and a rudder post with tiller. *Home's* hull is mostly intact with the exception of collision damage at the starboard bow, which carried away her port cathead and then lifted the stern cabin.

The *Home* is representative of a rare and relatively undocumented vessel type and trade, the Great Lakes lakeshoring schooner. Few archaeological examples of lakeshoring schooners exist today, and the archaeological integrity of the *Home* wreck site makes this wreck particularly significant. The *Home* was listed on the National Register of Historic Places on 28 December 2010 (Meverden and Thomsen, 2010).

Methods

Shipwreck Survey

Divers conducted numerous hand measurements on both the *Hetty Taylor* and the *Home* wrecks during surveys. The *Hetty* Taylor was surveyed throughout the summers of 1996,

97 & 98. The video survey was captured on 8 July 2008. The *Home* was surveyed between 27 July and 2 August 2008 and the video was captured on 10 July 2009. Divers estimate the visibility around both sites was ~28 m. For the surveys, divers affixed a cable baseline with attached fiberglass measuring tape to each wreck and extended it along the vessel's centerline from bow to stern. Cross lines were established at 3.05 m intervals on either side of the baseline, extending beyond the farthest extent of the wreckage at right angles to the baseline. The scaled baseline gave surveyors a reference to coordinate all measured sketches and photographs. The cross lines, in addition to acting as an additional reference, partitioned the wreck site into 3.05 m sections for mapping. Each survey team member sketched one 3.05 m section where wreck features were trilaterated to the baseline using additional fiberglass measuring tapes, plum-bobs, pencils and Mylar graph paper. All measurements were recorded to a precision of 0.03 m to minimize recording errors (Figures 1.1 B, C) These measurements are assumed to have an accuracy of 0.03 m. Wreck surveys were used for georeferencing of the 3D models as well as to compare measurements made using the model against field measurements.

Video surveys of the wrecks were conducted to collect mosaic imagery. Divers used the "Minibee" camera, which is owned by Woods Hole Oceanographic Institution-Advanced Imaging and Visualization Laboratory to collect all video. The camera is a custom-packaged, 1 inch, single chip Kodak CCD sensor with debayering, and all images were acquired with a 6.5mm lens. Minibee was mounted in a down facing orientation on the front of a Silent Submersion UV26 diver propulsion vehicle (Figure 1.2) along with battery packs, and piloted roughly 6.10 m above the shipwrecks. An array of six Sartek

50 Watt HIDs, with reflectors, were affixed to depth compensating arms and mounted to the UV26. Divers adjusted the arms at depth for appropriate light fill as seen through the viewfinder. Depth control of the UV26 was accomplished using a Liquivision brand dive computer with depth gauge. A bubble level was mounted to the top of the Minibee to assure down looking position. Recording was conducted on the surface through a fiber optic cable link that allowed the surface team to adjust camera setting such as aperture, white balance or exposure. Overlapping passes of the wreck site and adjacent debris fields were made to collect a full data set. Surveys took approximately 25 minutes with 10 passes. Fisheye correction was performed in Adobe Photoshop 7 by using the distortion tool. A spherical distortion was applied until features that are known to be straight became straight. This was then recorded as a macro and applied to all other images. The video was then transformed into a collection of still images with a resolution of 72 dpi and dimensions of 1920 x 1080 pixels. Each 100^{th} frame was originally hand-selected for further analysis, though we now use a custom-made MATLAB function. Our function takes in the video file and outputs the series of images, allowing the user to select how many frames and the output image settings.

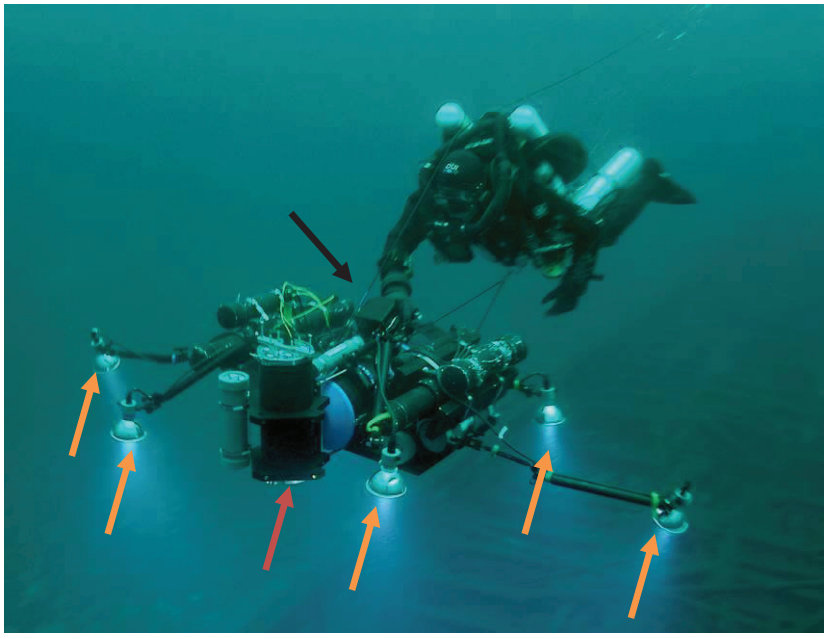

Figure 1.2: Silent Submersion UV26 diver propulsion vehicle being operated above shipwreck. The six Sartek lights (orange arrows) are arranged around the vehicle with the Minibee in a downward facing direction, located at the nosecone (red arrow). The diver views the video through the viewfinder screen (black arrow).

All images were preprocessed using contrast-limited adaptive histogram equalization (CLAHE) (Singh et al., 2011). The CLAHE method was implemented in MATLAB R2014a (8.3.0.532) using the function *adapthisteq* and following suggestions for processing color images, found in the function documentation. All function parameters are set to *default* other than 'NumTiles' and 'ClipLimit' which are 5 and 0.005 respectively. We created new image files using the function *imwrite*, exporting a TIFF image with default settings. This step greatly increased the quality of the images and reduced vignettes caused by poor lighting (Figure 1.3). While other methods of preprocessing underwater imagery have been proposed (Bazeille et al., 2006, Iqbal et al.,

2007) due to time restrictions as well as a successful first assessment additional preprocessing was not needed.

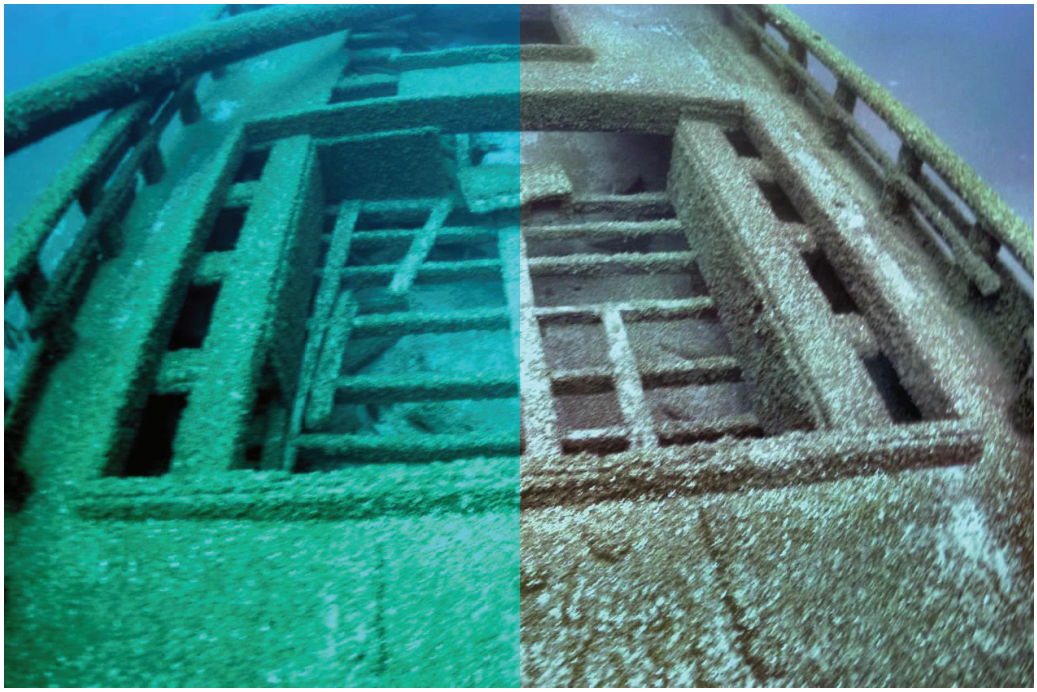

Figure 1.3: Original imagery from underwater submersible vehical (left) along side CLAHE adjusted image (right). Note the distinct over saturation of green in the original is substantially reduced in the CLAHE version.

AgiSoft Photoscan Model Generation

Agisoft Photoscan SfM software package version 1.0.4 build 1847 (64 bit) was used to create the 3D models. The series of images for each model (228-Hetty, 221-Home) was imported into Photoscan and aligned using the “high” quality setting, which analyzes the images at full resolution, other options are “medium” (1/4 resolution) or “low” (1/8 resolution). The alignment used the default settings recommended by AgiSoft for DEM generation. Initial alignment detects pixels between image pairs (i.e. where pixel

similarities exist), using these image pairs, and by further matching more pixels, the software is able to determine scene structure as well as an estimate of camera position for each image. The resulting sparse point cloud allows the user to visualize the initial alignment and assess the scene. If camera focal plane information is collected during image acquisition, it can be used to improve the accuracy of the alignment; however, this information is not necessary for model construction and was not available for use in our study. The sparse cloud for the *Hetty Taylor* contains 473314 matched pixels (Figure 1.4 A) and the *Home* contains 81384 matched pixels.

Following the initial camera alignment and scene estimation, we removed points that appeared erroneous before generating the dense point cloud. We chose to create a "high" quality dense point cloud, which includes ¾ of the pixels in generation. The other choices (i.e. ultra-high, medium, low and ultra-low) operate on resolutions that increase or decrease by ¼ respectively. The dense point cloud generation searches for more matching pixels and produces the bulk of the point data for the final model. The dense cloud for the *Home* contains 24492773 matched pixels (Figure 1.4 B) and the *Hetty Taylor* contains 14636426 matched pixels.

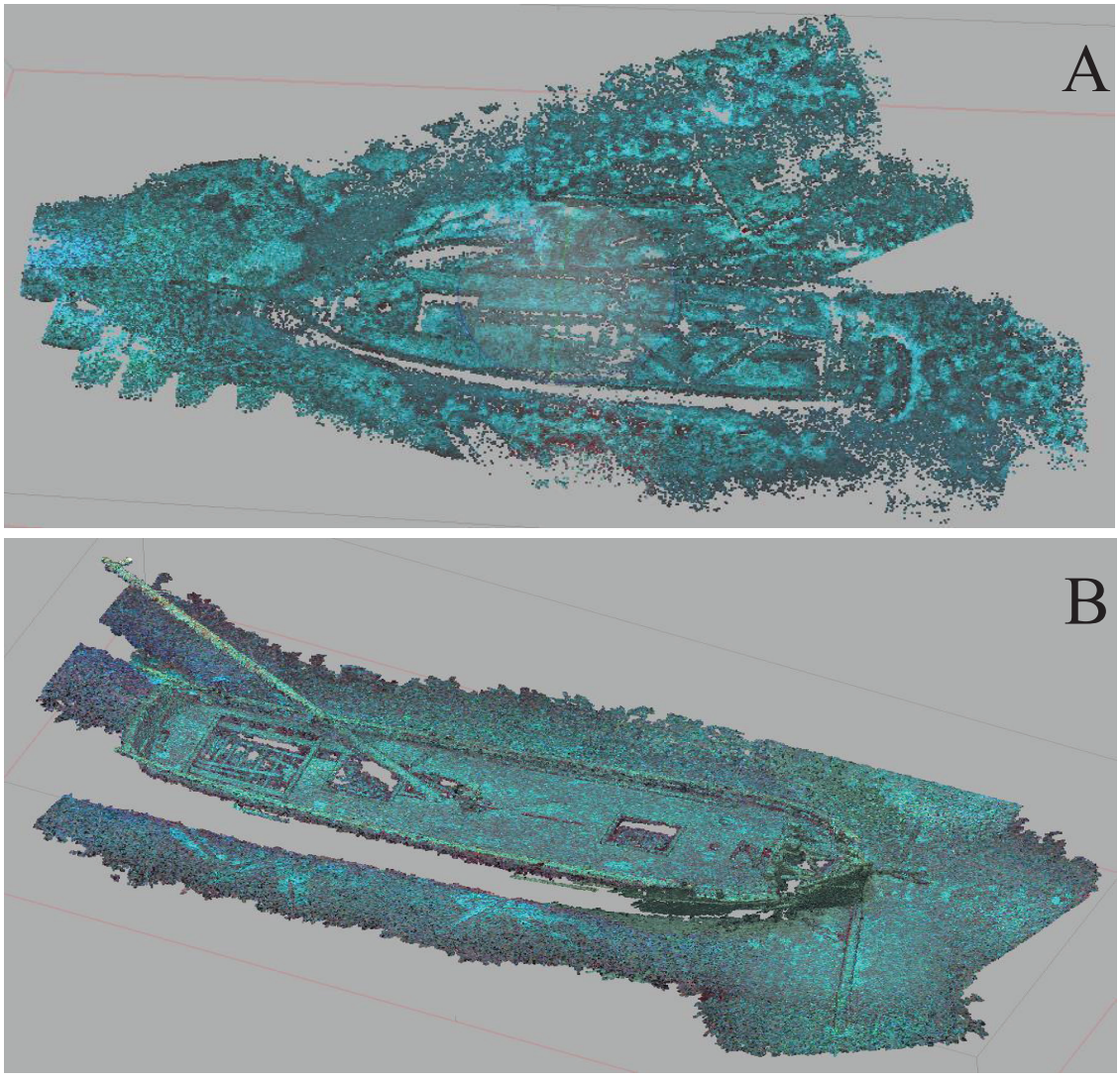

Figure 1.4: Sparse point cloud of the schooner Hetty Taylor (A) and dense point cloud of the schooner Home (B).

Using this dense point cloud, a triangulated 3D mesh is produced, that lacks a defined coordinate system. The software suggests a value for the number of triangulated faces. It is possible to manually set a limit, but we chose the suggested value for a “High” polygon count, which corresponds to 1/5 of the total number of dense points. In addition, there are options to fill voids through interpolation or extrapolate edges. For our models, we did

not use void filling. 2818826 nodes and 5636550 faces were created for the *Home* and 1466133 nodes and 2925437 faces were created for the *Hetty Taylor*. Shading of the model using the photos provides a first look at the 3D model, allowing rotation in space and minor adjustments (Figure 1.5 A&B).

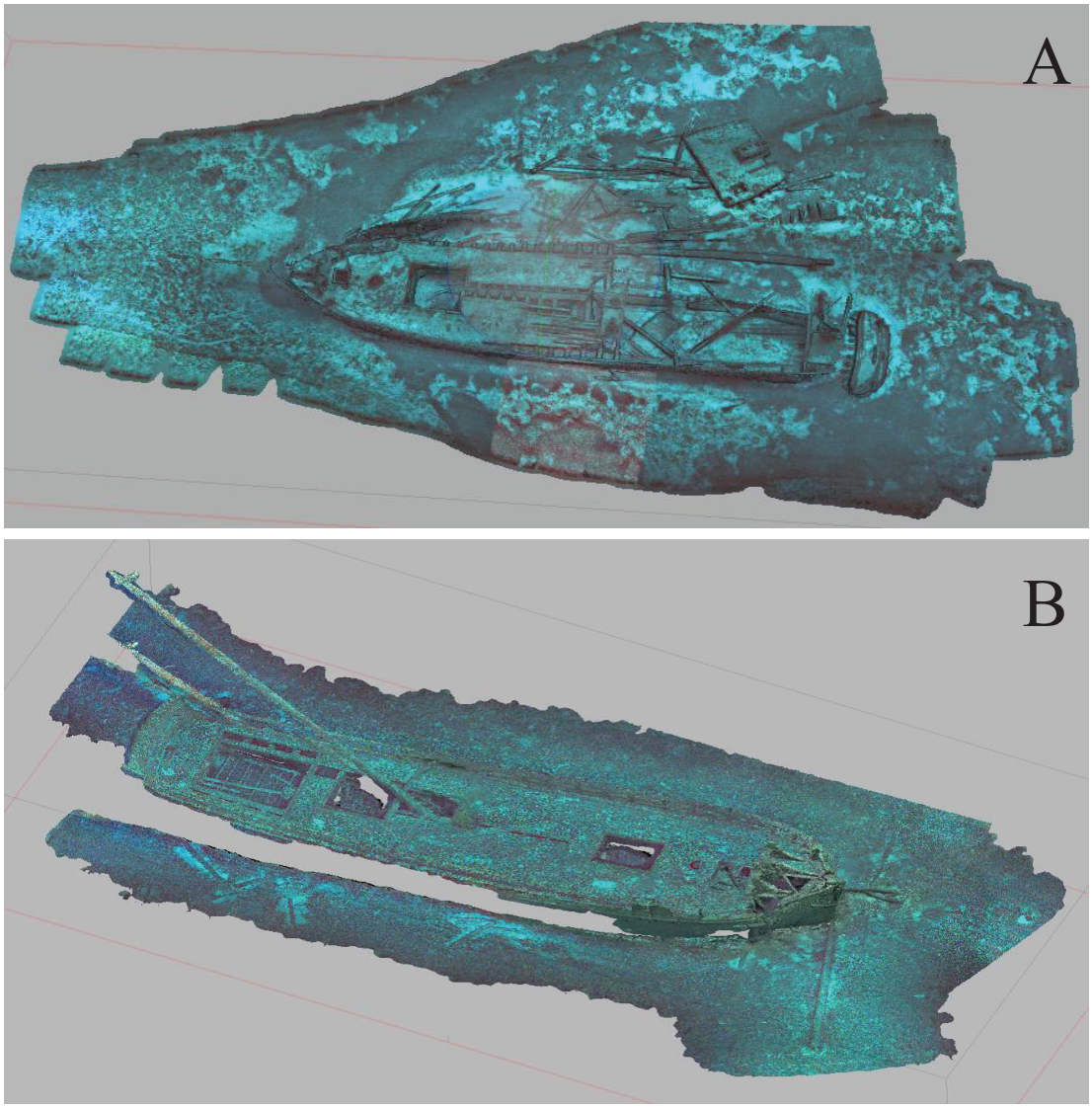

Figure 1.5: 3D shaded model of the schooner Hetty Taylor (A) and the schooner Home (B).

Finally, mosaicked orthophotos are made using the final models and the input imagery. Figure 1.6 shows the resulting orthophotos (A & B) and in addition, an orthophoto generated using Adobe Photoshop 7. All Photoscan steps were performed on a Lenovo W510 with Intel i7 Q720 dual quad core1.60Ghz processors and 32 GB of internal memory and a NVIDIA Quadro FX 880M GPU. Processing time from start to finish took on average two days total.

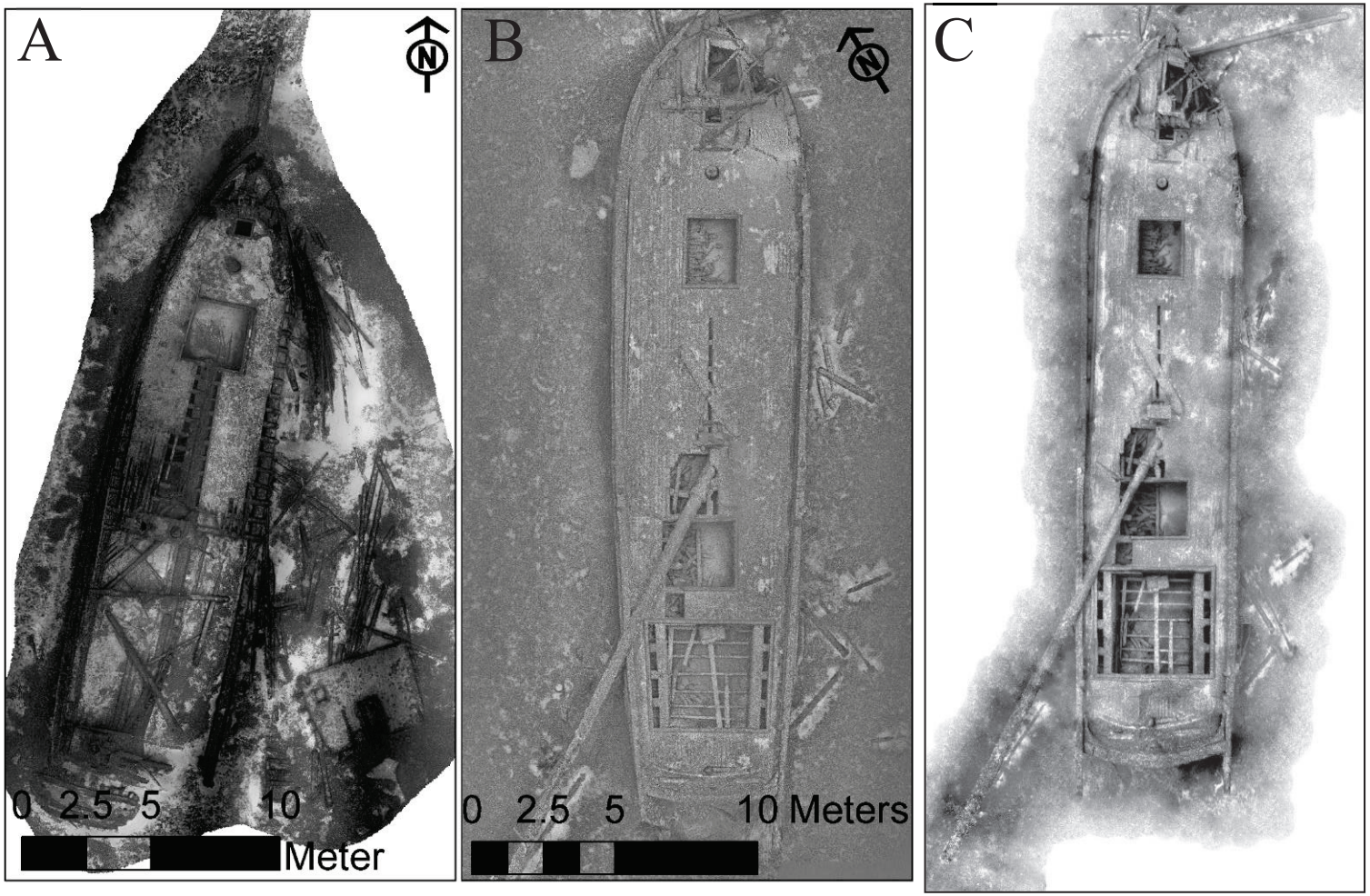

Figure 1.6: Orthophoto generated from Photoscan for the *Hetty Taylor* (A) and *Home* (B) wreck sites. Photo mosaic created manually from photostills of the Home wreck site (C). Note tapering of side rails of Home which match with wreck map measurements yet are not preset in the manually produced mosaic.

Model Alignment

AgiSoft recommends that approximately 10 ground control points (GCPs) should be used when georeferencing a digital elevation model (Agisoft, 2014). The addition of GCPs to the model helps resolve issues such as skew, rotation and scale errors that occur during pixel matching. In terrestrial surveys, GCPs are typically established using differential GPS surveys and are primarily used to fit the resulting model to a real-world coordinate system. In maritime surveys, GCPs can be established by defining a local benchmark and using triangulation between points (Diamanti et al., 2011). In this investigation, we were working with archived video and photographic imagery, therefore we were not able to incorporate GCPs. As an alternative, we used maps created from hand surveys of each site to align our 3D models (Figure 1.1 A&B) using Autodesk 3DS Max.

Once the 3D model was created in Photoscan, we exported the model and the orthophoto texture map to a 3DS Max file. In 3DS Max we created a plane object centered at the origin extending in the X,Y directions in the same size as our wreck map images. The wreck maps were then draped over the plane. Next, we imported the 3D model and merged it with the current project. We then began to move the model around the wreck map plane and adjusted it to fit. To do this we used the shift, scale and rotate tools in 3DS Max while the model was set to be somewhat transparent. Once the models have been aligned, we then assigned them a texture using the output orthoimagery from Photoscan.

Model Measurements

We repeated a series of measurements from the official reports of each shipwreck (Meverden and Jensen, 2004, Meverden and Thomsen, 2010) using the measure tool in

Adobe Photoshop (Figure 1.1 B). By calculating the actual scaled size of a single pixel, in Photoshop you can set the measurement scale and easily create a data table of all measurements performed. We calculated 0.016 m per pixel for the *Home* and 0.011 m per pixel for the *Hetty Taylor*.

The measurements we made on the *Home* wreck were designed to cover a range of sizes and locations of objects on the vessel (Figures 1.1, B; Table 1.1). All measurements to "leading edges" are distances from the tip of the bow along the centerline to the forward edge of the object. On the *Home* the length and width of the fore and aft cargo holds were measured in addition to the opening left by the removal of the stern cabin. Measurements made from the bow included the leading edges of the two holds, the stern cabin, as well as to the winch and sampson's post. Lastly, we measured a prominent wooden plank that was lying across the deck and the bowsprit lying in the sand off the leading starboard side.

Table 1.1: Reported measurements from field survey of the Schooner *Home* with digital measurements and % error.

Measurement	Reported (m)	Measured (m)	% Error	Difference (m)
Aft Cargo Leading Edge	18.96	18.71	1.31	0.25
Aft Cargo Length	2.44	2.39	1.98	0.05
Aft Cargo Width	1.89	2.11	11.65	-0.22
Bowsprit Length	8.11	7.97	1.70	0.14
Forward Cargo Leading Edge	7.99	7.66	4.08	0.33
Forward Cargo Length	2.44	2.41	1.16	0.03

Forward Cargo Width	1.92	1.83	4.70	0.09
Plank On Center Length	3.93	3.87	1.57	0.06
Plank On Center Width	0.37	0.43	17.56	-0.06
Samson Post Leading Edge	2.93	2.95	0.82	-0.02
Ship Length	29.87	29.34	1.78	0.53
Stern Cabin Leading Edge	22.92	22.44	2.10	0.48
Stern Cabin Length	3.96	3.87	2.33	0.09
Stern Cabin Width	4.21	4.23	0.56	-0.02

Fewer hand measurements were available for the *Hetty Taylor* and its structure is much more damaged than the *Home*. Consequently, our choice of repeatable measurements is fewer than the *Home*. We measured the bowsprit length to the point where it meets the bow stem. We were able to measure the length and width of the centerboard, deckhouse hatch, fore cargo hold and the small deckhouse. In addition, we measured the diameter of the remaining foremast (Table 1.2).

Table 1.2: Reported measurements from field survey of the Schooner *Hetty Taylor* with digital measurements and % error.

Measurement	**Reported (m)**	**Measured (m)**	**% Error**	**Difference (m)**
Centerboard Trunk Width	0.36	0.35	1.60	0.01
Deckhouse Hatchway Width	0.41	0.46	11.65	-0.05
Fore Mast Hole	0.53	0.49	8.86	0.04

Deckhouse Hatchway Length	0.56	0.47	18.89	0.09
Small Deckhouse Width	0.76	0.75	1.60	0.01
Small Deckhouse Length	1.55	1.52	2.27	0.03
Fore Cargo Length	2.44	2.48	1.68	-0.04
Fore Cargo Width	2.67	2.50	6.68	0.17
Deckhouse Length	3.05	3.41	10.62	-0.36
Bowsprit Length	3.66	3.85	5.00	-0.19
Deckhouse Width	5.18	4.73	9.55	0.45
Centerboard Trunk Length	6.13	5.61	9.21	0.52

Results

Measurement Accuracy

The maximum measurement for the *Home* is the overall ship length, measured in the field as 29.87 m and in the 3D model as 29.34 m. The smallest object measured, the width of the plank lying across the center, was 0.37 m in the field and 0.43 m using the 3D model. The three main square openings on the deck, the fore cargo hold, aft cargo hold and the stern cabin, being clearly visible, were measured lengthwise and width wise across the center point of each. Of these, the width of the aft cargo hold shows the largest error at 11.65%. The overall percentage errors associated with the measurements are < 5%, with the exception of the plank across the center (Figure 1.7). The minimum error is encountered in the comparison of the stern cabin width at 0.56%. The maximum and minimum percentage errors in our measurements for the *Home* are 0.56-17.56%

respectively. Aside from measurements, the model generated from SfM also displays better overall shape accuracy when compared with the mosaic created by aligning photos in Photoshop 7 (Figure 1.6 B & C).

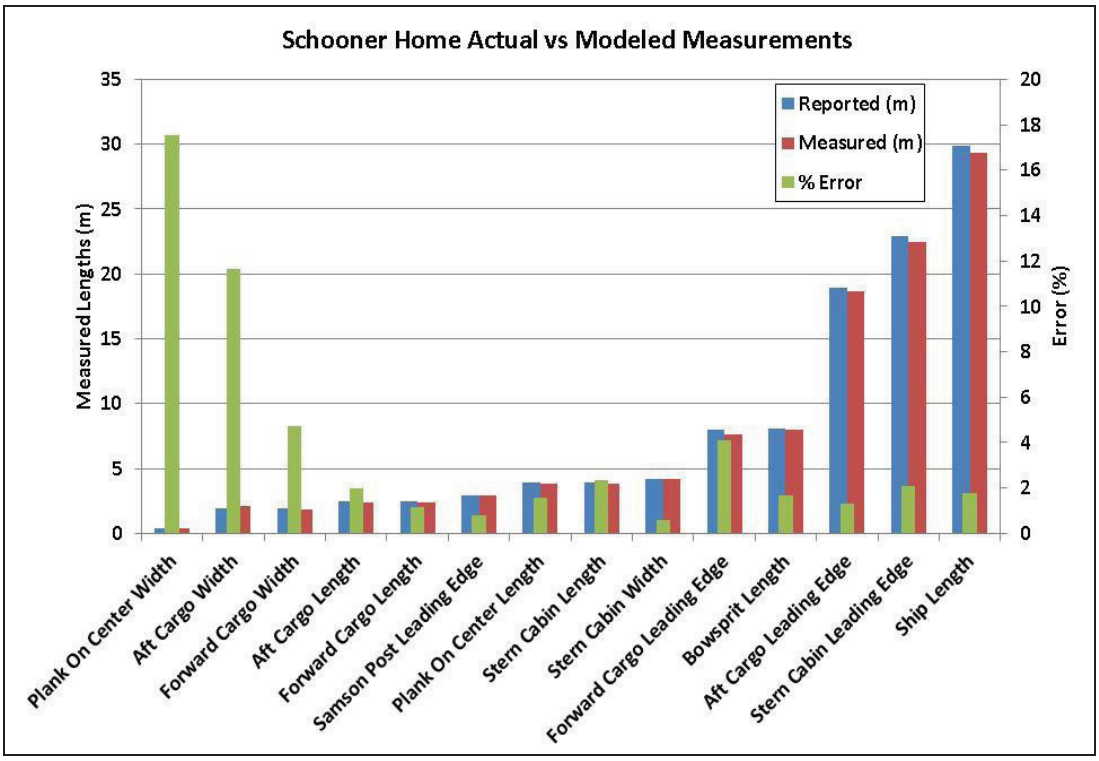

Figure 1.7: Comparison of field measurements and % error, made on the schooner *Home* with 3D model measurements.

The largest measurement on The *Hetty Taylor* is the centerboard trunk length which is visible protruding through the deck. It measured 6.12 m in the field and 5.61 m using the 3-D model. The smallest measurement is the centerboard trunk width at 0.35 m in the field and 0.35 m using the model. The measurement with the largest error, 18 %, is the deckhouse hatchway length. In the field, this was measured at 0.56 m and our measurement of the model is 0.47 m. Our accuracy results from the *Hetty Taylor* are

therefore similar to those of the *Home,* in that there are some smaller measurements with the largest % error (Figure 1.8).

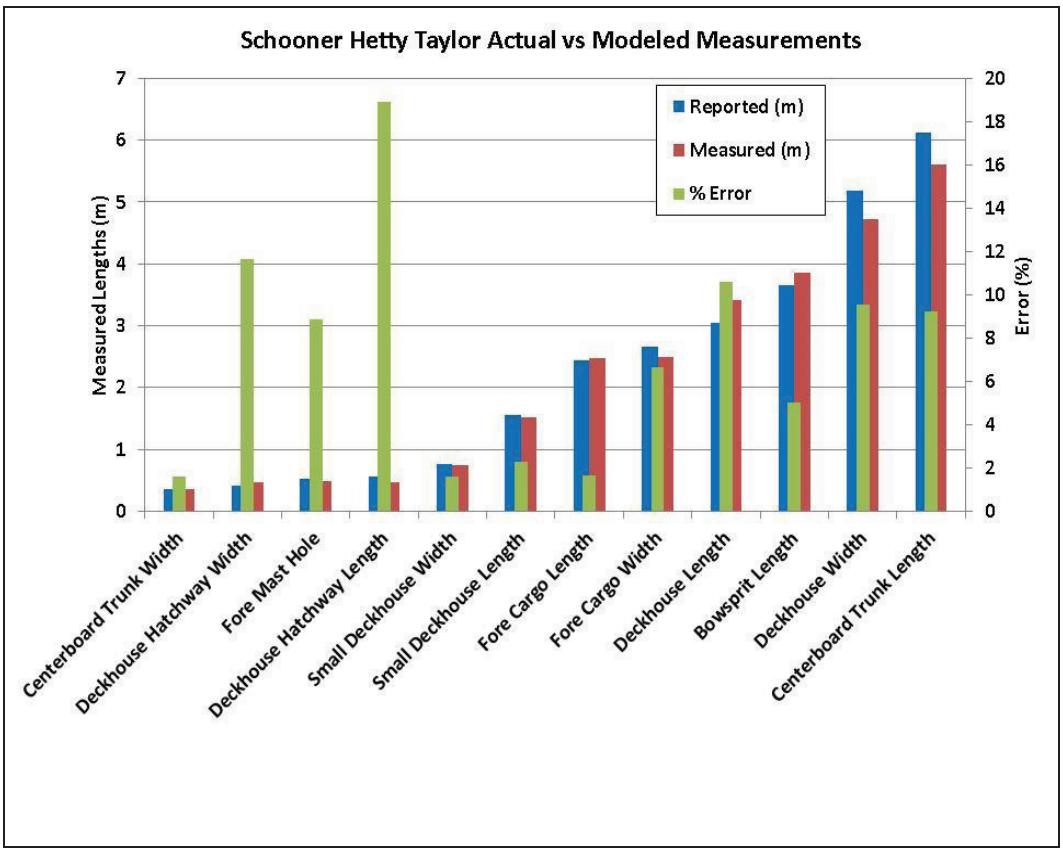

Figure 1.8: Comparison of field measurements and % error, made on the schooner *Hetty Taylor* with 3D model measurements.

Both the models of the *Hetty Taylor* and the *Home* contain gaps, poorly resolved edges and vertical surfaces. These gaps generally occur on the outer hull as well as in the cargo holds. On the *Hetty Taylor,* excessive deposits of sand on the aft of the deck limit the detail that can be extracted in the model. In addition, traces of a railing leading from the

bow to the stern exist in the model but are not fully modeled due to the lack of oblique imagery.

Discussion

Our results suggest that archival video surveys of large-scale archaeological sites can be used to produce detailed 3-D models for further study. Even though the original video surveys were not conducted for the purpose of SfM, we were still able to generate 3-D models of large portions of the wreck sites. In our case, the success of the 3-D modeling is probably due to initial image acquisition being in support of 2-D mosaic creation. Video image collection ensured a high degree of overlap between images allowing for a high number of matched points during model creation. The ability of archived video collected from less coordinated video surveys to create 3-D models has not yet been assessed, however, randomly collected photographs and video footage of terrestrial sites has been used to successfully create 3-D models of major landmarks such as the Roman Colosseum (Agarwal et al., 2011), suggesting the approach should work underwater.

Our models lack coverage of the sides of the vessels, again, largely because the initial video survey effort was to support 2-D mosaic creation. Surveys for mosaic creation are analogous to aerial surveys and result in a high degree of coverage in the horizontal spatial plane, but lacked sufficient oblique photographic coverage to resolve high visual detail in the vertical direction. The relatively low error values derived from this comparison illustrate the possibilities of creating a full 3-D model with adequate video coverage. Aiming for coverage that included both above and oblique angle photos is crucial to resolve complicated surfaces (Demesticha et al., 2014). The need for dense

video coverage for accurately resolving complicated surface features is noticeable in the lower degree of convergence between the 3D model and the wreck map of the *Hetty Taylor* compared to the *Home.* The *Home's* shape, being more regular (i.e. less damaged), allowed for more accurate model construction, whereas improving the accuracy in the *Hetty Taylor* would have required detailed videography in areas that had been badly broken.

Measurement errors in our study are similar to those of McCarthy and Benjamin (2014). In our case, measurements with errors greater than 5% occurred on the smallest measurements and represent a difference of 0.06-0.22 m. Similar to McCarthy and Benjamin (2014), we found that measurement error increased as an inverse function of object size. This error likely results from two sources. First, the 3D models derive their spatial information primarily from measurements of vessel length and width. Small, centimeter-scale measurement errors over measurement distance of 1s to 10s of meters are less significant when measuring objects of that are several meters in length. Measurement errors of a few centimeters, however, become far more significant when measuring objects that are few centimeters in length. The second source of measurement error results from alignment mistakes due to pencil and pixel widths during model adjustment in 3DS Max. Small errors in alignment could easily have scales of 10s of centimeters. Determining the degree to which measurement errors in our study result from measurement error during hand surveys or alignment error is not possible with data available.

It is important to note that we could have created 3D models without the wreck maps, however, generation of spatial information requires that some method of aligning and scaling the output model to a reference system. In our study, scaled wreck maps allowed us to align the models in a 3-D virtual environment and then conduct our measurements. Without such maps, our models could not have been used for measurements, only visual interpretation. To facilitate the accurate adjustment of the models to a measurable reference system many studies have used a combination of GCP markers located prior to photographic surveys (Diamanti et al., 2011, Skarlatos et al., 2012, Demesticha et al., 2014, McCarthy and Benjamin, 2014), the placement of scale bars within the cameras view to allow for absolute scaling (De Reu et al., 2013, McCarthy and Benjamin, 2014) or GPS where possible (Henderson et al., 2013). When working with archival video data, these types of spatial information may not be available. On sites were sonar data was also collected, it should be possible to use sonar surveys as a means of georeferencing the model, however, we did not assess this approach during our study. Finally, any known measurements, blueprints or sources of knowledge pertaining to the construction of the objects should also be useful for model georeferencing. If no spatial information is available to support georeferencing, the 3-D models still remain useful tools to support 3-D visualization by researchers and for outreach purposes.

In comparison to other methods of 3-D modeling maritime archaeological sites, SfM has proved to be the most inexpensive in terms of application. The time required to conduct a thorough photographic survey is much less than that required for full site mapping through trilateration. In addition, the essential equipment needed is only a good

underwater camera with a light source. For shallow, clear water sites, lighting is generally not an issue. The application of 3-D sonar scanners can produce highly detailed results when coupled with optical data (Drap et al., 2014), but the general cost remains high, well beyond many budgets. Even when the commercial software costs, needed for post processing of images for SfM, are taken into account, the overall budget remains well below the cost of a 3-D sonar scanner. Use of SfM obviously requires water with some visibility; however, the minimum visibility requirement has yet to be established.

When modeling SfM, there are a variety of both commercial (e.g. 3DF Zephyr, PhotoModeler and 123D Catch) and open-source software packages (e.g. Bundler, PMVS, VisualSFM, or SLAM) available. AgiSoft Photoscan software package (AgiSoft 2014), used in this study has a commercial price of 3400 USD, but an educational license price of 550 USD, making it reasonably priced for academically funded projects. Agisoft Photoscan is both powerful and very easy to use (McCarthy and Benjamin, 2014). Other options include open source software combinations of Blunder and Patch Based Multi-View Stereo, which is comparable in function to Agisoft's Photoscan (Verhoeven et al., 2012, De Reu et al., 2013, Olson et al., 2013) or custom algorithms such Simultaneous Localization and Mapping (SLAM) (Pizarro, 2004).

One of the most important aspects of the application of SfM to archival media is the potential to visually display these sites in a new way. Even without data for scaling and adjustment, the model allows objects to be manipulated in virtual space, viewed from multiple angles, zoomed in on and studied in detail. These models can be used as an interactive resource for teachers and students. Instead of showing a 2-D photograph or

drawing, students can see the true form of objects they are studying. In addition to an academic setting, the models can also be used to display archaeological sites to the public (Drap et al., 2007, De Reu et al., 2013). 3-D rendering programs can now be used to produce realistic a fly through, using the model as a base from which to build (McCarthy and Benjamin, 2014).

Conclusion

Archival video surveys can be used as a unique source of data for SfM construction of maritime archaeological sites. Resulting models allow researchers the ability to analyze sites spatially and visually post image acquisition. The method of extracting images from video surveys, which allows for a high degree of image overlap during image acquisition, opens up an even more rapid and data-rich way of conducting underwater surveys. While our study emphasized the use of archival video, our results indicate that by planning a survey to get complete coverage of the site a full, high resolution, visually stunning model can be created. With appropriate sources of data for model alignment, accurate measurements can be made from computer models as opposed to in the field, saving researcher both time and money. In addition, these models are a new and exciting tool for displaying these intriguing sites to the public and allow almost a fully immersive experience.

Acknowledgements

J Mertes and J Gulley acknowledge funding from the Department of Geological and Mining Engineering and Sciences. T Thomsen acknowledges funding from University of Wisconsin Sea Grant Institute. We thank three anonymous reviewers for comments that

improved the quality of this manuscript. In addition, we thank Berit Jakobsen from the University Centre in Svalbard for help with literature acquisition while the lead author was resident in Svalbard, Tusen Takk.

References Cited

Agarwal S, Furukawa Y, Snavely N, Simon I, Curless B, Seitz SM, Szeliski R. 2011. Building rome in a day. Communications of the ACM **54**: 105-112

Agisoft, 2014. Agisoft PhotoScan User Manual. In *Professional Edition, Version 1*. Agisoft LLC: http://www.agisoft.ru/pdf/photoscan_pro_1_0_en.pdfhttp://www.agisoft.ru/pdf/photoscan_pro_1_0_en.pdf, http://www.agisoft.ru/pdf/photoscan_pro_1_0_en.pdf

Ballard RD. 1989. The Bismarck Found. National Geographic **176**: 622-637

Ballard RD, Michel J-L. 1985. How we found Titanic. National Geographic **168**: 696-719

Bass GF. 1966. Archaeology under water. Frederick A. Praeger: New York

Bass GF, Katsev ML. 1968. New tools for underwater archaeology. Archaeology **21**: 164-173

Bazeille S, Quidu I, Jaulin L, Malkasse JP, 2006. Automatic underwater image pre-processing. In *Proceedings of Caracterisation du Milieu Marin (Marine Environment Characterisation)*: Brest, France

Beall C, Lawrence BJ, Ila V, Dellaert F, 2010. 3D reconstruction of underwater structures. In *Intelligent Robots and Systems (IROS), 2010 IEEE/RSJ International Conference on*; 4418-4423. DOI: 10.1109/IROS.2010.5649213

De Reu J, Plets G, Verhoeven G, De Smedt P, Bats M, Cherretté B, De Maeyer W, Deconynck J, Herremans D, Laloo P, Van Meirvenne M, De Clercq W. 2013. Towards a three-dimensional cost-effective registration of the archaeological heritage. Journal of Archaeological Science **40**: 1108-1121. DOI: http://dx.doi.org/10.1016/j.jas.2012.08.040

Demesticha S, Skarlatos D, Neophytou A. 2014. The 4th-century BC shipwreck at Mazotos, Cyprus: New techniques and methodologies in the 3D mapping of shipwreck excavations. Journal of Field Archaeology **39**: 134-150

Diamanti E, Georgopoulos A, Vlachaki F, 2011. Geometric documentation of underwater archaeological sites. In *XIII CIPA International Symposium*: Prague

Doneus M, Verhoeven G, Fera M, Briese C, Kucera M, Neubauer W, 2011. From deposit to point cloud: a study of low-cost computer vision approaches for the straightforward documentation of archaeological excavations. In *XXIIIrd International CIPA Symposium*, Pavelka K (ed): Prague, Czech Republic; 81-88 6, http://hdl.handle.net/1854/LU-2038452

Drap P. 2012. Underwater photogrammetry for archaeology. Special Applications of Photogrammetry, DC da Silva, Ed. InTech: 111-136

Drap P, Merad D, Boï J-M, Mahiddine A, Peloso D, Chemisky B, Seguin E, Alcala F, Bianchimani O. 2014. Underwater Multimodal Survey: Merging Optical and Acoustic Data. In *Underwater Seascapes*. Springer; 221-238

Drap P, Seinturier J, Scaradozzi D, Gambogi P, Long L, Gauch F, 2007. Photogrammetry for virtual exploration of underwater archeological sites. In *Proceedings of the 21st International Symposium, CIPA 2007: AntiCIPAting the Future of the Cultural Past: Athens (Greece), 01–06 October 2007*. Citeseer

Green JN. 1973. An underwater archaeological survey of Cape Andreas, Cyprus, 1969–70: a preliminary report. Marine archaeology: 141-79

Green S, Bevan A, Shapland M. 2014. A Comparative Assessment of Structure from Motion Methods for Archaeological Research. Journal of Archaeological Science **46**: 173-181. DOI: 10.1016/j.jas.2014.02.030

Henderson J, Pizarro O, Johnson-Roberson M, Mahon I. 2013. Mapping Submerged Archaeological Sites using Stereo-Vision Photogrammetry. International Journal of Nautical Archaeology **42**: 243-256

Howard P. 2006. Archaeological surveying and mapping: recording and depicting the landscape. Routledge

Iqbal K, Salam RA, Osman A, Talib AZ. 2007. Underwater Image Enhancement Using an Integrated Colour Model. IAENG International Journal of Computer Science **34**: 529-534

Klein M. 2002. Side Scan Sonar. In *International Handbook of Underwater Archaeology*, Ruppé C, Barstad J (eds). Springer US; 667-678. DOI: 10.1007/978-1-4615-0535-8_39

Ludvigsen M, Eustice R, Singh H, 2006. Photogrammetric models for marine archaeology. In *OCEANS 2006*; 1-6. DOI: 10.1109/OCEANS.2006.306915

McCarthy J, Benjamin J. 2014. Multi-image Photogrammetry for Underwater Archaeological Site Recording: An Accessible, Diver-Based Approach. Journal of Maritime Archaeology **9**: 95-114. DOI: 10.1007/s11457-014-9127-7

Meverden KN, Jensen JO, 2004. Hetty Taylor Shipwreck (schooner). In *National Register of Historic Places Nomination Form. Manuscript on file.* Wisconsin Historical Society: Division of Historic Preservation and Public History: Madison, Wisconsin

Meverden KN, Thomsen TL, 2010. Home Shipwreck (schooner). In *National Register of Historic Places Nomination Form. Manuscript on File*. Wisconsin Historical Society: Division of Historic Preservation and Public History: Madison, Wisconsin

Nicosevici T, Garcia R, 2008. Online Robust 3D Mapping Using Structure from Motion Cues. In *OCEANS 2008 - MTS/IEEE Kobe Techno-Ocean*; 1-7. DOI: 10.1109/OCEANSKOBE.2008.4531022

Olson BR, Placchetti RA, Quartermaine J, Killebrew AE. 2013. The Tel Akko Total Archaeology Project (Akko, Israel): Assessing the suitability of multi-scale 3D field recording in archaeology. Journal of Field Archaeology **38**: 244-262. DOI: 10.1179/0093469013Z.00000000056

Pizarro O. 2004. Large scale structure from motion for autonomous underwater vehicle surveys. Massachusetts Institute of Technology/Woods Hole Oceanographic Institution joint program: PhD-thesis. Ocean Science and Engineering. Ph.D. http://dspace.mit.edu/handle/1721.1/39185.

Pollio J, 1968. Applications of underwater photogrammetry. Naval Oceanographic Office: Washington D.C.

Rosencrantz DM. 1975. Underwater photography and photogrammetry. Photography in Archaeological Research, School of American Research, University of New Mexico Press (Albuquerque 1975) **265**: 310

Sedlazeck A, Koser K, Koch R, 2009. 3D reconstruction based on underwater video from ROV Kiel 6000 considering underwater imaging conditions. In *OCEANS 2009 - EUROPE*; 1-10. DOI: 10.1109/OCEANSE.2009.5278305
Singh B, Mishra RS, Gour P. 2011. Analysis of Contrast Enhancement Techniques For Underwater Image. International Journal of Computer Technology and Electronics Engineering (IJCTEE) **1**: 5
Singh H, Adams J, Mindell D, Foley B. 2000. Imaging underwater for archaeology. Journal of Field Archaeology **27**: 319-328
Skarlatos D, Demestiha S, Kiparissi S. 2012. An 'open'method for 3D modelling and mapping in underwater archaeological sites. International Journal of Heritage in the Digital Era **1**: 1-24
Verhoeven G. 2011. Taking computer vision aloft–archaeological three-dimensional reconstructions from aerial photographs with photoscan. Archaeological Prospection **18**: 67-73
Verhoeven G, Doneus M, Briese C, Vermeulen F. 2012. Mapping by matching: a computer vision-based approach to fast and accurate georeferencing of archaeological aerial photographs. Journal of Archaeological Science **39**: 2060-2070. DOI: http://dx.doi.org/10.1016/j.jas.2012.02.022

Chapter 2. Rapid, Quantitative Assessment of Submerged Cultural Resource Degradation using Repeat Video Surveys and Structure from Motion[2]

Abstract

Monitoring, managing and preserving submerged cultural resources (SCR) such as shipwrecks can involve time consuming detailed physical surveys, expensive side-scan sonar surveys, the study of photomosaics and even photogrammetric analysis. In some cases, surveys of SCR have produced 3-D models, though these models have not typically been used to document patterns of site degradation over time. In this study, we report a novel approach for quantifying degradation and changes to SCR that relies on diver-acquired video surveys, generation of 3-D models from data acquired at different points in time using structure from motion, and differencing of these models. We focus our study on the shipwreck *S.S. Wisconsin*, which is located roughly 10.2 km southeast of Kenosha, Wisconsin, in Lake Michigan. We created two digital elevation models of the shipwreck using surveys performed during the summers of 2006 and 2015 and differenced these models to map spatial changes within the wreck. Using orthomosaics and difference map data, we identified a change in degradation patterns. Degradation was anecdotally believed to be caused by inward collapse, but maps indicated a pattern of outward collapse of the hull structure, which has resulted in large scale shifting of material in the central upper deck. In addition, comparison of the orthomosaics with the difference map clearly shows movement of objects, degradation of smaller pieces and in some locations, an increase in colonization of mussels.

---

[2] The material in this chapter has been submitted for review to the Journal of Maritime Archaeology October 21, 2016

Introduction

The preservation and management of submerged cultural resources (SCRs), such as shipwrecks, is a difficult endeavor. Although there has not been extensive publication on specific best practices for monitoring SCRs over time, there have been isolated projects and studies on the effectiveness of different monitoring techniques. Traditionally, SCR managers relied upon physical surveys, photomosaics, side scan sonar, and photogrammetry to monitor change and make decisions. Many of the existing discussions about site degradation over time have focused on general guidelines for preservation and monitoring (Canada, 2005), encompassed large scale projects with advanced computer programs and multiple agencies (Green et al., 2002, Palma, 2005, Foecke et al., 2010, Bates et al., 2011), focused on the theoretical concept of site formation processes for site analysis (Ward et al., 1999, Horlings, 2011), or consist of initial site assessments and recommendations (Murphy, 1993, Morris and Lima, 1996, Murphy, 1998, Russell, 2004, Russell and Murphy, 2013). Many other studies have focused specifically on conservation and techniques for *in situ* preservation, or reburial, after initial survey (Wheeler, 2002, Björdal and Nilsson, 2008, Gregory et al., 2012).

In general, these past studies have produced detailed archaeological information, and in some cases, detailed 3-D models of various maritime resources, but they have not primarily focused on comparative analyses of site degradation over time. Monitoring and site degradation studies necessarily must be conducted over a series of years. Common methodologies for monitoring sites usually involve a series of physical surveys at regular intervals but these techniques can be costly, labor intensive and difficult to achieve when

a site is difficult to reach either due to depth or location. To reduce economic and labor costs associated with traditional, hand-based site surveys, a few notable studies in recent years have begun to develop methods of using photogrammetry (Ludvigsen et al., 2006, Henderson et al., 2013, McCarthy, 2014).

One of the earliest forays into a modern photogrammetric methodology in maritime archaeology was a three-dimensional model of the wreck of the J3 submarine in Australia. Franke (1999) used EOS Systems program PhotoModeler Pro in an attempt to create an accurate representation of the submarine. To complete his analysis, Franke used historic images of the submarine for comparison. Though innovative, the methodology had certain limitations. The site was semi-submerged, and, due to the obstacles of capturing photogrammetric models underwater, the results of the study were limited to a three-dimensional rendering of only above-water sections of the submarine (Franke, 1999). Although Franke proved that his technique was a valid methodology for aiding in site analysis, it did not extend beyond the initial survey, and monitoring of the site using this procedure was ultimately not conducted.

Researchers in the Institute of Nautical Archaeology (INA) used PhotoModeler to survey and analyze a 5th century shipwreck off the western coast of Turkey over the course of three field seasons (Green et al., 2002). PhotoModeler was used in lieu of extensive triangulation by divers to create a three-dimensional representation of 250 to 300 amphorae on the site. To resolve the issue of defining the site's location in three-dimensional space, specific target points and control grids were manually placed on the mouth of each amphora to be used as control points to gather accurate results. These

points could then be used by the software to provide an accurate scale and mapping control. Accuracy was further improved by adding small, 1m control grids around artifacts. Additional photographs were taken at greater distances above the site to link the artifacts to the control points. The target points allowed three sets of X, Y, and Z coordinates to be produced, which could then be associated with a wire frame of an artifact created in Rhinoceros (Rhino). Using Rhino, each artifact was placed in its exact location, fully rendered, within the model.

In addition to using Photomodeler, Green et al. (2002) also used VirtualMapper software to accurately model the seafloor in a three-dimensional space around the site. The process involves taking two photographs in stereo and using the computer program to allow the user to manually float a curser to a particular point, thus providing X, Y, and Z coordinates. These coordinates can be extrapolated to place other objects within the three-dimensional space, removing the need to have multiple precise targets, and allowing the model to be placed within its relative location on the seafloor (Green et al., 2002). Although the impetus for using photogrammetry in this setting was focused on initial site recording, the models produced and the methodology presented leave the possibility for additional site surveys and potential comparative analysis, though none have yet to be undertaken. While this method did alleviate many of the logistic obstacles of a traditional underwater survey, such as time in the water and accuracy of data, it remained complex and required extensive post processing and multiple computer programs for rendering.

More recently, archaeologists from the National Park Service, Submerged Cultural Resources Center worked with scientists from the National Institute of Standards and Technology in developing a methodology to study the degradation of the *USS Arizona*. By developing a finite element model (FEM) of a 25m section of the *Arizona* archaeologists were able to determine the current condition of the site, compared to its condition upon its sinking, in an attempt to better understand how the site will deteriorate as it corrodes for long-term site monitoring. Using computer software, the study was able to produce a detailed model of the midsection of the *Arizona* that could have its density changed based on known corrosion rates. The results of this study produced prediction models for various rates of the metal hull's corrosion based on stress levels. By applying increasing percentages of stress on the components of the model, the archaeologists were able to visualize how much the *Arizona* has already collapsed, and how the vessel will likely continue to corrode and collapse in the future (Foecke et al., 2010). With the use of the FEM models, a systematic method of monitoring the Arizona was established, but the process still involves complex and time consuming methods of model creation and analysis.

Although effective, many of these methods listed above are time consuming and expensive, and without access to large scale funding or time, they remain out of reach for many small agencies and research groups. Structure from Motion (SfM) offers a cost-effective alternative to extracting spatial information and/or creating 3-D models from diver acquired photographs or video stills. While there are a variety of commercial and open source software packages (e.g. Bundler, Python Photogrammetry Toolbox,

3DFlow), AgiSoft PhotoScan is the most widely used due to its intuitive Graphical User Interface. The process of extracting geometric information from imagery using the SfM method uses feature-matching algorithms to detect features in multiple images and generate a sparse point cloud. By doing so, it is possible to calculate not only the relative exterior orientation of the image planes (i.e. x, y, z yaw, pitch, roll), but also the interior orientation of the camera itself (e.g. focal length, distortion coefficients). Having calculated the positions of the camera, using Multiview stereo software, locations of more of the remaining overlapping pixels can be determined and a dense point cloud is created (Agarwal et al., 2011). By adding ground control points (GCPs) with X, Y, Z values at known points on the model, it is possible to scale the resulting model to a known reference system and create accurate three-dimensional digital elevation models with little residual error (e.g. Mertes et al., 2014).

Differencing multiple digital elevation models (DEM) for the purpose of detecting changes in shape and quantifying their magnitudes, is a method that is commonly used in the geosciences. Two DEMs of the same surface are generated and aligned such that when elevation values for each aligned pixel from the latter DEM are subtracted from the earlier DEM, areas of deposition and erosion will result in positive and negative changes to elevation, respectively. DEM differencing is widely used to investigate changes in glacier volume (Etzelmüller, 2000, Rippin et al., 2003, Nuth et al., 2010, Bolch et al., 2011, Kääb et al., 2012, Thompson et al., 2016), river and coastal erosion rates (Lane et al., 2003, De Rose and Basher, 2011, Williams et al., 2011, Gibbs et al., 2015, Obu et al., 2016) and even detection of volcanic deformation (Walder et al., 2004).

In this study, we investigate the potential of SfM and DEM differencing as a quantitative monitoring tool for mapping patterns of degradation in shipwrecks and other SCRs. Using SfM, we created two DEMs of an early 20th century shipwreck using still frames extracted from separate diver acquired video surveys. By differencing these DEMs, we were able to rapidly map and detect changes, such as large scale collapsing both inward and outward, movement of objects or shifting of surfaces and, even assess changes in local flora and fauna.

Study Site

The S.S. Wisconsin

The remains of the iron package steamer *Wisconsin* rests in 38 m of water, 10.2 km southeast of Kenosha Wisconsin (Figure 2.1). Built in 1881 at the Detroit Dry Dock Company in Wyandotte, Michigan, the *Wisconsin* was originally part of the break bulk cargo trade, ferrying goods across Lake Michigan for the Goodrich Transportation Company. During its 48 years of service, the *Wisconsin* served Lake Michigan's cross lake freight trade under many different names and owners, before returning to the name *Wisconsin*. The *Wisconsin* was lost 29 October 1929 due to an unknown leak during a violent storm while in route from Chicago to Milwaukee. Today the *Wisconsin* lies upright and mostly intact on the lakebed. The lower portion of the wreck exhibits excellent preservation, while its upper decks have long since collapsed. The contents of the *Wisconsin*'s final cargo remain intact within the vessel's hull. Although the site retains extensive archaeological integrity, diver reports have indicated that the site has degraded rapidly in recent years.

Figure 2.1: Overview map showing location of SS Wisconsin shipwreck approximately 10.2 km SE of Kenosha Wisconsin (© Google, 2016, Landsat Image NOAA).

The *Wisconsin* is a rare example of a vessel type that was vital to Great Lake's economy (Figure 2.2). Year-round steamers like the *Wisconsin* were an important link for railroad freight traffic connecting Wisconsin's communities economically with wider regional and national markets. As one of the few iron package steamers in Wisconsin waters, the site is an archaeological rarity, and still has the potential to yield further archaeological information. The *Wisconsin* was listed on the National Register of Historic Places on 7 October 2009 (Thomsen and Meverden, 2010).

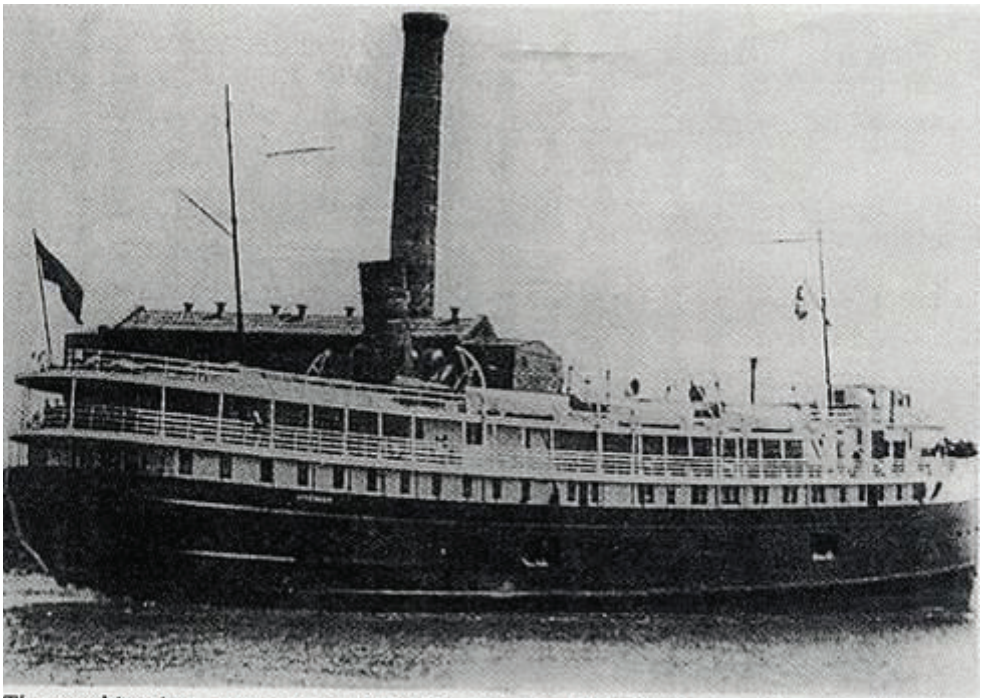

Figure 2.2: Archive photograph of the S.S. Wisconsin during operation (Data source: Wisconsin Marine Historical Society).

Methodology

Surveys

Divers conducted photographic and hand surveys of the *S.S. Wisconsin* in July 2006, 2007 and again in July 2015. In 2007, divers completed a full Phase II archaeological survey of the *S.S. Wisconsin* site, recording detailed measurements of the ship for its National Register of Historic Places nomination. During the 2015 survey, fiberglass measuring tapes were used to determine the vessel's overall length and gain detailed measurements of various sections of *Wisconsin's* hull. Detailed annotated drawings were

produced to indicate location of data collection and to note qualitative observations of change from the 2006 photomosaic of the site. The 2006 photomosaic was printed on sheets of Mylar and attached to plastic slates. Data and notes were recorded on these Mylar sheets with mechanical pencils. All measurements were recorded to a precision of 0.03 m in the X, Y plane to minimize recording errors, and all are assumed to have an accuracy of 0.03 m. These survey measurements were used for triangulating GCPs used for proper scaling of the 2015 3-D model.

The 2006 video survey of the *SS Wisconsin* wreck site was conducted to collect mosaic imagery in July of that year. Divers used a 2003 Sony Handycam video camera, which is owned by Wisconsin Historical Society to collect all video. The camera was mounted in a down facing orientation on the front of a Silent Submersion UV-26 diver propulsion vehicle (DPV) and piloted approximately 20 feet above the shipwreck (Figure 2.3). The video was shot using ambient lighting. Depth control of the UV-26 was accomplished using an OMS Bottom Timer as a depth gauge. A bubble level was mounted to the top of the DVP to ensure a down looking position. Overlapping passes of the wreck site and adjacent debris fields were made to collect a full data set. The survey took approximately 35 mins with 8 passes. Still images were captured from the video every 10 seconds with no automation and cataloged by pass. The video was transformed into a collection of still images with the highest resolution at the time, of 72 dpi and dimensions of 640 x 480 pixels.

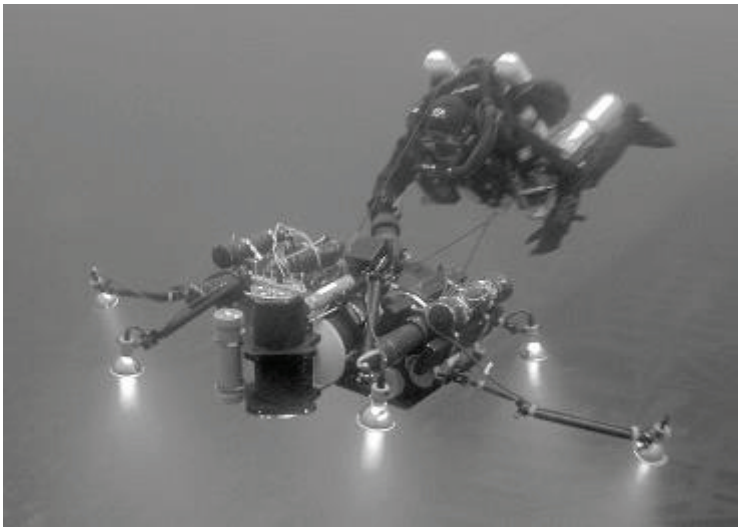

Figure 2.3: Diver operating the Silent Submersion Diver Propulsion Vehicle.

The 2015 video survey of the *SS Wisconsin* wreck site was conducted to collect comprehensive imagery of the site for 3D visualization purposes. Divers used a Canon 5D Mark II camera with an Aquatica 9.25" mega glass dome port housing, to collect all video. The lens used was a Canon 16-35mm II F2.8. The camera was mounted in a down facing orientation on the front of a Dive X DPV and piloted approximately 20 feet above the shipwreck. The video was shot using an array of four 50W Light Monkey HIDs with reflectors, mounted to the DPV with depth compensating arms. The arms were adjusted at depth for appropriate light coverage. Depth control of the DPV was accomplished using a Hammerhead Rev. D dive computer as a depth gauge. A bubble level was mounted to the top of the DVP to assure down looking position. Overlapping passes of the wreck site and adjacent debris fields were made to collect a full data set. The survey took approximately 1 hour and 30 mins with 12 passes.

Still images were extracted from each survey dataset at a frequency of every 10-15 frames using a custom MATLAB code that automates the process (Mertes et al., 2014). Stills from the 2015 survey were down sampled to roughly the same resolution as the 2006 survey. Downsampling was performed to reduce errors due to resolution differences as well as speed up processing time. Still image extraction resulted in 1754 images from the 2006 survey and 3580 images for the 2015 survey that were then used for reconstruction of the 3-D shipwreck model.

Model Generation using Agisoft Photoscan

Model reconstruction was performed using Agisoft Photoscan SfM software package version 1.1.6 build 2038- 1.2.4 build 2399 (64 bit). Images were imported into Photoscan and processed following a similar approach as in Mertes et al. (2014). The processing was performed on a custom-built laptop running an Intel© Core™ i7-6700 4.00 GHz with eight cores and 64Gb of memory. The 2006 model took roughly two hours of processing time whereas the 2015 model took 16 hours due to the larger image size and quality.

The initial alignment produced sparse point clouds of 548,897 points and 452,904 points for 2006 and 2015 respectively. These point clouds were next filtered using the *Gradual Filter* function and points with reprojection errors of greater than ~0.5 were removed along with points having reconstruction uncertainties of greater than 25. This step is recommended in the Agisoft manual to help improve the accuracy of resulting optimization steps and bundle adjustments by removing points with larger potential error (Agisoft, 2014).

Secondly, a visual inspection of the point cloud was made to remove leftover points that appear to be erroneous and not conforming to the known shipwreck shape (e.g. far away points) which often result from low angle photographs. The final sparse point clouds of each survey after filtering had 406,142 points and 156021 points for 2006 and 2015 respectively.

In order to apply proper scaling to the models, ground control points (GCPs) were placed on the 2006 model with the origin located at the tip of the bow increasing in distance towards the stern with negative values to starboard and positive to the port side. We have used this method of relative positioning due to the fact that the original survey was not conducted with the intent of generating a 3D model and no ground truthing was performed. Future investigations of SCR sites would benefit from the implementation of permanent marker points around the site that could be accurately measured and visible in each video surveys. Stable, non-movable GCPs would allow rapid model scaling without the need for extensive measurements and triangulation of GCPs.

In Photoscan, markers were placed at their identified locations in a few photographs and assigned their corresponding triangulated X, Y values (Figure 2.4). Agisoft recommends 10 GCPs as a minimum when georeferencing models (Agisoft, 2014), yet for this study, as we are only interested in relative change between the two scenes, we used less than this. In addition, our GCPs are positioned on objects that we assumed have undergone little to no change, based on visual inspection of the model orthomosaic. Since the sparse alignment has previously been performed, Photoscan is then automatically able to determine in which other photos each specific GCPs occurs. Visual inspection of these

automatically assigned markers must be done to assure correct placement. After every GCP had been located and adjusted in their corresponding images, we optimized the model a second time, thereby improving overall accuracy through a bundle adjustment.

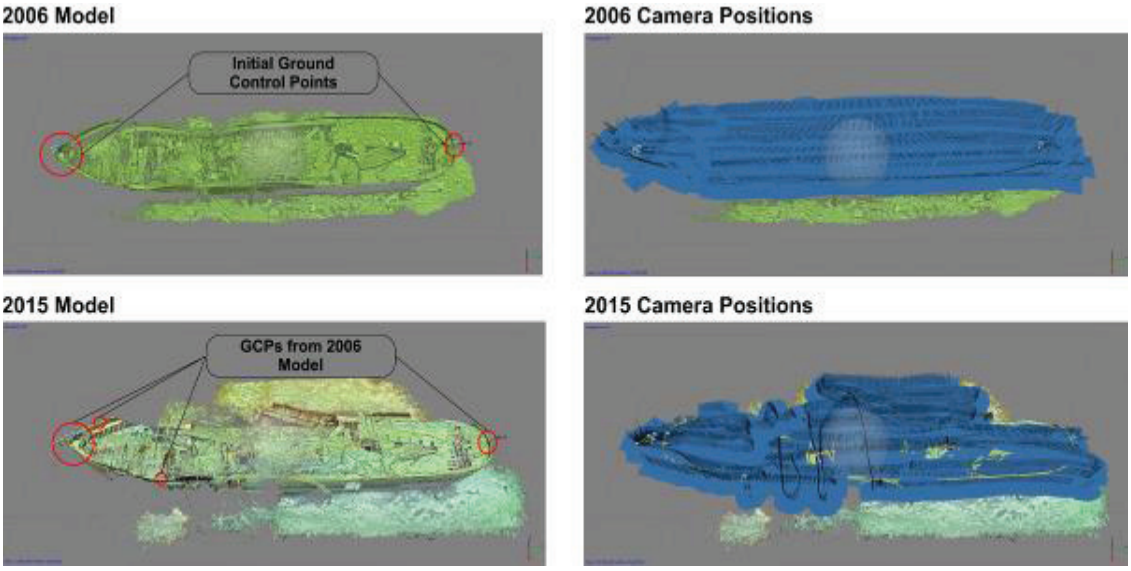

Figure 2.4: Locations of GCPs and cameras for the 2006 and 2015 models, shown over Photoscan shaded meshes.

Generating dense point clouds took 18 minutes for the 2006 model and 4hrs for the 2015 model. The resulting dense point clouds contained 7,881,099 points and 6,472,617 points for the 2006 and 2015 models, respectively. Outliers were again removed through visual inspection and then surface meshes were generated. The reconstruction parameters for the surface meshes were of type 'Arbitrary', using the dense point cloud, with interpolation disabled. Quality was set to 'High' and depth filtering (i.e. noise removal) was set to 'Moderate'. This resulted in surface meshes of 19,999,999 faces and 11,539,095 vertices for the 2006 model and 17,452,030 faces and 9,607,632 vertices for the 2015 model.

From these meshes we next generated DEMs with a resolution of 1 cm pixel^{-1} (Figure 4.4).

Orthomosaics were created at a resolution of 0.005 cm pixel^{-1} using the settings 'average' for the color calculation of pixels based on multiple images. These products (i.e. DEM and Orthomosaic) were exported as geotiff files for further analysis using ESRI ArcMap GIS software. The 2006 model was completed first using four GCPs taken from known measurements. The GCPs for the 2015 model were then selected from the 2006 DEM and orthomosaic thereby allowing us to more accurately align the two models.

Results

Models

Creation of models from both surveys was successful for the majority of the upper deck from bow to stern. Considering that the purpose of the 2006 survey was to create a down-looking photomosaic, minimal coverage of the hull limited our ability to generate a complete 3-D model. The 2015 survey included collection of video coverage oblique to the hull surface as well as inside the ship's cargo hold, yet initial attempts to build a full model including interior spaces as well as the ship's hull failed due mainly to poor lighting and resolution. In some areas, portions of the hull were successfully extracted, but not with sufficient spatial density to allow comparison between time periods. For this reason, we chose to focus on generating 3-D models from a vertical perspective looking at changes visible on the upper deck as well as surrounding the shipwreck.

The resulting models have 3-D RMSE, based on the GCPs, of 0.27 m and 0.30 m for the 2006 and 2015 models respectively. In the Z direction, the RMSE for 2006 and 2015 is

0.02 m and 0.21 m respectively. Each model has photographic coverage of >9 image overlap over the majority of the area of interest (Figure 2.5).

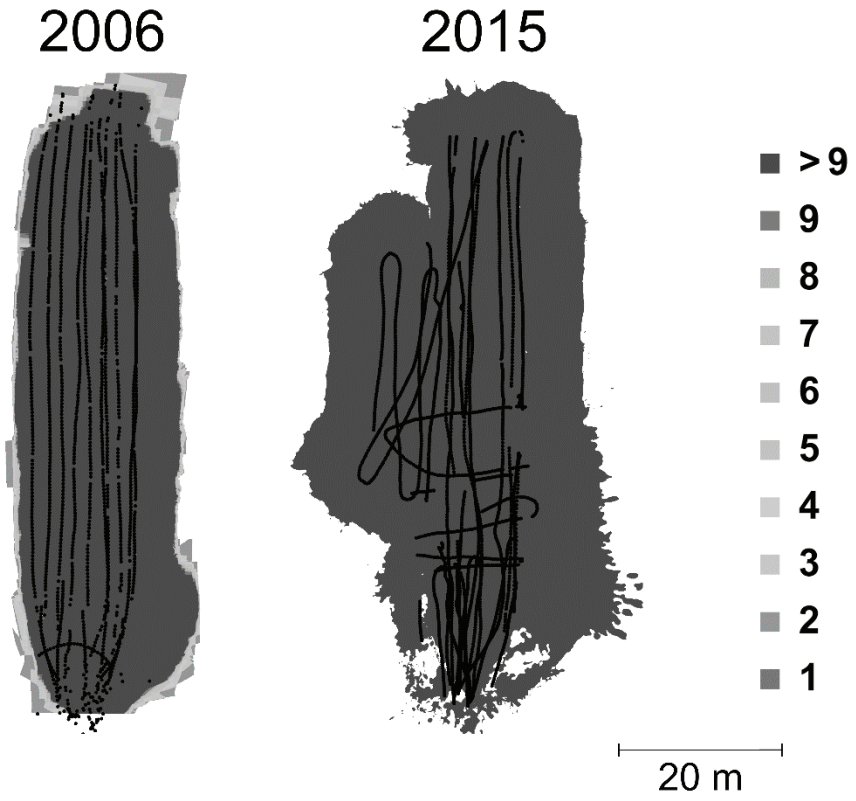

Figure 2.5: Locations of images (dots) and total imagery overlap color map, produced from Photoscan, showing coverage of >9 images over most of the shipwreck site for both 2006 and 2015.

DEM Differencing

By subtracting the height values of the 2006 model from the 2015 model, we created a difference map showing areas that have undergone some type of vertical change over the ~10-year period. We have excluded any changes greater than 5 m and less than -5 m as visual inspection revealed these regions were located in areas of poor model

reconstruction. Assuming minimal changes to the surrounding lakebed area (e.g. low disturbance, slow deposition) we assess the differences in this area to quantify our model error. The middle 50% of our data range from 0.03 to -0.54 m, with ~99% of the data between 0.89 and -1.4 m. Normal and extreme outliers make up only 0.38% of our dataset ($n=3.7*10^6$) (Figure 2.6). We calculate an off ship standard error (σ) of ±0.36 m and an overall mean difference of -0.22 m.

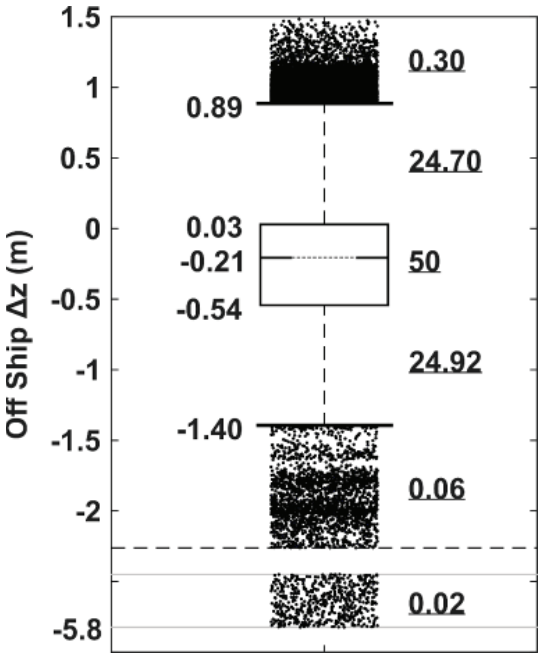

Figure 2.6: Box and whisker plot of off ship DEM differencing values. The gray dash line within the box represents the median while the upper and lower bounds of the box encloses the central 50% of data. The numbers to the left of the box are the upper adjacent the 75th percentile, median, 25th percentile and the lower adjacent. On the right are the percentages of the total data points (n=~3.7*106).

Obvious erroneous regions, identified as interpolated artifacts from the mesh generation, have also been clipped out to allow better visualization of changes within our desired

range. These areas include a small section on the starboard side of the bow and a section near the stern starboard side (Figure 2.7).

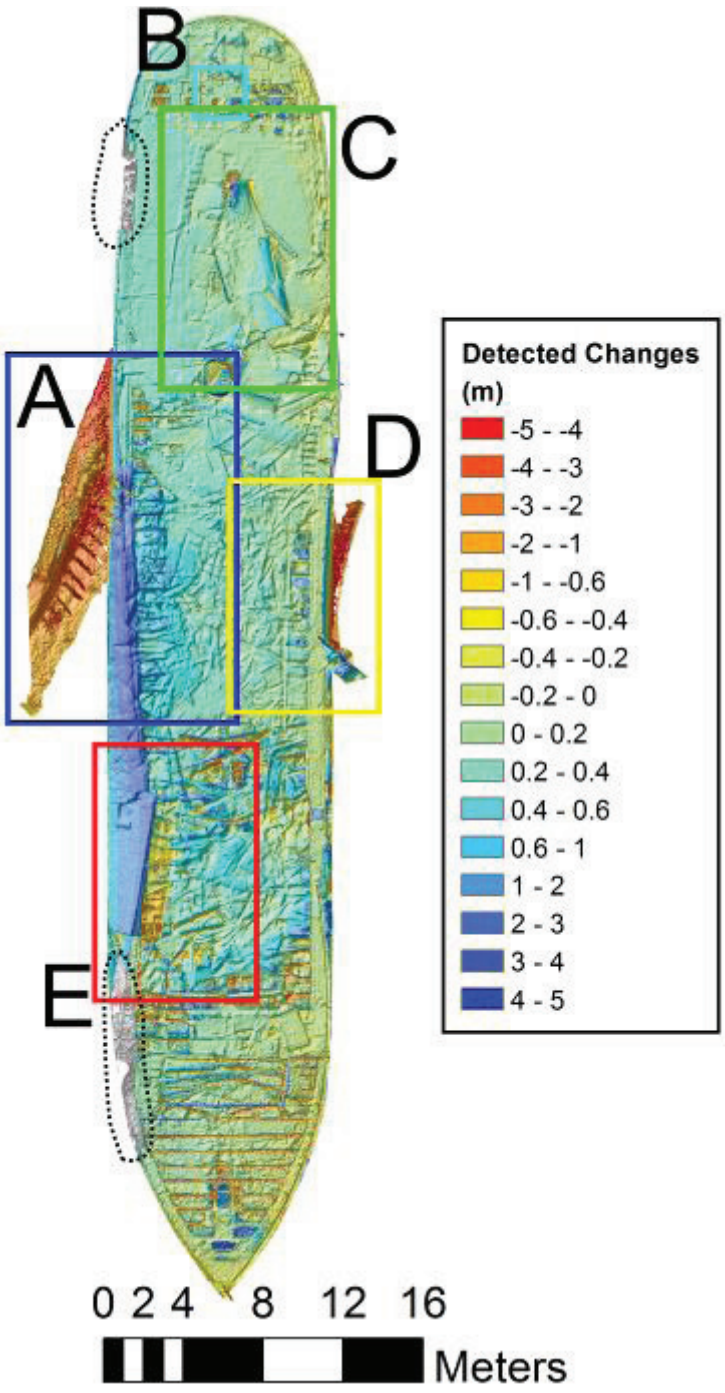

Figure 2.7: Difference map of the 2006 and 2015 models with specific areas of interest identified within labeled boxes. Bordering over interpolated areas that have been removed are indicated by dotted black outlines. Positive values of change indicate areas of decreased elevation whereas negative values indicate an increase in elevation from 2006-2015.

Our results show three large areas of high changes (i.e. ~±2-5 m) occurring mainly in the central region of the ship (Figure 2.7, A, D and E). Smaller areas with changes on the order of ~1 m appear in both the bow and stern regions indicating shifting of objects on the more stable deck (Figure 2.7, B). In the bow region, differences associated with planks extending from starboard to port, which were extracted from one set of imagery, yet not the other, clearly show up as changes of ~1 m (Figure 2.7, Bow). Overall, however, the bow appears to have undergone little change as indicated by the minimal change of the capstan (Figure 2.7). The remainder of the difference map appears to be within our calculated error.

Region A shows an increase in height (negative change) of 3-5 m off the starboard side, whereas along the starboard side from region A through E there is a decrease (positive change) of 0.2 to 4-5 m. Similarly, on the port side there is also a thin region (Figure 2.7, D) indicating a large increase in height bordered by an area of height decrease. These zones (A, D, E) are displaying large-scale collapse features and shifting of major sections of the hull. The central areas within regions A, D, and E have a pattern of increasing change from port to starboard indicating that the deck collapse outward has caused material to shift downward and slide from port to starboard.

Visible Changes

In addition to producing DEMs from underwater surveys, SfM can also produce high-resolution orthomosaics from the imagery and model, which can be used as a complementary source of data to inspect changes to SCRs. The large detected negative change along the aft section of the starboard hull can be attributed to the outward collapse of a 19.8 m section of the hull (Figure 2.8, 1). This outward collapse of the hull appears to have also caused a destabilization to the deck as other material and objects can be seen to have shifted significantly between the two periods (Figure 2.8, 2).

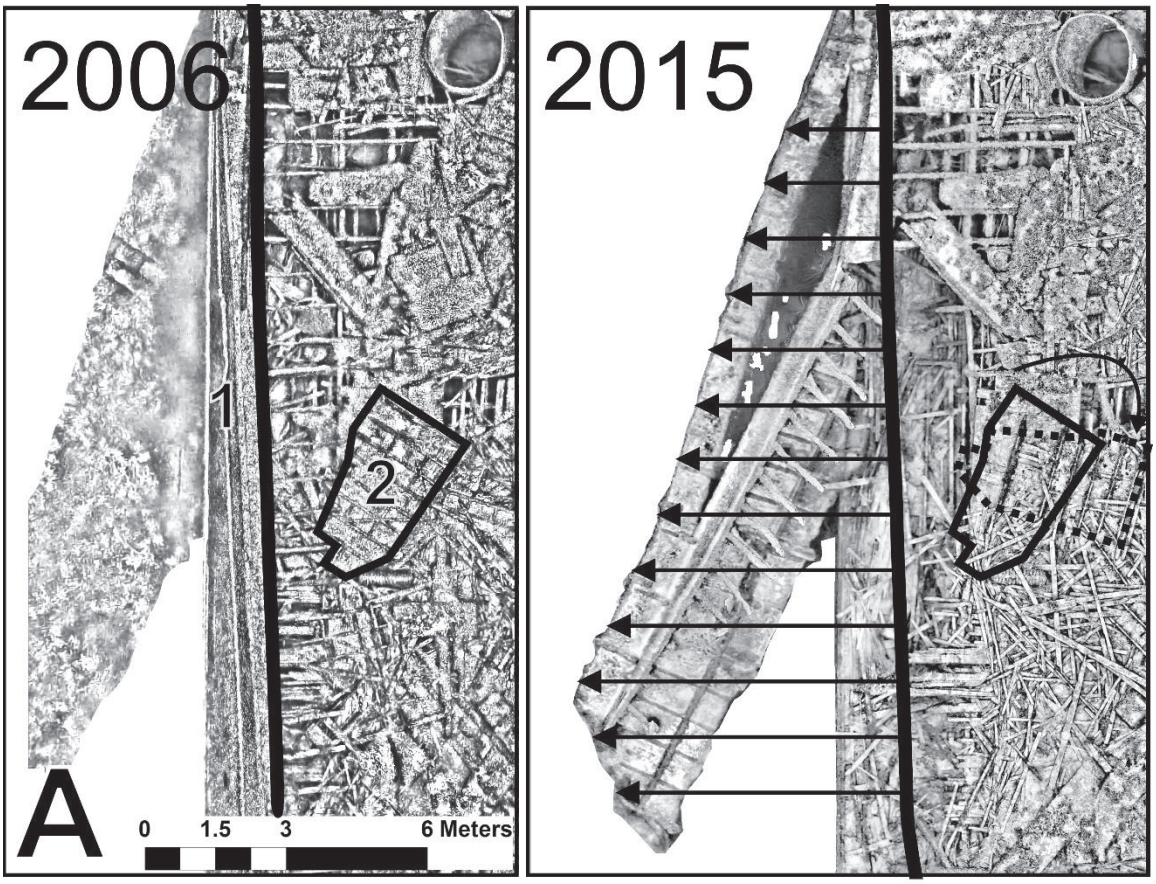

Figure 2.8: Subset A from Figure 2.7 showing the outward collapse of the mid-aft section of the starboard hull (1). As well as observed rotation of a large piece of material (2).

Small scale changes can also be visibly detected as is shown in area B of Figure 2.7. we can visually detect thickening changes on objects such as the steering quadrant and rudder post, as well as on the deck planks and structure around them (Figure 2.9). Smaller magnitude changes detected in the aft section between the smokestack and the stern, which are just above our estimated error, can visibly be attributed to lateral shifting of large planar objects.

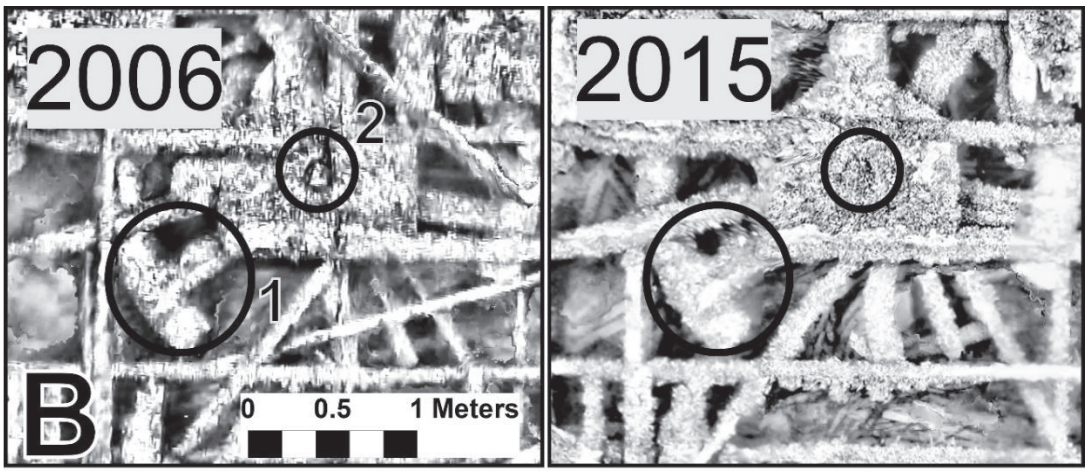

Figure 2.9: Subset B from Figure 2.7 showing the observed buildup of mussels on what is believed to be components of the steering quadrant (1) and the rudder post (2).

A piece of the upper cabin works, roughly 10.6 m in length has shifted towards the port, and begun flexing downward over the aft cargo hold opening (Figure 2.10, 1). In addition, a second large piece of cabin structure has also tipped inward and rotated slightly in an anti-clockwise fashion after it split into multiple pieces (Figure 2.10, 3).

Another object (Figure 2.10, 4) can be observed to have fallen into a void created by the forward shifting of the smokestack (Figure 2.10, 5).

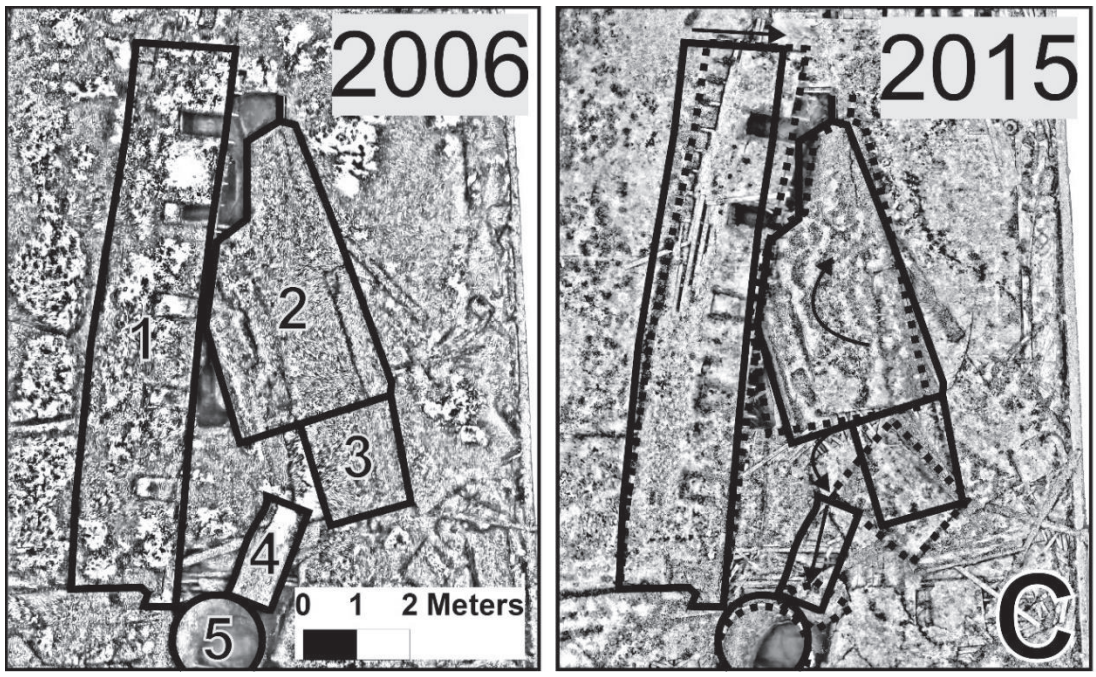

Figure 2.10: Subset C of Figure 2.7 showing shifting of a section of the upper cabin works from starboard to port (1) as well as rotation of another piece (2) caused by what appears to be sliding into the aft cargo hold. Objects 3, 4 and the smokestack (5) have all shifted forward. Object 4 has tipped upward and slid into the void between the deck and smokestack.

On the port side of the ship, where we detected larger changes, we can observe more outward collapse of the ship. A piece of the deck rail has peeled away from the upper hull and folded downward (Figure 2.11, 1). Also, changes can be observed to have occurred to deck planks and other pieces of wood, that could possibly be attributed to the major starboard hull collapsing (Figure 2.11, 2, 3).

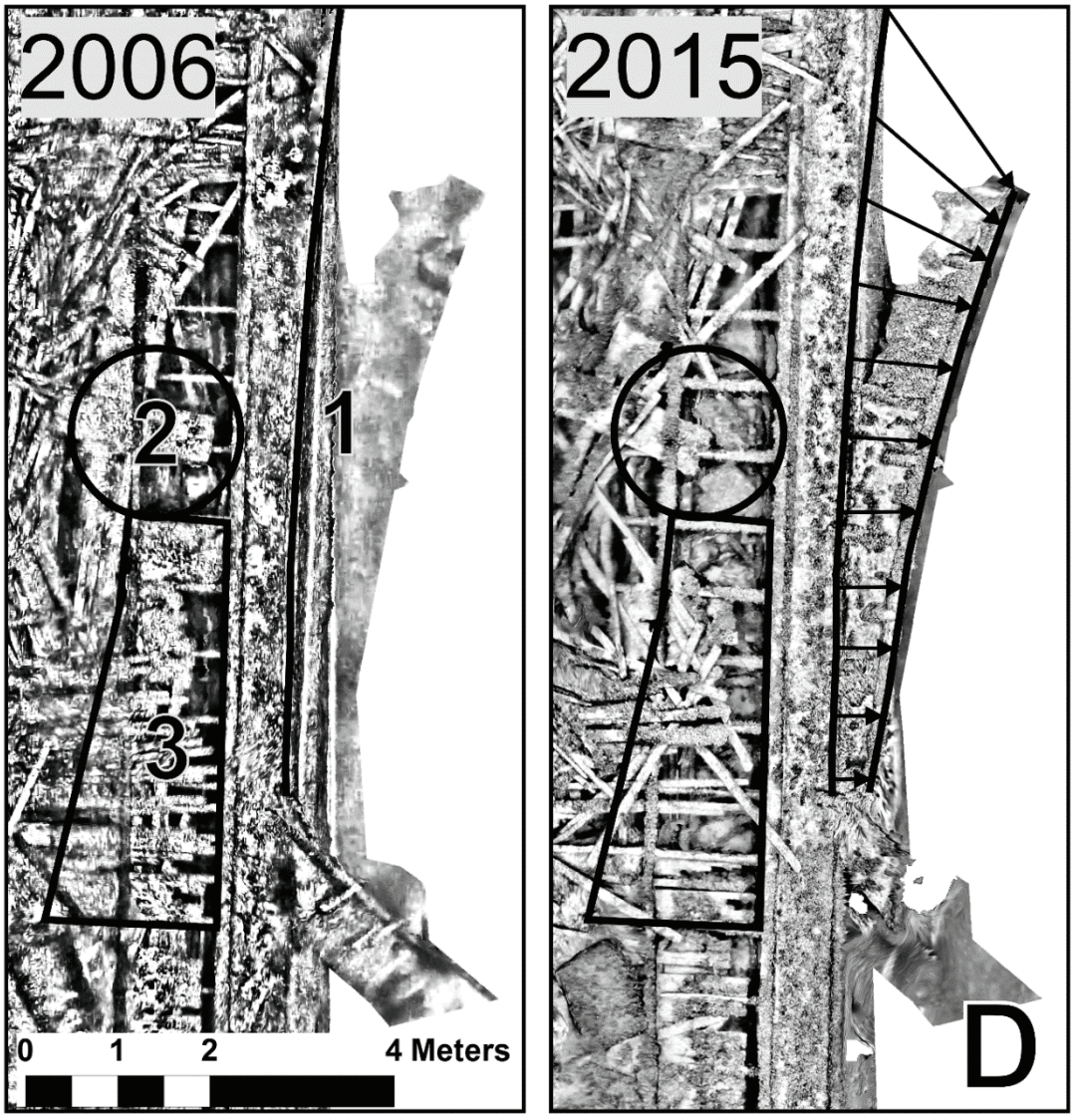

Figure 2.11: Subset D of Figure 2.7 showing the outward collapse of the main railing on the port side (1) as well as degradation and movement of deck material (2, 3) which may have been caused by the outward and inward collapse of the starboard hull (Figure 2.7 A & E).

The collapse of the aft section of the starboard hull outward (Figure 2.8, 1) and the inward collapse of the forward section (Figure 2.12, 1) appears to have caused a decrease in underlying support as well as an increase in pressure from above, respectively. These

changes appear to have caused shifting of material on the deck such as that seen in Figure 2.11 as well as Figure 2.12 (2, 3), downward and to the starboard, effectively increasing the slope of the deck in the port direction.

Figure 2.12: Figure 2.7 subset E showing the two sections of the starboard hull which split and collapsed outward (black arrows, i.e. Figure A) and inward (1) onto the deck material. Changes in the orientation of deck material (e.g. planks) are observed (2) with the appearance of two metal radiator looking objects (3).

Discussion

Our results demonstrate that using SfM and photo/video surveys of SCR sites can yield high-resolution models and orthomosaics, which can aid in management, monitoring, and preservation of SCRs. We have shown that the application of DEM differencing to periodically obtained model of SCR sites is a powerful tool for detecting and quantifying spatial changes. Visual inspection of resulting orthomosaics can allow SCR managers to see changes on a wide variety of scales.

Model Generation

One of the largest difficulties encountered in constructing our models comes from image resolution and lighting. The 2006 video survey was shot at a relatively poor resolution compared to resolution available today. In order to make DEMs of comparable quality, and to speed up processing of large batches of images during DEM construction, we down sampled our 2015 imagery to match the resolution of the 2006 imagery. In many areas of the model, the relatively low image resolution does not seem to cause issues with model creation. In areas of low exposure, or in slightly blurred images, lower detail results in failure to match features across multiple images. The inability to construct a complete hull stems mainly from the fact that the camera angle during filming resulted in inclusion of the lake surface in the upper corner of each frame. The lake surface appears bright from sunlight, in contrast to the hull bottom, which was in shadow. The exposure of the camera adjusted for the brightness, rendering the hull bottom too dark to match features across images. This is also similar to imagery of the upper deck that include large openings to the inner ship, where little light penetrates. These areas appear as depressions in the model. Keeping the camera with its upper edge at most parallel to the

lakebed would likely have minimized this problem and produced more usable hull imagery.

Shooting video allows a large number of images to be collected quickly, but the slow shutter speeds and dim lighting characteristic of video result in many blurred images. Higher-quality imagery could be obtained with a still camera and underwater strobes, though using a still camera would result in an increase in overall survey time. For management applications where in-water survey time is not a critical deciding factor, the improvement in matched points, and ultimately model resolution, could make still photography preferable to video.

Despite image blur in some scenes, the two models constructed for this study display great resolution both geometrically as well as visually. The use of a minimal amount of GCPs for scaling doesn't appear to have hindered our DEM differencing but it may be a contributing factor to the estimated error of ±0.36 m. The use of SfM in other areas of archaeology has demonstrated that with an organized network of accurately measured GCPs, it is possible to create DEMs from SfM with errors in the range of a few centimeters (Green et al., 2014). Another key factor contributing to error in our models is the limited distribution of GCPs across the scene, which leaves some regions prone to distortions due to lack of GCP constraints. In spite of our high degree of error, our models are sufficiently reliable to detect changes of >~1 m (i.e. % error of less than 36%), which is acceptable for a wide range of SCR management applications. Improving the method used for acquiring GCPs could significantly lessen this error.

Detected Changes

The results of the comparative analysis of the two models indicate that the *Wisconsin*, similar to many metal shipwrecks in the Great Lakes, is collapsing. While many sites remain well-preserved after years of submersion, the majority of metal wrecks have begun to collapse inward, as opposed to outward (Thomsen et al., 2014, Zant et al., 2015, Meverden et al., 2016). Patterns of inward collapse are associated with ship construction techniques that relied on stanchions along the centerline of vessels that were made of narrow steel or iron I-beams, usually measuring 0.3 m square. Iron and steel ships were lighter, stronger and longer than the wooden vessels they replaced, which allowed them to carry higher tonnages of cargo. The I-beams used in their construction, however, have been a notorious weak point in metal shipwrecks located in Lake Michigan.

Initial archaeological investigations of the *Wisconsin* in 2006, seemed to indicate that the *Wisconsin* was following a similar trend of collapsing inward. The upper sections of the *Wisconsin*'s outer hull had begun to lean inward as the central deck beams collapsed (Thomsen and Meverden, 2010). Data reports from investigations in 2015 indicate that this pattern, however, is no longer evident. A 19.8 m section of the *Wisconsin*'s starboard hull, which had been leaning inward significantly in 2006, has fallen away from the main body of the wreck, hinged at the aft end (Figure 2.7, A; Figure 2.8). A 7.0 m long section of the hull, located just forward of this large section, has continued its collapse inward, creating a vertical crack along its forward edge, at the aft edge of the forecastle deck, and causing the collapse of previously intact forecastle deck beams (Figure 2.7, E; Figure

2.12). Additionally, a section of the vessel's main railing, which had remained intact in 2006, now hangs off the port side of the hull (Figure 2.7, D; Figure 2.11).

Although there is no direct indication as to why this is occurring at this site and not others, one possible explanation is that site colonization by quagga mussels has altered the normal pattern of progressive inward collapse. During the sinking event, the *Wisconsin*'s upper deck cabins blew off due to a sudden release of air trapped within its enclosed spaces. When this occurred, the integrity of the iron deck beams was compromised, and upon the vessel's collision with the lakebed, these beams and their support stanchions, collapsed inward along the ship's centerline (Thomsen and Meverden, 2010). This trajectory of inward collapse should have continued as increasing weight from the buckled upper decks was placed on the remaining deck stanchions in the lower hold of the vessel. Numerous influencing factors may have contributed to the now outward collapse situation. These factors may include the colonization of mussels which not only adds weight to the structure, but also metal corrosion caused by increases local levels of carbonic acid through the introduction of carbon dioxide through mussel respiration (Hecky et al., 2004). Mussels also increase the overall surface roughness and, by doing so, increase drag forces caused by water currents. It is also important to consider that during late 2011, divers reported strong rip currents in the area extending to depths of 30-40 m. The combination of these factors could be contributing to the cracking of the thin iron covering the vessel's upper deck above the bustle. The bustle refers to the 0.9 m sections on either side of the ship where it was widened in 1909. Historically, this was an area noted for leaking and weaknesses in the hull, and may be further indication

of why the vessel is degrading more rapidly here than in other sections. Except for the small section of the vessel's fantail stern, the bow and the stern of the vessel have experienced very little overall change between 2006 and 2015. This is likely because these two sections retain their integrity from the original build of the vessel in 1881.

Although DEM differencing indicates these are areas of little change, the remaining intact sections of the upper decks, in the bow and the stern, show some signs of degradation as well (Figure 2.7). The most notable changes are located near the remains of the *Wisconsin*'s smokestack. The 2015 data notes a significant shift in the angle of the smokestack (which is still attached to the boilers below decks) from a slight list to starboard to a significant list forward (Figure 2.10, 5). This change is indicative of the collapse of the deck beams holding the smokestack in place. Though most of the upper deck beams were believed to be damaged during the original sinking, the visible continuation of this collapse progressively aft reveals a continued rapid degradation of the site. Similar deterioration has been noted in the vessel's bow, with the forecastle deck beams beginning to collapse progressively forward.

During the 2015 archaeological investigations, divers qualitatively noted that the bulkheads and stanchions in the lowest deck of the cargo hold are significantly buckled as well, indicating further collapse since the 2006 survey. Despite this collapse below decks, most of the measured change in the vessel between 2006 and 2015 has occurred to the vessel's upper decks, or what would have existed above the waterline when the vessel was afloat. This is likely occurring because these early iron and steel vessels were made with two different thicknesses of metal and using different sizes of plating. Built to break

through thick Lake Michigan ice to operate in year-round service, the *Wisconsin*'s lower hull plates were significantly stronger than those used on the upper decks. Below the bustle, the hull plating consists of a series of iron plates measuring significantly smaller in size than the hull plates used for the upper decks. These plates were also 0.03 to 0.06 m thicker than the upper deck hull plates as well (Thomsen and Meverden, 2010, Zant et al., 2015).

In summary, the use of SfM modelling with repeat underwater video or still photographic surveys of SCRs can greatly aid in the detection of site degradation and environmental and anthropogenic disturbances. By constructing models of the shipwreck *Wisconsin* using video surveys performed in 2006 and 2015, we have calculated spatial changes, through the method of DEM differencing, of up to ~±5 m vertically. Visual inspection of these changes reveals that the ship has shifted from a state of inward collapse in 2006, to what now appears to be outward collapse as seen by the many large hull sections falling away from the ship. Using the high-resolution orthoimages and DEMs from both time periods we have also been able to pinpoint numerous other objects on the upper deck that have undergone changes which can be associated with shifting of materials, degradation and mussel colonization.

Conclusion

The results of our study provide an example of a novel new approach to detecting and quantifying changes and degradation to SCRs through the use of diver-acquired photographic surveys and SfM model generation. The work demonstrates that, even with minimal GCPs from around a site, models can be easily co-registered to increase the

overall accuracy of the model differencing. We have shown that the combination of both the DEM and high-resolution orthomosaic allow detailed inspection of changes in a spatial and visual manner. While previous repeat surveys of SCRs rely on extensive and time-consuming observations and measurements, DEM differencing can more efficiently produce products to be used for comparison. The spatial resolution of detected changes in our survey is limited by the lack of stable, unmovable GCPs that were measured at high precision. By first establishing fixed GCPs around the SCR, model generation would be easier and less time consuming and accuracy would be improved relative to our study reported here. Future investigations using this type of method would benefit from using still photographs with powerful strobes to decrease image blur and increase image detail and quality. The knowledge gained from repeated surveys of SCR is of vital importance for monitoring and maintaining our historic sites.

Acknowledgements

We acknowledge funding from the David and Julia Uihlein Charitable Foundation and Wisconsin Coastal Management Program. We would also like to thank our volunteers on the project- John Scoles, John Janzen, Gayle Orner, and Carolyn Rock. The data and video collection in 2015 would not have been possible without them. Jordan R. Mertes acknowledges funding from Michigan Technological University and The Michigan Technological University 2016 Fall Finishing Fellowship.

References

Agarwal S, Furukawa Y, Snavely N, Simon I, Curless B, Seitz SM, Szeliski R. 2011. Building rome in a day. Communications of the ACM **54**: 105-112

Agisoft, 2014. Agisoft PhotoScan User Manual. In *Professional Edition, Version 1*. Agisoft LLC: http://www.agisoft.ru/pdf/photoscan_pro_1_0_en.pdfhttp://www.agisoft.ru/pdf/photoscan_pro_1_0_en.pdf, http://www.agisoft.ru/pdf/photoscan_pro_1_0_en.pdf

Bates CR, Lawrence M, Dean M, Robertson P. 2011. Geophysical Methods for Wreck-Site Monitoring: the Rapid Archaeological Site Surveying and Evaluation (RASSE) programme. International Journal of Nautical Archaeology **40**: 404-416

Björdal CG, Nilsson T. 2008. Reburial of shipwrecks in marine sediments: a long-term study on wood degradation. Journal of Archaeological Science **35**: 862-872

Bolch T, Pieczonka T, Benn D. 2011. Multi-decadal mass loss of glaciers in the Everest area (Nepal Himalaya) derived from stereo imagery. The Cryosphere **5**: 349-358. DOI: 10.5194/tc-5-349-2011

Canada P, 2005. Guidelines for the Management of Archaeological Resources. Parks Canada Agency: Ottowa, Canadafile:///C:/Users/Jordan%20Mertes/Downloads/archguide_e.pdf

De Rose RC, Basher LR. 2011. Measurement of river bank and cliff erosion from sequential LIDAR and historical aerial photography. Geomorphology **126**: 132-147

Etzelmüller B. 2000. On the Quantification of Surface Changes using Grid-based Digital Elevation Models (DEMs). Transactions in GIS **4**: 129-143

Foecke T, Ma L, Russell MA, Conlin DL, Murphy LE. 2010. Investigating archaeological site formation processes on the battleship USS Arizona using finite element analysis. Journal of Archaeological Science **37**: 1090-1101

Franke J. 1999. Applying Photomodeler in maritime archaeology: A photogrammetric survey of the J3 submarine wreck. Western Australia Maritime Museum, Department of Maritime Archaeology

Gibbs A, Nolan M, Richmond B, 2015. Evaluating changes to arctic coastal bluffs using repeat aerial photography and structure-from-motion elevation models. In *Proceedings from 2015 Coastal Sediments Conference, San Diego, CA, CD-ROM (doi: 10.1142/9789814689977_0080)*,

Green J, Matthews S, Turanli T. 2002. Underwater archaeological surveying using PhotoModeler, VirtualMapper: different applications for different problems. International Journal of Nautical Archaeology **31**: 283-292

Green S, Bevan A, Shapland M. 2014. A Comparative Assessment of Structure from Motion Methods for Archaeological Research. Journal of Archaeological Science **46**: 173-181. DOI: 10.1016/j.jas.2014.02.030

Gregory D, Jensen P, Strætkvern K. 2012. Conservation and in situ preservation of wooden shipwrecks from marine environments. Journal of Cultural Heritage **13**: S139-S148

Hecky R, Smith RE, Barton D, Guildford S, Taylor W, Charlton M, Howell T. 2004. The nearshore phosphorus shunt: a consequence of ecosystem engineering by dreissenids in the Laurentian Great Lakes. Canadian Journal of Fisheries and Aquatic Sciences **61**: 1285-1293. DOI: 10.1139/f04-065

Henderson J, Pizarro O, Johnson-Roberson M, Mahon I. 2013. Mapping Submerged Archaeological Sites using Stereo-Vision Photogrammetry. International Journal of Nautical Archaeology **42**: 243-256

Horlings RL. 2011. Of his bones are coral made: submerged cultural resources, site formation processes, and multiple scales of interpretation in coastal Ghana.

Kääb A, Berthier E, Nuth C, Gardelle J, Arnaud Y. 2012. Contrasting patterns of early twenty-first-century glacier mass change in the Himalayas. Nature **488**: 495-498. DOI: 10.1038/nature11324

Lane SN, Westaway RM, Murray Hicks D. 2003. Estimation of erosion and deposition volumes in a large, gravel-bed, braided river using synoptic remote sensing. Earth Surface Processes and Landforms **28**: 249-271

Ludvigsen M, Eustice R, Singh H, 2006. Photogrammetric models for marine archaeology. In *OCEANS 2006*; 1-6. DOI: 10.1109/OCEANS.2006.306915

McCarthy J. 2014. Multi-image photogrammetry as a practical tool for cultural heritage survey and community engagement. Journal of Archaeological Science **43**: 175-185

Mertes J, Thomsen T, Gulley J. 2014. Evaluation of Structure from Motion Software to Create 3D Models of Late Nineteenth Century Great Lakes Shipwrecks Using Archived Diver-Acquired Video Surveys. Journal of Maritime Archaeology **9**: 173-189. DOI: 10.1007/s11457-014-9132-x

Meverden KN, Thomsen TL, Zant CN, 2016. Senator Shipwreck (steam screw). In *In National register of historic places nomination form. Manuscript on file.* Wisconsin Historical Society: Division of Historic Preservation and Public History: Madison, Wisconsin

Morris DP, Lima J. 1996. Channel Islands National Park and Channel Islands National Marine Sanctuary: Submerged Cultural Resources Assessment.

Murphy LE. 1993. Dry Tortugas National Park: submerged cultural resources assessment. US Department of the Interior, National Park Service, Submerged Cultural Resource Unit

Murphy LE. 1998. HL Hunley site assessment. Submerged Cultural Resources Unit, Intermountain Region, National Park Service

Nuth C, Moholdt G, Kohler J, Hagen JO, Kääb A. 2010. Svalbard glacier elevation changes and contribution to sea level rise. Journal of Geophysical Research: Earth Surface **115**:

Obu J, Lantuit H, Grosse G, Günther F, Sachs T, Helm V, Fritz M. 2016. Coastal erosion and mass wasting along the Canadian Beaufort Sea based on annual airborne LiDAR elevation data. Geomorphology:

Palma P. 2005. Monitoring of shipwreck sites. International Journal of Nautical Archaeology **34**: 323-331

Rippin D, Willis I, Arnold N, Hodson A, Moore J, Kohler J, Björnsson H. 2003. Changes in geometry and subglacial drainage of Midre Lovénbreen, Svalbard, determined from digital elevation models. Earth Surface Processes and Landforms **28**: 273-298
Russell MA. 2004. Comet: submerged cultural resources site report, Channel Islands National Park. DIANE Publishing
Russell MA, Murphy LE. 2013. Balancing Historic Preservation, Science, and the Environment in Underwater Cultural Heritage Site Management: Long-Term Management Strategies for the Sunken Battleship USS Arizona. Conservation and Management of Archaeological Sites:
Thompson S, Benn DI, Mertes J, Luckman A. 2016. Stagnation and mass loss on a Himalayan debris-covered glacier: processes, patterns and rates. Journal of Glaciology: 1-19. DOI: 10.1017/jog.2016.37
Thomsen T, Meverden K, 2010. Wisconsin Shipwreck (steam screw). In *National register of historic places nomination form. Manuscript on file.* Wisconsin Historical Society: Division of Historic Preservation and Public History: Madison, Wisconsin
Thomsen T, Reckner P, Stout M, 2014. Lakeland Shipwreck (steam screw). In *In National register of historic places nomination form. Manuscript on file.* Wisconsin Historical Society: Division of Historic Preservation and Public History: Madison, Wisconsin
Walder JS, Schilling SP, Vallance JW, LaHusen RG. 2004. Effects of lava-dome growth on the Crater Glacier of Mount St. Helens, Washington. A volcano rekindled: the renewed eruption of Mount St. Helens **2006**: 257-276
Ward IA, Larcombe P, Veth P. 1999. A new process-based model for wreck site formation. Journal of Archaeological Science **26**: 561-570
Wheeler A. 2002. Environmental controls on shipwreck preservation: the Irish context. Journal of Archaeological Science **29**: 1149-1159
Williams R, Brasington J, Vericat D, Hicks M, Labrosse F, Neal M. 2011. Chapter twenty-monitoring braided River change using terrestrial laser scanning and optical bathymetric mapping. Developments in Earth Surface Processes **15**: 507-532
Zant CN, Thomsen TL, Reckner P, Stout M, 2015. Milwaukee Shipwreck (steam screw). In *In National register of historic places nomination form. Manuscript on file.* Wisconsin Historical Society: Division of Historic Preservation and Public History: Madison, Wisconsin

Chapter 3. Using Structure from Motion to create DEMs and Orthoimagery from Historical Terrestrial and Oblique Aerial Imagery[3]

Abstract

Increased resolution and availability of remote sensing products, and advancements in small-scale aerial drone systems, allows observations of glacial changes at unprecedented levels of detail. Software developments, such as Structure from Motion (SfM), now allow users an easy and efficient method to generate 3-D models and orthoimages from aerial or terrestrial datasets. While these advancements show promise for current and future glacier monitoring, many regions still suffer a lack of observations from earlier time periods. We report on the use of SfM to extract spatial information from various historic imagery sources. We focus on three geographic regions, the European Alps, High-Arctic Norway and the Nepal Himalaya. We used terrestrial field photos from 1896, high-oblique aerial photos from 1936 and aerial handheld photos from 1978 to generate DEMs and orthophotos of the Rhone glacier, Brøggerhalvøya and the lower Khumbu glacier, respectively. Our analysis shows that applying SfM to historic imagery can generate high quality models using only ground control points. Estimated camera model/orientation information, exported from the SfM software, matches very well with the limited information from each data set. Using these data, we calculated mean ground sampling distances across each site which demonstrates the high potential resolution of resulting models. Vertical errors for our models are ±5.4 m, ±5.2 m and ±3.3 m. Differencing shows similar patterns of thinning at lower Rhone and Brøggerhalvøya glaciers, which

[3] The material in this chapter has been submitted for review to the journal Earth Surface Processes and Landforms October 21, 2016. Reviews have been received as of February 20th, 2017, and are currently being implemented for resubmission.

have mean surface lowering rates of 0.31 m a-1 to 0.86 m a-1, respectively. On these clean ice glaciers surface lowering is highest in the terminus region and more even and decreasing up glacier. In contrast to these glaciers, uneven topography, exposed ice-cliffs and debris cover on the Khumbu glacier create a highly variable spatial distribution of surface lowering. The mean lowering rate for the Khumbu study area was found to be 0.54±0.9 m a-1.

Introduction

Observations from an increasing number of glacier monitoring programs have quantified the sensitivity of glaciers to regional and global climate changes that have occurred over the last several decades (Silverio and Jaquet, 2005, Paul et al., 2007, Bolch et al., 2011, Kamp et al., 2011, Diolaiuti et al., 2012, Braithwaite et al., 2013). Many locations, however, lack any glacier monitoring programs or have only short periods of data. Understanding magnitudes of changes in modern glacier mass balance would be improved if these changes could be placed in historical context. Such improvements could aid in improved forecasting of future glacial conditions and associated implications for water resources (Immerzeel et al., 2010, Thorsteinsson et al., 2013, Unger-Shayesteh et al., 2013, Soruco et al., 2015) and potential geo-hazards (Bolch et al., 2011, López-Moreno et al., 2014) by gaining more insight into past changes.

Current technology allows scientists to monitor glaciers at spatio-temporal scales that were unthinkable 20 years ago. Just over 10 years ago, a DEM of 10m resolution was considered “high-resolution” (Gruen and Murai, 2002). It is now possible to get stereo satellite images of glaciated regions that that can yield products, such as digital elevation

models (DEMs) and orthorectified imagery, at resolutions of < 0.5 m (e.g. GeoEye, Worldview, Pleiades). Light detection and ranging (LiDAR) is a widely used technology in cryospheric sciences, both terrestrially and aerially, and has the capability of producing models of centimeter resolution and accuracy (Bhardwaj et al., 2016a). Recent advances in unmanned aerial vehicles (UAVs) and computer vision software such as Structure from Motion (SfM) and Multi-View Stereo (MVS) now allow researchers to extract 3D information from their own remotely-sensed data at high spatial and temporal resolution (Bhardwaj et al., 2016b). While current high-resolution satellite data, aerial and terrestrial LiDAR scans and UAV surveys can help monitor present and future glacial changes in unprecedented detail, historical oblique images remain a largely untapped resource of glacier mass balance data.

Numerous studies have used older satellite and vertical aerial photos for studying glacier changes by either orthorectifying the images over current DEMs (e.g. Surazakov et al., 2007, Bhambri et al., 2011, Wang et al., 2016), or by producing actual DEMs from the imagery itself (Bolch et al., 2011). Bjork, et al. (2012) recently combined sequences of historic aerial images from Greenland, dating as far back as the 1930s, to visualize long-term changes to glaciers in the southeast. Much of the earlier imagery was shot at high-oblique angles for cartographic purposes, and was used by Bjork et al. primarily to determine the location of previous glacier margins through orthorectification; the earliest DEM was based on vertical aerials photographed in the early 1980s. While not possible until a few years ago, recent advances in SfM now allow DEMs to be created directly

from the historical imagery without the need to orthorectify historic aerial imagery over current DEMs, and with minimal need for *a priori* camera information.

Using SfM+MVS to extract geometric information from imagery works by matching features (e.g. pixels, pixel groups, edges) of the same subject across images that were taken from different positions or perspectives. Then, through perspective projection, SfM+MVS estimates the positions, attitudes and focal lengths of the individual images (i.e. SfM) (Agarwal et al., 2011). Following sparse 3-D point cloud generation, estimation of internal orientation (IO) (e.g. focal length, radial distortion) and a relative external orientation (EO) (i.e. X, Y, Z, roll, pitch, yaw), MVS algorithms generate a dense point cloud by extracting depth information from all pixels found in multiple images (Agarwal et al., 2011). As a result, SfM+MVS (hereafter referred to as SfM) allows generation of 3-D models of objects without having any IO or EO information. 3-D models created without IO or EO information are built in an arbitrary space but real-world coordinate systems can be assigned with the aid of current orthoimagery and DEMs by matching arbitrary points in the model with their corresponding real-world position. This information is then used during sparse point cloud optimization, during which the accuracy of the model, and the estimated camera positions and parameters can be improved (Agisoft, 2014). The result of such a process is that one can create a DEM and orthoimages using easily acquired imagery and identifiable ground control data. When IO and EO information are known before beginning SfM, they can be used to speed up processing and create a georeferenced model without the need to manually assign real-world coordinates (Agisoft, 2014).

In this study, we present the results of using the SfM technique to extract geometric information and create DEMs from freely available, archival glacial imagery. Creating these historical DEMs allows us to document changes in glacier surfaces as far back as the late 19th century. We focus on three distinct geographic regions and glacial types, the European Alps clean ice glacier, High-Arctic Norway clean ice glaciers and the Nepal Himalayas heavily debris-covered glacier, from 1896, 1936 and 1978 respectively. These specific cases involve different image types and compare resultant models and glacial changes on a variety of glaciers. In addition, we demonstrate how this process can be performed without *a priori* information about the IO and EO of the imagery, and how with precise enough GCPs, the estimated EO information becomes close to the true values.

Study Sites

Our study sites cover a range of glaciated environments from alpine to arctic and Himalayan. Within these regions, we selected glaciers that have historical images and that have also been the focus of previous glaciological investigations.

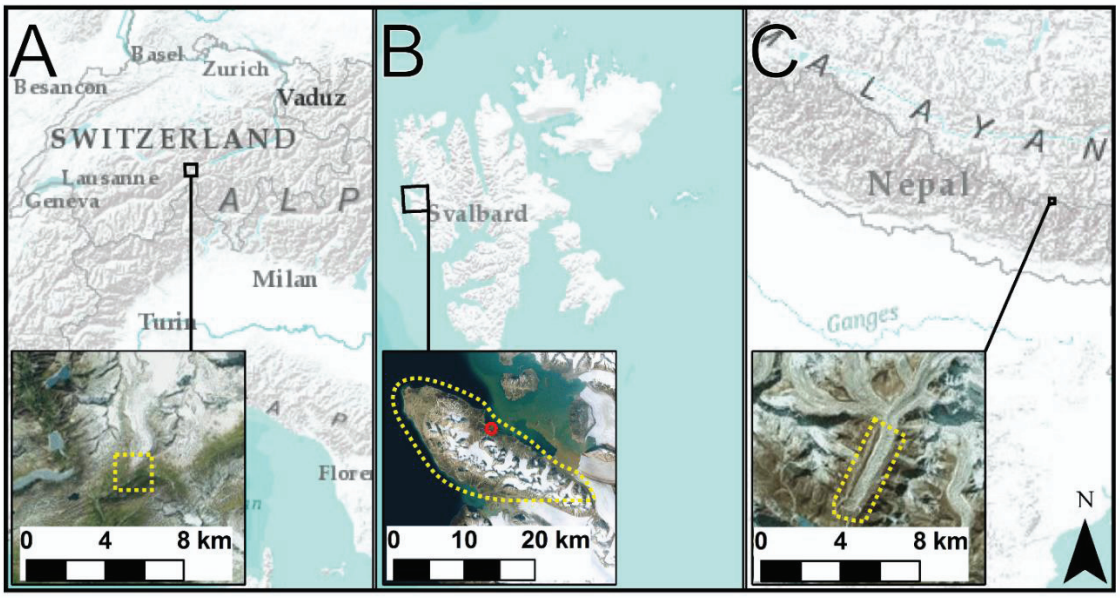

Figure 3.1: Overview of three study sites, A) Rhone glacier, Switzerland, B) Brøggerhaløya (with Ny Ålesund circled in red), Svalbard, C) Khumbu glacier, Nepal.

Rhone glacier, Switzerland

The Rhone glacier (46°36'N, 8°23'E) is located in the central Swiss Alps (Figure 3.1, A) and is the source of the Rhone river, which flows through Lake Geneva and south to the Mediterranean Sea. The glacier has some of the longest time series of observations of any glacier in the world, with length measurements dating back to 1609 and mass balance measurements dating back to 1884 (Wallinga and Wal, 1998). We selected this site because repeat terrestrial photographic surveys began during the late 19th century (Mercanton et al., 1916). In addition, the glacier's rapid retreat from the lower valley to its current position is well documented in postcards, photographs and scientific articles. The abundance of photographic, cartographic and glaciological data on the Rhone glacier have made this glacier the focus of numerous glacier-climate modelling studies, as there

is plenty data available to verify model results (Roderik and Van De Wal, 1998, Sugiyama et al., 2007, Jouvet et al., 2009). For this study, we focus on the 1.1 km^2 area in the lower valley from where the glacier terminated in 1896, up to the lip of the upper hanging valley (Figure 3.1, A Yellow Box).

Ny Ålesund, Svalbard

The Svalbard Archipelago is located north of mainland Norway at ~76-80°N and ~10-30°E (Figure 3.1, B). Nearly 60% of the total area of Svalbard is glaciated (Hagen et al., 2003). We selected Brøggerhalvøya (~190 km^2), which is located around the research village of Ny Ålesund, on the northwestern coast of Spitsbergen (78°56′ N, 11°53′ E) (Figure 3.1, B Yellow Box), as our study area because previous attempts at extracting surface information have been performed over this region. Nuth et al. (2007) interpolated DEMs from topographic maps with 50 m contour intervals, the maps were originally derived in part from the imagery used in this study. The area has a central mountain ridge running in a NW-SE direction with ~25 small cirque glaciers, some of which have been the focus of numerous scientific studies.

Khumbu Glacier, Nepal

The Khumbu glacier is located in the similarly named Khumbu region of the Mahālangūr Himāl, northeast Nepal (Figure 3.1, C) (Carter, 1985). The glacier accumulation zones are located in the upper reaches of mountain peaks, including Chumbu to the west, Pumori to the north and Lhotse, Nupste and Mt. Everest to the north and east. From the south face of Mt. Everest, the glacier flows a distance of 16 km to the terminus. Our area of interest is the lower 10 km of the glacier, located just down glacier from the

confluence of the two main tributaries, ~5000 m a.s.l. (Figure 3.1, C Yellow Box). The area has been chosen based on the type of imagery (i.e. handheld cameras) and the importance of understanding the long-term evolution of debris-covered glacier surfaces and patterns of downwasting. The glacier terminus is at an elevation of 4900 m a.s.l. (Nakawo et al., 1999). The flow direction of this section of the glacier runs in a NE-SW direction at 207° and the lowest 4 km of the snout are now stagnant (Quincey et al., 2009).

Methods

Imagery

We obtained 3 images of the Rhone glacier (Figure 3.2) from the Swiss Federal Institute of Technology (ETH) Library "e-pics" imagery archive (ETH-Bibliothek, 2016). The images are terrestrial photographs taken 30 August, 1896. They are located in the collection of imagery taken by the Glaziologische Kommission der SANW. None of the images were attributed to any specific photographer, but they have similar compositions as repeat photographs of the Rhone glacier taken by Paul-Louis Mercanton during the late 19th century through to the early 20th century and were taken on similar 9x12 cm film plates (Mercanton et al., 1916). The series contained numerous photographs, but only 4 captured the lower glacier tongue. Of these four, view angles only allowed us to use three images for model recreation. We were unable to find any information pertaining to camera type, IO or EO.

We obtained 25 images of the Ny Ålesund field site (Figure 3.2) from the Toposvalbard database (http://toposvalbard.npolar.no), which is managed by the Norwegian Polar

Institute. Images on Toposvalbard can be browsed in a GIS environment, in which each image is placed in its approximate geographic position with a marker arrow indicating the line of sight. These aerial high-oblique images were taken from roughly 3-3500 m a.s.l. during the summer of 1936 using a Zeiss 18 x 18 cm aerial camera with a focal length of 210 mm (Debenham, 1938). The images were taken in a roughly south to southwest direction from above Kongsfjord, on the northern shore of the peninsula. Detailed IO and EO data have not been determined for these images.

We obtained 42 images of the Nepal field site (Figure 3.2) from the Japan Agency for Marine-Earth Science and Technology's Cryosphere Data Archive Partnership (CrDAP) Observational Research Database. These images are part of the 11 December 1978 aerial photo reconnaissance, which was conducted by the Japanese Glaciological Expedition in Nepal (GEN) to support large-scale glacial observations throughout the Nepal Himalaya (Yabuki, 2011). The photos were taken with handheld 35 mm film based cameras from a chartered low flying Pilatus Turbo Porter airplane, at angles from high-oblique to near-nadir (Yabuki and GEN-(Nagoya University, 2012). Data pertaining to detailed IO and EO of the cameras used to capture these images is also unknown.

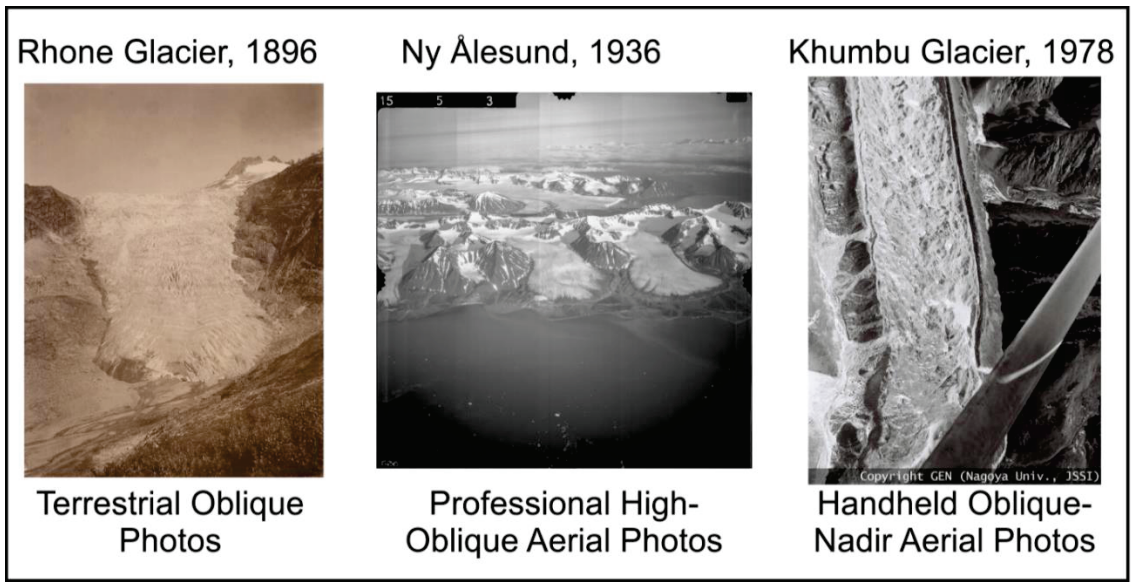

Figure 3.2: Examples of imagery used for SfM model generation including 1896 terrestrial imagery from the Rhone glacier (Data source: ETH-Bibliothek (2016), high-oblique aerial photographs done during the 1936 Svalbard survey (Data source: http://toposvalbard.npolar.no, 'detail of S36-1553', © Norsk Polarinstitutt,) and handheld mixed images from 1978 over the lower Khumbu glacier (Data source: CrDAP, Yabuki (2011)) .

Image corrections

We adjusted contrast and exposure of all images in Adobe Photoshop Lightroom™ 6.6.1. This process was subjective and performed manually on the different sets of images to improve clarity in the areas of interest.

We made no additional adjustments to the Switzerland imagery as they appear to be slightly different dimensions (3520x2537, 3462x2635 & 3425x2632 pixels) and have no borders or fiducial markings to align.

Images from the Svalbard survey were first corrected for alignment issues caused during digitizing. We noted alignment issues when we observed that images were not exactly the same dimensions. All images were opened in a common photo editing suite, placed into individual layers and one by one were rotated and scaled slightly to align the fiducial marks around the image borders. Once this was complete, all images were cropped down to the nearest square dimension of 6370x6370 pixels.

The images from the Nepal survey were digitized to the same dimensions therefore no post resizing, alignment or cropping was performed. Images have dimensions of 2137x1535 pixels. Image watermarks pose no issue as these areas can be masked out during processing.

Reference DEMs and Orthoimages

We relied on recent high-resolution DEMs and orthoimages to identify stable ground control points (GCPs), such as boulders or mountain peaks, for georeferencing the final models. The addition of GCPs also helps to improve the calculation of the IO and EO information.

For the Rhone glacier, subsets of a 2010 digital terrain model (DTM) and a very-high resolution orthoimage were provided by the Swiss Federal Research Institute WSL. The color infrared (CIR) orthoimage has a resolution of 0.5 m. The DTM has a resolution of 1 m with a RMSE of 0.81 m (Ginzler and Hobi, 2015).

The DEM and orthoimagery for Svalbard is freely available through the Norwegian Polar Institute's (NPI) Geodata portal (geodata.npolar.no). The DEM of the area,

NP_S0_DTM5_2010_13828_33 is a 5 m resolution DEM generated from high-resolution aerial imagery taken during a 2010 campaign. It was cropped down to include our area of interest which is roughly within the yellow dashed border in Figure 1. The standard deviation of the model is between 2-5 m (NPI, 2014).

The DEM for the Khumbu glacier was generated from very-high resolution Pleiades satellite imagery acquired on 7th October 2015. The 2015 model generation was done using only the supplied rational polynomial coefficients without GCPs. This is not an issue because we only wish to co-register the two models and are not looking for real world positioning accuracy. The resulting DEM and orthoimage have resolutions of 1 and 0.5 m respectively.

Model Generation

We used Agisoft Photoscan™ SfM software package version 1.1.6 build 2038- 1.2.5 build 22735 (64 bit) to create our DEMs. The processing was performed on a custom-built laptop running an Intel© Core™ i7-6700 4.00 GHz with eight cores and 64Gb of memory. The computer GPU is a NVIDIA® GeForce® GTX 980M with 8.0GB DDR5 Video RAM.

For each specific study site, images are first imported into Photoscan and areas that are not modelled are masked out using the mask tool. For the Rhone glacier imagery, masked areas include foreground as well as the horizon and mountains beyond the glacier area. For images from the Ny Ålesund survey, these areas mainly include features behind the first mountain ridge-line parallel to the flight path (i.e. limited line of sight areas) and the

ocean shore line and sky. For the Khumbu glacier imagery, these masked areas include the horizon, the watermarked edge of the photos as well as parts of the airplane that are present in some images.

Initial alignment was done at the setting of 'high' for the Ny Ålesund imagery and 'highest' for the Rhone and Khumbu imagery. No previously known camera information was used for our model generation (e.g. focal length) however the resulting estimated IO/EO data allow us to check estimate accuracy. The sparse point clouds generated for the three sites have 11662 (Rhone), 58742 (Ny Ålesund) and 148178 (Khumbu) points prior to filtering. Sparse points were filtered using the *Gradual Filter* function and points with reprojection errors of greater than ~0.5 were removed, along with points that appear distant or obviously erroneous. This step is recommended in the Agisoft manual to help improve the accuracy of the following optimization steps and bundle adjustments by removing points with larger potential error (Agisoft, 2014). The resulting sparse point clouds contained 10370 (Rhone), 33657 (Ny Ålesund) and 48868 (Khumbu) points.

GCPs used to georeference point clouds were features identified in both the historic and current imagery that are unlikely to have changed positioning (e.g. large boulders on apparently stable terrain). Adding GCPs after initial alignment is substantially faster than prior to alignment because the software can automatically determine the location of the GCP in each image used to construct the model after the user places the first marker. The software then populates the marker throughout the image data set. Following the placement of the first marker, we then filtered the photos to those with the marker and then adjusted the locations slightly to improve the placement accuracy. After each marker

was positioned correctly, we entered the X, Y, Z data extracted from the current DEM and performed a bundle adjustment. We developed a method to speed up the identification of potential GCPs by placing perhaps 3-4 GCPs, spread out over the AOI, optimizing, then generating a dense cloud, a DEM and an orthophoto. It is then possible to drape the roughly aligned orthophoto over the current orthophoto and, using for example the swipe feature in ESRI's ArcMap, easily identify objects which have undergone no visible change. For Rhone glacier, Ny Ålesund and Khumbu glacier, 14, 27 and 32 GCPs were identified respectively.

After we identified all GCPs and performed model optimizations, we generated dense point clouds at high settings with moderate to aggressive point filtering. The dense point clouds for each site contained 1418606 (Rhone), 20053599 (Ny Ålesund) and 12563679 (Khumbu) points. Each dense cloud was then edited and points far beyond our areas of interest were removed along with obvious erroneous points.

Meshes were generated for the Rhone glacier and Ny Ålesund sites and smoothed using the Photoscan mesh tool, with a value of 3 for "passes". This helped to smooth areas where dense point removal was difficult due to topography. For both the Rhone and Ny Ålesund sites, the resulting mesh was then used for DEM construction. For the Khumbu glacier, however, the dense point cloud was easily editable and showed no signs of extreme noise, therefore we use the dense point cloud as the source for the final DEM. Generation of DEM with the setting "interpolated" enabled resulted in areas of over interpolation occurring around the model perimeter and in areas of poor visibility (e.g.

behind ridges). After final DEMs were generated we produced the resulting orthoimagery using the DEMs as the underlying surface.

Calculated Focal Lengths and GSD

Upon completion of our DEM and orthoimagery generation it is possible to use the estimated IO and EO parameters, in combination with previous knowledge of image size and sensor size (i.e. film size), to calculate image focal lengths and fields of view for comparison. This information also aids us in determining potential maximum and minimum ground sampling distance (GSD).

To calculate the estimated focal length of the images in mm we take the estimated focal lengths in pixels, fp, divided by the corresponding pixel dimension of the image (i.e. width or height), p_w, and multiply by the actual sensor dimension (e.g. 35 mm film sensor has a 0.036 m width), s_w.

$$f_l = \frac{f_p}{p_w} s_w$$

Photoscan's camera data export gives two focal lengths, one for the horizontal dimension and one for the vertical. We have used the mean of the calculated focal lengths for each dimension. To calculate the horizontal and vertical fields of view we use the formulae,

$$fov_H = 2\tan^{-1}\left(0.5\frac{s_w}{f_l}\right) \qquad fov_V = 2\tan^{-1}\left(0.5\frac{s_h}{f_l}\right)$$

Where fov_H, fov_V, s_w and s_h are the horizontal and vertical fields of view and the sensor width and height, respectively. We used sensor widths and heights of 0.12 x 0.09

m, 0.18 x 0.18 m and 0.036 x 0.024 m for the Rhone, Ny Ålesund and Khumbu imagery, respectively.

Using the camera EO and the calculated fields of view we then calculated the viewshed of each camera. This is similar to the viewshed tool in GIS software packages such as ESRI ArcMap, however we have added a calculation of the distance to each visible DEM pixel from the camera location as well. These distances were then used to calculate an estimated mean GSD map for each study site.

Results

DEM Error Analysis

The details of the resulting DEM and orthoimages generated through a SfM process are given in Table 3.1. The final resolutions of the DEMs for the Rhone, Ny Ålesund and the Khumbu glacier are 1.00, 2.30 and 1.44 m respectively. From the used GCPs for each site, the 3-D RMSE are 7.24, 13.40 and 8.46 m however the RMSE in the Z direction are 3.11, 4.40 and 2.02 m respectively.

Table 3.1: Resulting resolutions and errors for orthoimages and DEM produced using Photoscan.

	Rhone	Ny Ålesund	Khumbu
DEM Resolution (m)	1	2.3	1.44
Ortho Resolution (m)	0.2	1	0.5
Photoscan GCP 3D RMSE	7.24	13.4	8.46
Photoscan GCP Z RMSE	3.11	4.4	2.02
ΔZ RMSE (m)	2.62	0.57	1.69
ΔZ σ (including extreme outliers) (±m)	9.5	18.1	3.5
ΔZ σ (excluding extreme outliers) (±m)	5.4	5.2	3.3

After differencing each DEM with the more recent DEMs, we masked out the glacier areas and calculated the RMSE of the off-glacier differences (ΔZ), which we assume should have a value of zero if the stable landscape has undergone no change. The ΔZ RMSE for the Rhone area is 2.62 m while the areas around Ny Ålesund and Khumbu are 0.57 and 1.69 m respectively.

To determine the best possible standard deviation to use for our DEM differencing we analyzed the spread of off-glacier ΔZ values for each site. The results of this analysis are shown in Table 2 and Figure 3. The maximum and minimum off-glacier ΔZ for the Rhone glacier, Ny Ålesund and the Khumbu glacier are 46.4, 136.2 and 32.9 m (max) and -78.1, -355.3 and -40.1 m (min), respectively. While these values seem quite large, the interquartile range of off-glacier ΔZ (i.e. minimum and maximum of the middle 50% of the data) for each site is between -4.4 – 1.3 m (Rhone), -3.0 – 2.7 m (Ny Ålesund) and -1.0 – 3.0 m (Khumbu) (Table 3.2).

Table 3.2: Summary of off glacier statistics for each site showing distribution of values, boundaries of outliers and percentages of total points.

	Off Glacier Differences (m)				Count (#)			Percent of Total		
	Rhone	Ny Alesund	Khumbu		Rhone	Ny Alesund	Khumbu	Rhone	Ny Alesund	Khumbu
Max	46.4	136.2	33.0	**Upper Extreme Outliers**	3114	93309	2622	0.5	3.1	0.3
Upper Extreme Outlier Limit	18.3	19.8	15.2	**Upper Outliers**	13983	78196	13555	2.2	2.6	1.5
Upper Outlier Limit	9.8	11.2	9.1	**Upper Adjacent**	141664	582281	215625	22.3	19.3	23.3
Q3	1.3	2.7	3.0		0	0	0	0.0	0.0	0.0
Q2/Median	-1.6	0.1	0.8	**IQR**	317532	1507580	463736	50.0	50.0	50.0
Q1	-4.4	-3.0	-1.0		0	0	0	0.0	0.0	0.0
Lower Outlier Limit	-12.9	-11.5	-7.1	**Lower Adjacent**	119377	609200	220179	18.8	20.2	23.7
Lower Extreme Outlier Limit	-21.4	-20.1	-13.2	**Lower Outliers**	18764	77832	9935	3.0	2.6	1.0
				Lower Extreme Outliers	20617	66756	1673	3.2	2.2	0.2
Min	-78.1	-355.3	-47.5	**Total**	635051	3015154	432820	100.0	100.0	100.0

Outliers in each set of off-glacier ΔZ are given as values within 1.5σ to 3σ away from the interquartile boundaries. Extreme outliers on the other hand are classified as being greater than 3σ away from the interquartile boundaries (Table 3.2) and make up a very small percentage of the overall off-glacier ΔZ (Figure 3.3). For the Rhone site the outliers make up 8.9% of the total sampled off-glacier ΔZ. For the Ny Ålesund and Khumbu sites the outliers make up 10.5% and 3.0% respectively (Figure 3.3).

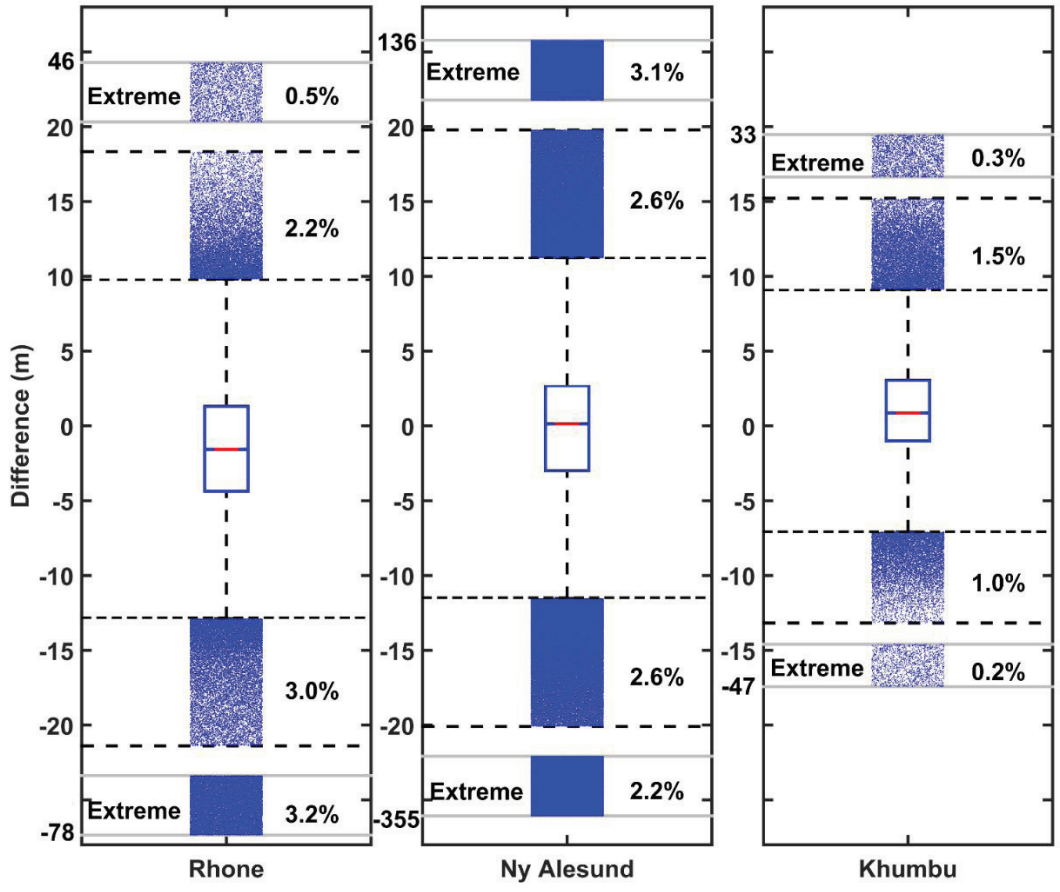

Figure 3.3: Box and whisker plots of the off-glacier elevation differences. This shows the percentage of data considered extreme outliers and normal outliers, with the inner box upper and lower bounds being the limits the 25-75% of data. The center line represents the data median.

To visually inspect the spatial distribution of both normal and extreme outliers we removed all non-outlier data from the set and draped a raster layer over the DEMs in a GIS environment. We displayed outliers as grey and extreme outliers as black (Figures 3.4, 3.5 and 3.6, C). These areas show up in either zones of poor photographic coverage or along the edges of our study areas and can be identified as over interpolation artifacts from Photoscan. Taking this into consideration, we removed all the data considered extreme outliers and recalculated our off-glacier ΔZ statistics. Our original $\Delta Z\sigma$, including extreme outliers, were ±9.5 m, 18.1 m and 3.5 m, and excluding these outliers ±5.4 m, 5.2 m and 3.3 m for the Rhone glacier, Ny Ålesund and the Khumbu Glacier respectively (Table 3.1).

Final Products

Our resulting orthoimages, DEMs and differences are shown in Figures 3.4, 3.5 and 3.6. The resolution of the orthoimagery, as stated by Photoscan during export, are 0.2 m,1.0 m and 0.5 m for the Rhone glacier, Ny Ålesund and the Khumbu glacier respectively. The Ny Ålesund orthoimage does have some gaps and blurred areas that occur beyond the mountain ridge running parallel to the flight direction (i.e. west to east). The Rhone glacier image also shows some blurred areas, which we can attribute to areas with poor coverage and a lower number of final points. These areas of sparse coverage cause excessive stretching of the orthoimagery during final mosaicking. The distribution of GCPs is shown in Figures 3.4, 3.5 and 3.6 as yellow markers overlain on the orthoimages.

The hillshaded DEMs (Figures 3.4, 3.5 and 3.6, B) show a high amount of detail and do not appear to contain any extremely erroneous points in the areas of interest. The upper edge and lower right corner of the Rhone DEM (Figure 3.4, B), as well as the southern side of the Ny Ålesund (Figure 3.5, B) and Khumbu (Figure 3.6, B) DEMs, contain the areas previously mentioned as zones of poor coverage and over interpolation. The Ny Ålesund DEM suffers from numerous areas of over interpolation and gaps due to poor reconstruction, or of little to no visibility being interpolated across. We were able to easily identify the largest of these areas in the hillshaded DEM and removed them prior to differencing.

The differenced DEMs (Figures 3.4, 3.5 and 3.6, C) show very distinct patterns of glacier mass loss for each of our study sites. The color maps for each have been adjusted to show areas within the calculated standard deviation (e.g. ±5.4, 5.2 and 3.3 m) as well as the remaining areas. This makes it easier to see that in the off-glacier regions of each site our differencing appears to be within these errors. The limit of -15 m change was chosen since in some areas we have deposition as opposed to lowering, a process that we mainly observed on the Khumbu glacier (Figure 3.6, C). For each difference map, the regions colored grey or black represent the outlier and extreme outlier areas respectively. For the Rhone glacier, these areas occur along corners of the DEM, whereas in Ny Ålesund many of these areas occur on the southern edge and on slopes that were shaded or occurred in areas of poor visibility. For the Khumbu glacier, these areas are located at the end of the terminus and are most likely due to shading on hillsides or areas where the surface

material is over exposed and extremely bright, which again would lead to poor contrast and texture.

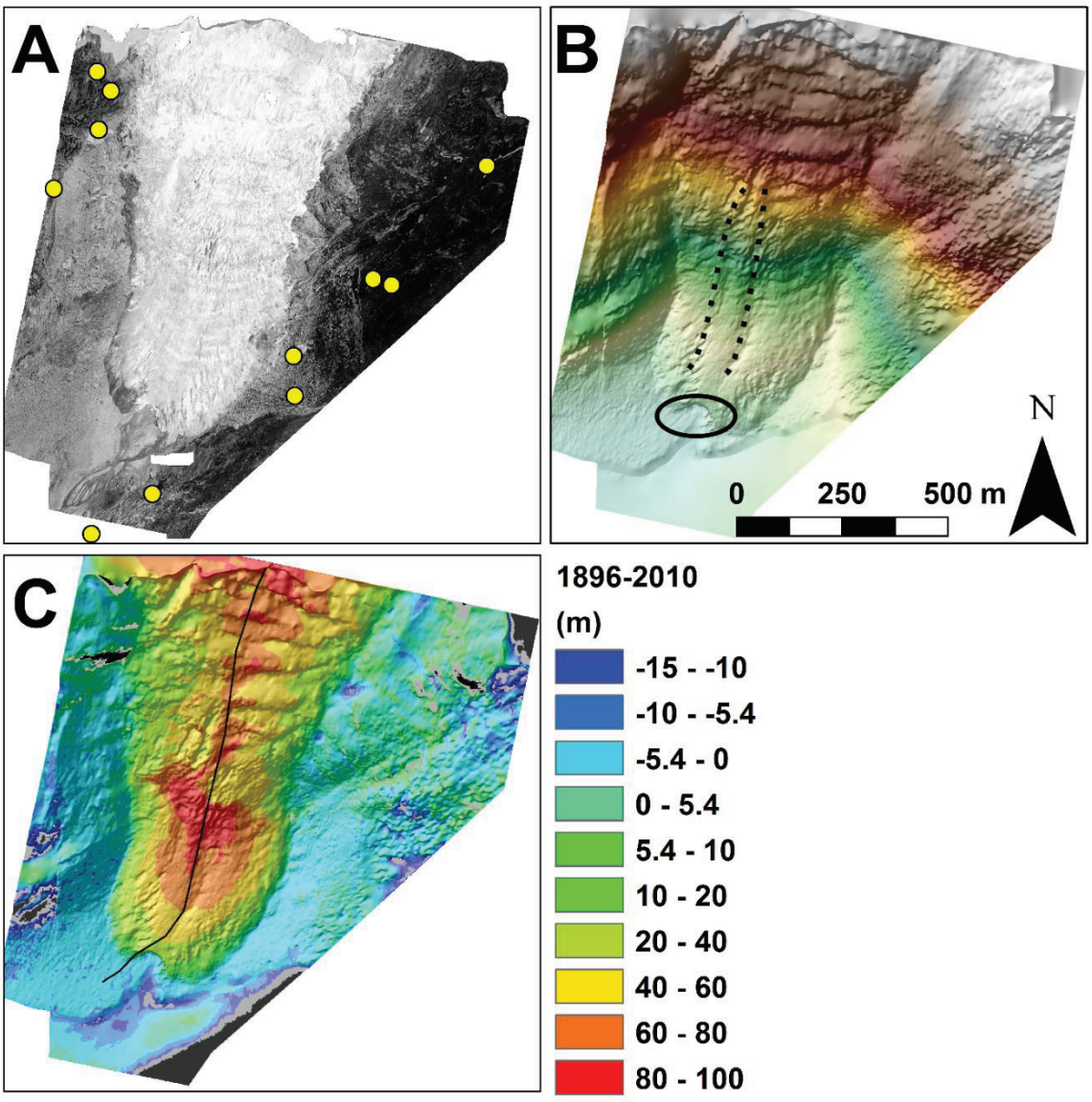

Figure 3.4: (A) Rhone glacier orthoimage, (B) 1896 DEM and (C) 1896-2010 elevation difference. Dotted lines indicate areas of surface depressions (B) and black oval shows outlet of subglacial meltwater in 1896 (B). Yellow dots mark locations of GCPs (A). Elevation profile of Figure 3.7 taken along solid black line (C).

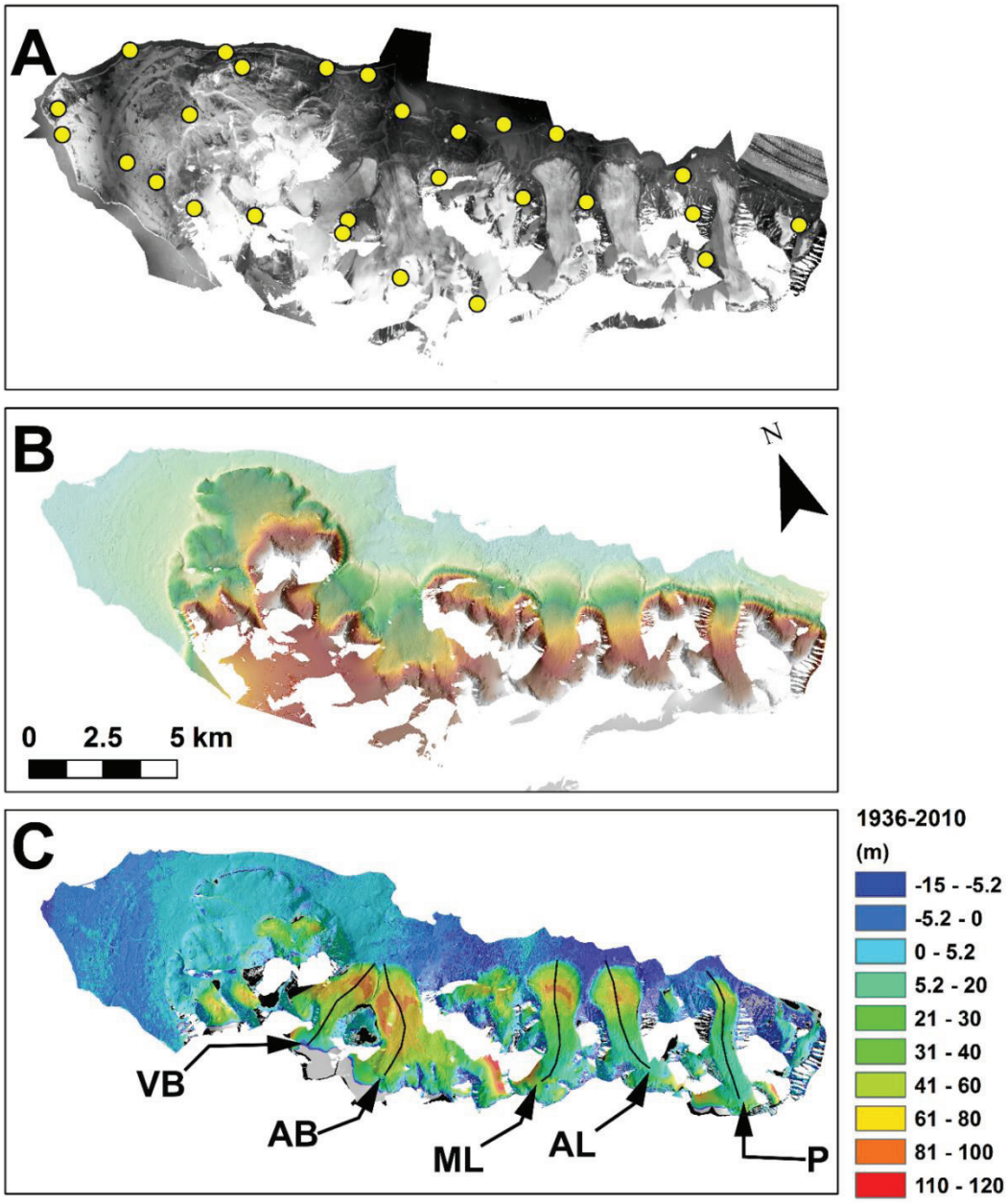

Figure 3.5: (A) Ny Ålesund orthoimage, (B) 1936 DEM and (C) 1936-2010 elevation difference. Yellow dots mark locations of GCPs (A). Elevation profiles of Figure 3.7 taken along solid black lines with individual glaciers marked (C).

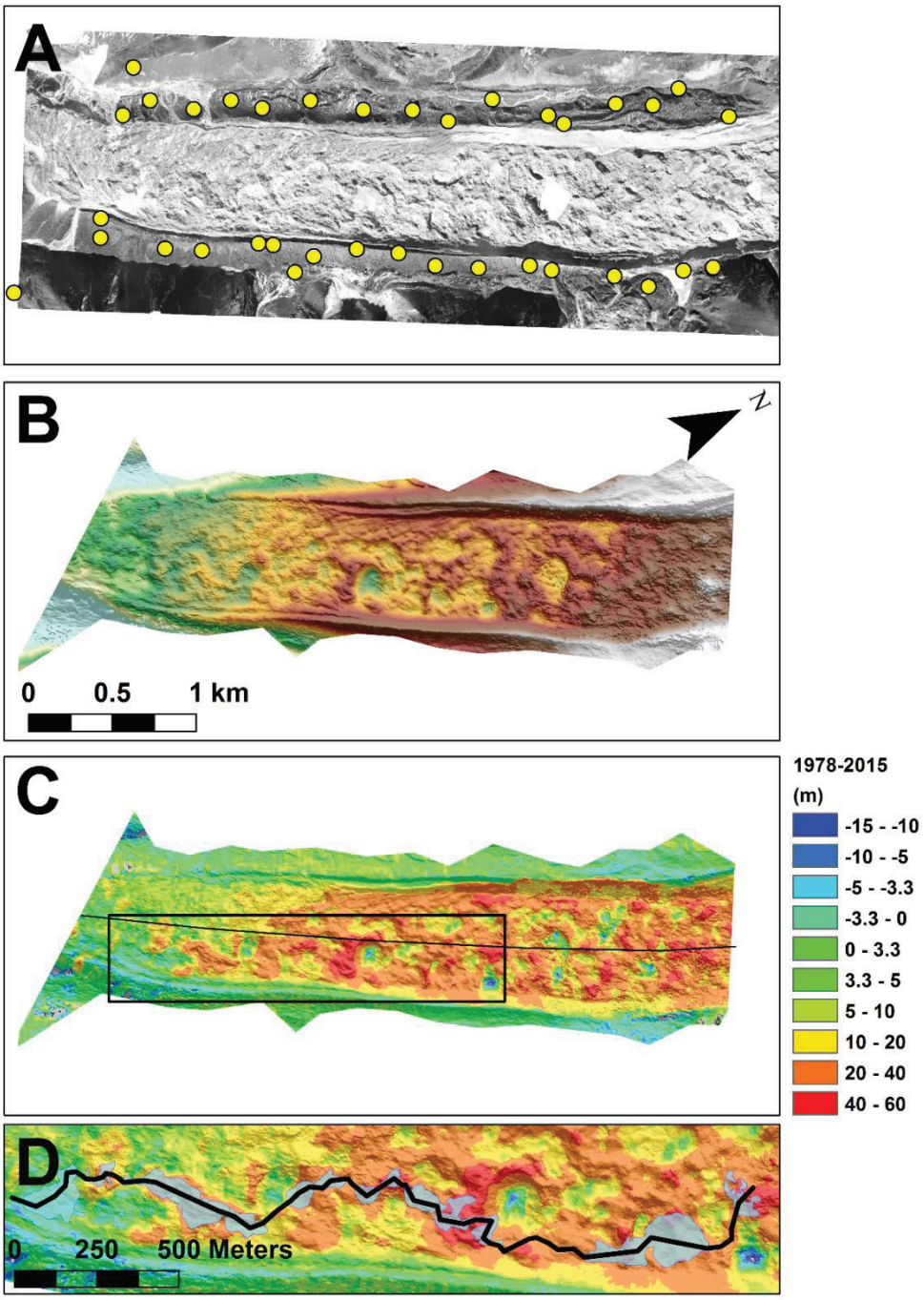

Figure 3.6: (A) Khumbu glacier orthoimage, (B) 1978 DEM, (C) 1978-2015 elevation difference and (D) 2015 lake system with Figure 3.12 transect (black). Yellow dots mark locations of GCPs (A). Elevation profile of Figure 3.7 taken along solid black line (C).

Elevation Profiles

We have extracted elevation profiles (black lines in Figures 3.4, 3.5 and 3.6 C) from each site to assess the detailed surface data as well as compare previous glacier surfaces to recent data (Figure 3.7). For the Ny Ålesund site, we have chosen 5 glaciers. From west to east, these glaciers are Vestre Brøggerbreen, Austre Brøggerbreen, Midtre Lovénbreen, Austre Lovénbreen and Pedersenbreen (Figure 3.5, C).

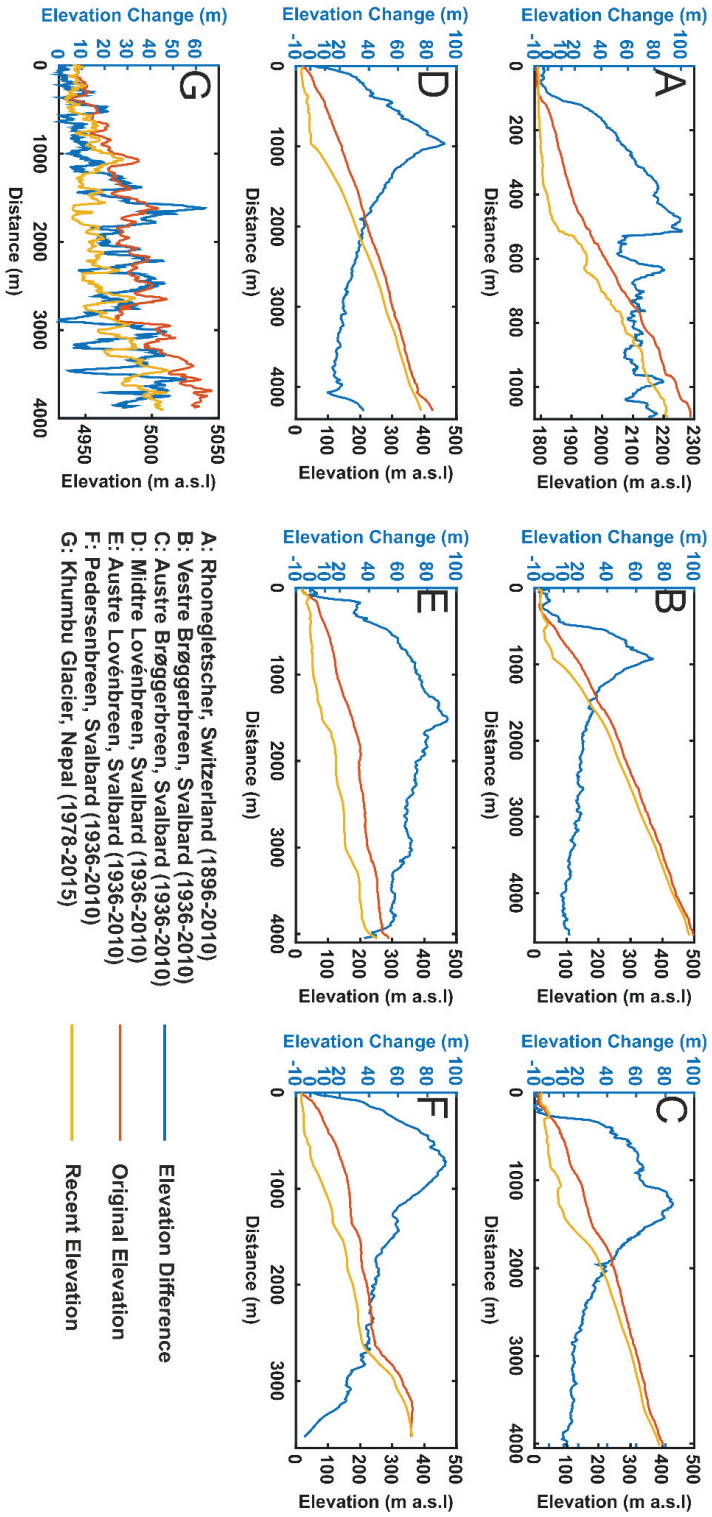

Figure 3.7: Elevation profiles from transects marked in Figure 3.4, 3.5 and 3.6.

Focal Lengths and Ground Sampling Distance

In order to constrain the potential DEM resolutions we could achieve using oblique and high-oblique imagery, we calculated the estimated mean ground sampling distance (GSD) based on the final estimated camera IO and EO information. As mentioned previously, it was possible to calculate the focal lengths of each image based on the estimated IO parameters and knowledge of the camera sensor size. Though we know the focal length of the imagery from Ny Ålesund, we decided to not use it for model generation and therefore assess how well the software could estimate it based on the GCP data.

The Rhone glacier imagery, which was taken on a 9x12 cm plate camera, is estimated to have been taken with a mean focal length of 147±2.6 mm. The Ny Ålesund imagery, taken on an 18x18 cm film, is estimated to have been taken with a mean focal length of 208±1.2 mm, only 2 mm less than the given focal length. The Khumbu imagery on the other hand, taken on 35 mm film by multiple persons, shows numerous focal lengths, which is ultimately why we chose to not group the photos together (Figure 3.8). There are clusters of images that appear generally consistent, such as images from GF14, which have a mean focal length of 33±1.3 mm and likewise with images from GY01 which have a mean focal length 60±3.8 mm. Photographs from the GN07 have a large spread of focal lengths and, in fact, many of these photos appear to be zoomed in on smaller areas when compared to those of the GF or GY series.

Using these focal length data in the field of view formulae, we find the Rhone imagery has a 44° horizontal and 34° vertical field of view. This was verified by manually

identifying objects near the horizontal and vertical edges of the images, and matching these with objects in the 2010 orthoimage. We calculated a horizontal FOV of 43.8° and a vertical FOV of 33.9° based on the angle made by these points and the estimate camera locations. The fields of view for the Ny Ålesund imagery are 46° for both the horizontal and vertical. The Khumbu imagery, being a mixture of focal lengths, shows mean horizontal and vertical fields of view of 59° and 41° for the GF14 imagery, 35° and 24° for the GY01 images and variable field of view for the GY07 and GN07 imagery.

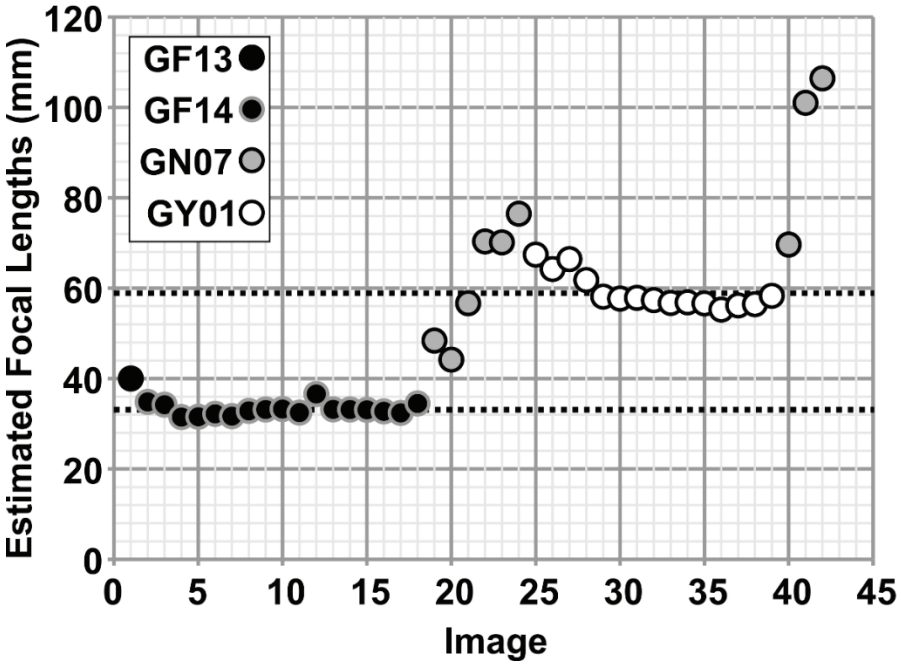

Figure 3.8: Scatter plot of estimated focal lengths of the images used for reconstruction of the Khumbu glacier. Note the two distinct focal lengths of ~33 mm and ~60 mm (GF14 and GY01) as well as imagery taken on one camera at multiple focal lengths (GN07).

The estimated mean GSD calculated using the camera locations as well as the calculated fields of view is shown in Figure 3.9. For all three sites the GSD decreases with

increasing distance from the cameras yet for our image resolutions and camera positions, our areas of interest all have potentially high GSD. For the Rhone glacier, the GSD ranges from 0.18-0.52 m pix^{-1} (Figure 3.9, A), which, when investigating the photographs appears to be accurate as it is possible to make out the window frames of the Hotel Belvédère, on the far mountain ridge. These frames are made up of 1-3 pixels and, at 0.5 m pix^{-1}, this results in a realistic window frame size. In the nearer foreground of one picture, we can see a small hut and two figures on the very edge of the glacier. The figures are roughly 6 pixels high, which in this area with a GSD of 0.25-0.30 m pix^{-1} would amount to persons with heights of 1.5-1.8 m.

In Ny Ålesund the GSD ranges from 1.32-2.87 m pix^{-1} (Figure 3.9, B). Differencing the 5 m 2010 DEM from the 1936 DEM reveals patterns of surface drainage on glaciers that could be meltwater channels with widths and depths within these GSD ranges. The furthest away mountain ridge, within our area of interest has a GSD of maximum ~2.5 m pix^{-1}, which even today is considered a high resolution. Image quality of those distance areas is quite low, however, and often lacks texture and contrast, making it difficult to pinpoint potential GCPs from the imagery.

The Khumbu glacier GSD ranges from 0.36-0.90 m pix^{-1}, based on the average focal length coverage per pixel (Figure 3.9, C). The area in the central part of the glacier tongue has the best GSD as the GY01 photographs were taken in a circular pattern above this area at a focal length of ~60 mm at near nadir. Many of the other parts of the area are covered with wither few large focal length images or many wide angle, ~33 mm focal length images from a distance.

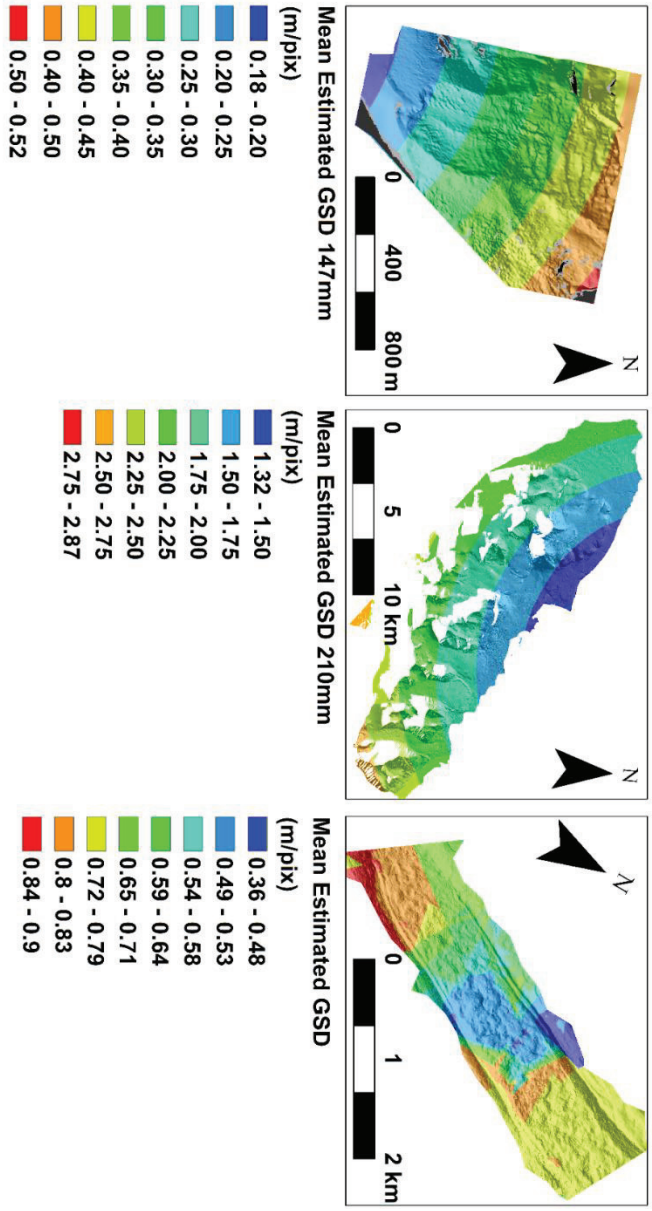

Figure 3.9: Estimated GSD for all sites calculated with estimated IO and EO information from Photoscan.

Discussion

Our results demonstrate the potential for using historical imagery to create DEMs of numerous glaciated regions including alpine glaciers, high-arctic clean ice glaciers and heavily debris-covered Himalayan glaciers, using a variety of imagery from numerous time periods. Here we present details about the quality of our resulting DEMs and orthoimages and offer possible explanations for erroneous areas. Finally, we use the observed changes between the earlier DEMs and the more recent DEMs to discuss differences in the patterns of long term glacier surface change at the three sites.

DEMs and Orthophotos

For all study sites the spatial distribution of off-glacier DEM differences appears largely uniform, within the limits of our calculated $\Delta Z\sigma$. The $\Delta Z\sigma$ of ±5.4, 5.2, and 3.3 m for the Rhone glacier, Ny Ålesund and the Khumbu glacier respectively, represent percentage errors as small as ~5% in the areas of greatest change. In comparison to qualities and accuracies of current high resolution DEM products, Aguilar et al. (2014) found that even by using 12 GCPs with sub-decimeter accuracy, very high-resolution DEMs generated from GeoEye (~0.46 m panchromatic resolution) and Worldview 2 (~0.48 m resolution) could still only reach LE90 accuracies of ±2.04 m and 2.56 m respectively when compared to high resolution LiDAR data. Our errors, being larger than those found by Aguilar et al. (2014), are still reasonable considering that we were not using high precision GCPs, our placement processes lacked well-defined targets, and we were limited by the accuracy, resolution and error of our current DEMs (e.g. 5x5 m resolution, ±2-3 m error in Brøggerhalvøya).

The generated orthophotos and DEMs for all three sites are of sufficiently high quality and resolution to detect changes in the glacier surfaces over the sampled time intervals both through visual inspection and DEM differencing. Removing areas that statistically represent outliers, we can also remove sections of the orthoimages where over interpolation causes extreme image warping. Our end results are, in most cases, smooth orthoimages that appear very closely aligned to current orthoimagery.

The DEMs for all three locations appear to have only small areas of questionable quality. By viewing the DEMs with a hillshade overlay it becomes easier to identify the interpolated regions along edges as coinciding with areas of limited visibility (e.g. behind Ny Ålesund mountains). The Khumbu glacier DEM shows some signs of noise in the lower and upper sections of the DEM. As the majority of the images used were taken above the central region, it is not unexpected that the upper and lower sections should have more noise, they may have 6-8 image overlap, but much of it is from similar viewpoints, with greater distances between the ground and cameras. The detected points in these two areas may therefore have a higher reconstruction uncertainty, such as previously mentioned for the Rhone glacier.

Aside from poor reconstruction in areas of limited camera coverage or high viewing angles, the only other areas where there was difficulty extracting data were in locations with poor lighting or limited contrast. Many of the mountainsides in the Ny Ålesund DEM have vertical gullies running downslope which cause alternating light and dark surfaces under the oblique sun angle. Positional errors on hillslopes can lead to higher Z

error due to the fact that a horizontal difference in one direction creates a vertical difference dependent on the slope angle (Nuth and Kääb, 2011).

While the Ny Ålesund and Khumbu DEMs provide nearly complete spatial coverage across the glaciers, the Rhone glacier DEM exhibits interpolation errors that are unique to its image dataset. For example, the DEM suffers from numerous areas of warping that are most likely caused by the terrestrial aspect of the camera position and the angle of the glacier surface. These highly oblique angles mean that some portions of the glacier are hidden from view in shadows, such as the area behind a large rock or ice block, and the model interpolates over and stretches the images in these shadowed regions. However, viewing the scene from the perspective of a person on the ground, these areas are not visible, and the scene itself appears to be of high quality (Figure 3.10). In addition to the camera position of Rhone imagery, the older acquisition date of 1896, means the image quality is lower, due to increased noise from ageing and lack of detail and contrast, contributing to fewer matched features. Of the series of Rhone glacier images taken in 1896, these three images are the only ones that we could successfully align, but using only three images is not an ideal situation as it limits the number and quality of the points matched between image pairs. Perhaps with more than three images, the maximum reconstruction uncertainty would decrease.

Figure 3.10: Virtual view of the lower Rhone glacier as it was in 1896. The concave wall in the center of the terminus is the outlet of the englacial/subglacial meltwater.

Despite the limitations discussed above, using archived photographs as a data source for SfM surface model generation can provide valuable information. For the purpose of studying changes in glacier surface patterns over very long time intervals, our results have a small percentage error in relation to the changes detected and can offer an excellent opportunity to extend the time series of glacier observations back beyond the current period of abundant data sets, providing context to higher temporal resolution recent assessments of glacier surface change and also providing insights into glacier behavior over longer timescales.

Observations

All three glaciers experienced significant retreat and/or downwasting over the respective periods of observation. The lower Rhone glacier has completely disappeared from the study area. Of the five Ny Ålesund glaciers, four exhibit a similar pattern of retreat and strong downwasting at the terminus, with less surface lowering up glacier. In contrast, Austre Lovénbreen exhibits significant downwasting over the whole area of investigation. Although the pattern of downwasting on the Khumbu glacier exhibits extreme heterogeneity, little downwasting is evident in the terminus regions with high downwasting rate displaced up-glacier.

The Rhone glacier terminus transitioned from an elevation of 1790 m a.s.l. to ~2210 m a.s.l. The elevation profile shows the maximum thinning along the centerline was located at the foot of the steep underlying valley wall (Figure 3.7, A). Discharge from the glacier exited at the concave wall located in the center of the terminus (Figure 3.4, B, black circle, Figure 3.10). Upglacier from this feature there are two surface depressions running along the glacier length (Figure 3.4, B, dashed lines). To the west this depression occurs in a highly-crevassed region, while to the east it occurs below a crevassed region and contains a surface meltwater channel which exits the surface only a few meters to the east of the observed subglacial drainage. Since the early 1980s the terminus has retreated another 375 m. The melting of the lower Rhone glacier removed roughly $18.5*10^7$ $\pm 0.2*10^7$ m^3 of ice over an area of $4.05*10^5$ m^2. Over the period of 1896-1980 this amount of melt would correspond to an annual surface lowering of 0.54 m/y in the lower tongue.

The five glaciers in Ny Ålesund all show similar patterns of surface lowering, with localized accentuated lowering in the central terminus region followed by a gradual decrease in lowering up glacier (Figure 3.5, C & Figure 3.7 B-F). Austre Lovénbreen, however, displays a much more pronounced overall thinning pattern where the measured thinning, 3 km from the 1936 terminus, is still ~69±5.2 m, in contrast to a mean of 25±5.2 m for the other glaciers. Vestre and Austre Brøggerbreen show peak melting along the transects of 71 m and 85±5.2 m respectively, whereas the remaining three glaciers show values of 92 m, 94 m and 93±5.2 m for Midtre Lovénbreen, Austre Lovénbreen and Pedersenbreen respectively (Figure 3.7, B-F). The maximum thinning rates from 1936-2010, along the transects are 0.96 m a^{-1}, 1.14 m a^{-1}, 1.24 m a^{-1}, 1.27 m a^{-1} and 1.26±0.07 m a^{-1}, with mean thinning rates of 0.31 m a^{-1}, 0.48 m a^{-1}, 0.51 m a^{-1}, 0.86 m a^{-1} and 0.65 m a^{-1} from west to east respectively.

Nuth et al. (2007) constructed a DEM for a large portion of Svalbard based on 50 m contour lines extracted from the 1938 topographic map of Svalbard which is based on the aerial oblique imagery of 1936 and 1938. Their DEM was differenced with the 1990 DEM, NP_S0_DTM20_199095_33, which has a 20 m resolution with a horizontal accuracy of ±2-3 m (NPI, 2014). We have differenced our Ny Ålesund DEM with the 1990 DEM and calculated the average elevation changes curves of our five glaciers. Our values fit closely with the average values of Prins Karls Forland and Brøggerhalvøya (Figure 3.11). The accuracy of the values in the 400-500 m altitudes are questionable as there may be influences from over interpolated edges, however, as a comparison, our data fits well with the previously calculated data.

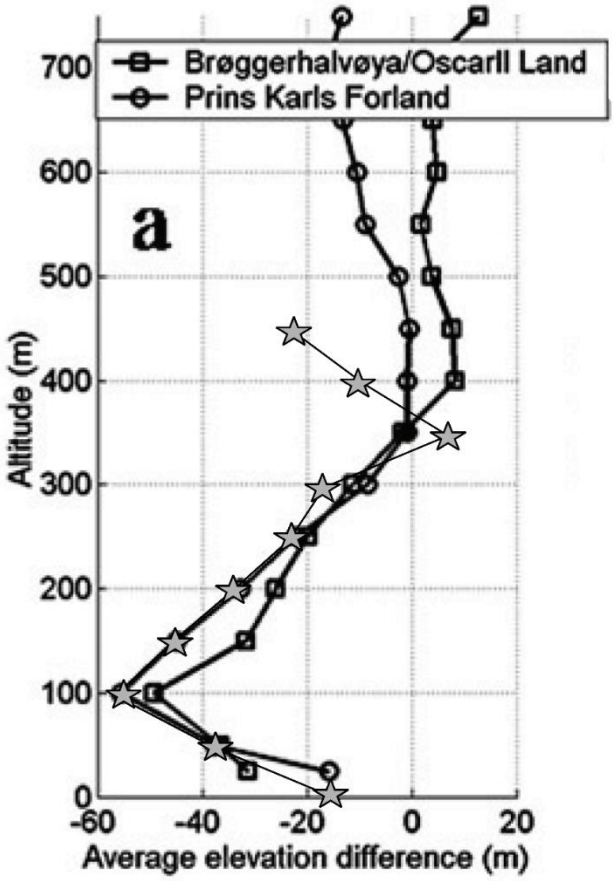

Figure 3.11: Mean elevation changes of 5 Ny Ålesund glaciers compared to results from Nuth et. al. (2007) comprised of all glaciers in the Brøggerhalvøya/Oscar II Land and Prins Karls Forland areas. Data from this study are plotted with gray stars and show very similar results with other glaciers in this region (Figure adapted from Nuth et al. (2007)).

While the Rhone glacier and the glaciers in the Ny Ålesund area are clean-ice glaciers, which, exhibit relatively smooth elevation profiles and similar thinning profiles (Figure 3.7), the Khumbu glacier is a highly debris-covered glacier which exhibits hummocky topography and highly variable spatial thinning patterns (Figure 3.6 B and C). The lower 1 km of the Khumbu appears to have undergone very little change over the 37-year period, showing average thinning along the transect of 7.5±3.3 m. Upglacier from here

the difference map demonstrates large variability in spatial patterns of downwasting with a maximum of 64.1±3.3 m, a minimum of -12.5±3.3 m and a mean thinning of 28.6±3.3 m.

The high degree of spatial variability in downwasting rates reflects the critical control of debris thickness on melt rates. Where debris layer thickness exceeds a few 10s of cm, little sub-debris melt can occur (Nakawo and Rana, 1999, Nicholson and Benn, 2006, Reznichenko et al., 2010). Consequently, non-uniform debris distributions create heterogeneous melt patterns that result in uneven, hummocky surface topography (e.g. Figure 3.6, B; Figure 3.12, dotted line). Thick accumulations of debris at down-glacier sites have resulted in limited to no downwasting. Further up glacier, thinner and more partial debris cover allows rapid, patchy downwasting in hot spots due to debris redistribution. Areas with steep surface slopes can increase, material can be redistributed through slumping, newly exposed ice can melt rapidly, increased surface meltwater production can lead to pond and lake formation, and subsequent lake margin calving can cause rapid backwasting of exposed ice faces (Watanabe et al., 1986, Sakai et al., 2000, Benn et al., 2001, Gulley and Benn, 2007, Röhl, 2008, Reid and Brock, 2014, Thompson et al., 2016).

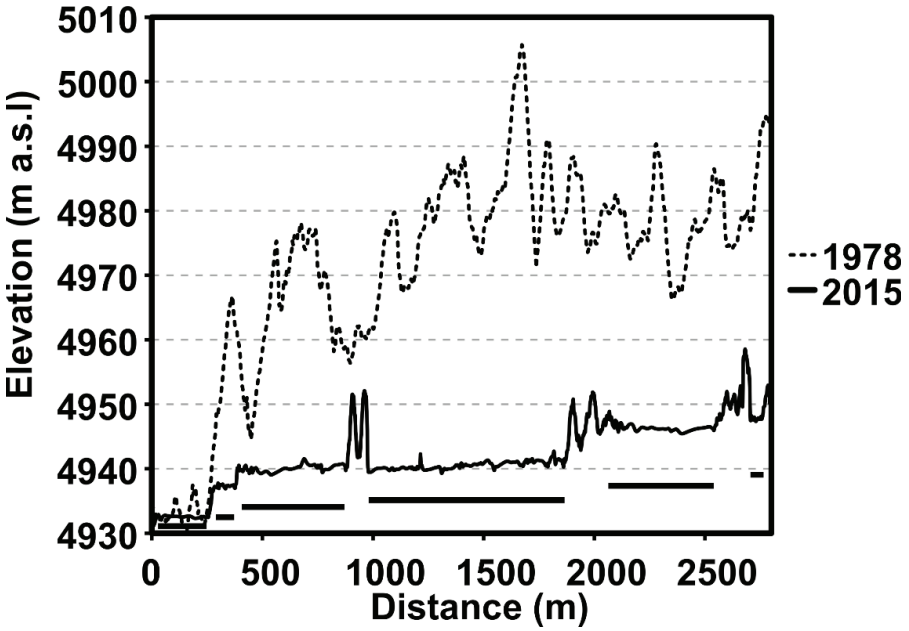

Figure 3.12: Elevation profile from lake system transect of the Khumbu glacier. Solid black horizontal bars indicate the locations of lake bodies in 2015.

In summary, we have demonstrated how, through the use of historic imagery and modern remote sensing products, it is possible to extract reliable, high-resolution DEMs and orthoimagery of glaciers from 38, 80 and 120 years ago. By searching through online databases for overlapping imagery of glaciers, even with a minimum of 3 photos (in the Rhone glacier case) it is possible to extract high quality geometric information using SfM technology. We have shown that the method can successfully extract the data and, if given enough reliable GCPs, its can also estimate the camera IO and EO information. Our analysis of off-glacier error shows that the method produces accurate DEMs within the areas visible from numerous cameras and that relative to the timespans between the historic imagery and the current imagery, the errors are small. Using the estimated IO and

EO information we have been able to calculate estimated potential maximum GSDs, which, even when using aerial high-oblique imagery, can be on the order of ~2-3 m or less. Our DEM differencing shows trends similar to numerous other studies and measurements performed in our selected regions. Elevation profiles from our glaciers demonstrates how differently glaciers from the High-Arctic, European Alps and the Himalayas, both clean and debris-covered, have responded to the warming climate over the last ~40-100 years.

Conclusion

Our results demonstrate that using SfM to create DEMs from historical images offers a powerful new tool for characterizing patterns of glacier downwasting. DEMs constructed from historical imagery can fill in gaps where no other remotely sensed, or field data exist. In the case of the Rhone glacier, the temporal coverage of the repeated photographs means it could be possible to reconstruct multiple DEMs of the lower Rhone and more accurately measure the disintegration of the glacier tongue from the late 1800s through ~1980. It would be possible to create models with detail such as shown in Figure 3.10 and animate the retreat of the terminus up the valley wall. Older oblique imagery can now be successfully used to extract DEMs of objects in the foreground. Terrestrial imagery can also be used, so long as there is sufficient coverage of off-glacier areas to identify GCPs. Even using mixed focal lengths can still yield high quality results suitable for observing glacial change. The application of SfM to such imagery can not only unlock the past and contribute to a better understanding of current and future trends in glacier climate interactions, but it can also help to increase knowledge on the development and

evolution of debris-covered glaciers. By allowing us to better understand how and at what rates, surface processes occur we can develop a better sequence behind the glacier surfaces we see today, and more accurately forecast how the surface will evolve in the future.

Acknowledgements

Jordan R. Mertes acknowledges funding from Michigan Technological University and The Michigan Technological University 2016 Fall Finishing Fellowship. The authors would like to thank the Norske Polar Institute for use of the low-resolution oblique photos and Christian Ginzler for access to a subset of the 2010 Rhone DEM and imagery. Pleiades data was made available by ACINN via the Austrian FFG ASAP project GlHima-Sat, project Nr. 847999.

References

Agarwal S, Furukawa Y, Snavely N, Simon I, Curless B, Seitz SM, Szeliski R. 2011. Building rome in a day. Communications of the ACM **54**: 105-112

Agisoft, 2014. Agisoft PhotoScan User Manual. In *Professional Edition, Version 1*. Agisoft LLC: http://www.agisoft.ru/pdf/photoscan_pro_1_0_en.pdfhttp://www.agisoft.ru/pdf/photoscan_pro_1_0_en.pdf, http://www.agisoft.ru/pdf/photoscan_pro_1_0_en.pdf

Aguilar MÁ, del Mar Saldaña M, Aguilar FJ. 2014. Generation and quality assessment of stereo-extracted DSM from GeoEye-1 and WorldView-2 imagery. IEEE Transactions on Geoscience and Remote Sensing **52**: 1259-1271. DOI: 10.1109/TGRS.2013.2249521

Benn DI, Wiseman S, Hands KA. 2001. Growth and drainage of supraglacial lakes on debrismantled Ngozumpa Glacier, Khumbu Himal, Nepal. Journal of Glaciology **47**: 626-638. DOI: 10.3189/172756501781831729

Bhambri R, Bolch T, Chaujar RK, Kulshreshtha SC. 2011. Glacier changes in the Garhwal Himalaya, India, from 1968 to 2006 based on remote sensing. Journal of Glaciology **57**: 543-556. DOI: 10.3189/002214311796905604

Bhardwaj A, Sam L, Bhardwaj A, Martín-Torres FJ. 2016a. LiDAR remote sensing of the cryosphere: Present applications and future prospects. Remote Sensing of Environment **177**: 125-143. DOI: 10.1016/j.rse.2016.02.031

Bhardwaj A, Sam L, Martín-Torres FJ, Kumar R. 2016b. UAVs as remote sensing platform in glaciology: Present applications and future prospects. Remote Sensing of Environment **175**: 196-204. DOI: 10.1016/j.rse.2015.12.029

Bjørk AA, Kjær KH, Korsgaard NJ, Khan SA, Kjeldsen KK, Andresen CS, Larsen NK, Funder S. 2012. An aerial view of 80 years of climate-related glacier fluctuations in southeast Greenland. Nature Geoscience **5**: 427-432. DOI: 10.1038/ngeo1481

Bolch T, Pieczonka T, Benn D. 2011. Multi-decadal mass loss of glaciers in the Everest area (Nepal Himalaya) derived from stereo imagery. The Cryosphere **5**: 349-358. DOI: 10.5194/tc-5-349-2011

Braithwaite RJ, Raper SC, Candela R. 2013. Recent changes (1991–2010) in glacier mass balance and air temperature in the European Alps. Annals of Glaciology **54**: 139-146. DOI: 10.3189/2013AoG63A285

Carter HA. 1985. Classification of the Himalaya. American Alpine Journal **27**: 122-123

Debenham F. 1938. Norwegian Expedition to Svalbard, 1938. Polar Record **3**: 5-6. DOI: 10.1017/S003224740003802X

Diolaiuti G, Bocchiola D, D'agata C, Smiraglia C. 2012. Evidence of climate change impact upon glaciers' recession within the Italian Alps. Theoretical and Applied Climatology **109**: 429-445. DOI: 10.1007/s00704-012-0589-y

ETH-Bibliothek. 2016. Rhonegletscher 30-Aug-1896. In *Glaziologische Kommission der SANW (Archiv)*, e-pics Online Database. ETH Bibliothek: Zurich. http://www.e-pics.ethz.ch/. DOI: http://goi.org/10.3932/ethz-a-000016893

http://goi.org/10.3932/ethz-a-000016894

http://goi.org/10.3932/ethz-a-000016896
Ginzler C, Hobi ML. 2015. Countrywide stereo-image matching for updating digital surface models in the framework of the Swiss national forest inventory. Remote Sensing **7**: 4343-4370
Gruen A, Murai S. 2002. High-resolution 3D modelling and visualization of Mount Everest. ISPRS journal of photogrammetry and remote sensing **57**: 102-113
Gulley J, Benn DI. 2007. Structural control of englacial drainage systems in Himalayan debris-covered glaciers. Journal of Glaciology **53**: 399-412. DOI: 10.3189/002214307783258378
Hagen JO, Kohler J, Melvold K, Winther JG. 2003. Glaciers in Svalbard: mass balance, runoff and freshwater flux. Polar Research **22**: 145-159
Immerzeel WW, van Beek LP, Bierkens MF. 2010. Climate change will affect the Asian water towers. Science **328**: 1382-1385
Jouvet G, Huss M, Blatter H, Picasso M, Rappaz J. 2009. Numerical simulation of Rhonegletscher from 1874 to 2100. Journal of Computational Physics **228**: 6426-6439
Kamp U, Byrne M, Bolch T. 2011. Glacier fluctuations between 1975 and 2008 in the Greater Himalaya Range of Zanskar, southern Ladakh. Journal of Mountain Science **8**: 374-389. DOI: 10.1007/s11629-011-2007-9
López-Moreno JI, Fontaneda S, Bazo J, Revuelto J, Azorin-Molina C, Valero-Garcés B, Morán-Tejeda E, Vicente-Serrano SM, Zubieta R, Alejo-Cochachín J. 2014. Recent glacier retreat and climate trends in Cordillera Huaytapallana, Peru. Global and Planetary Change **112**: 1-11. DOI: 10.1016/j.gloplacha.2013.10.010
Mercanton P-L, Heim A, Held L, Rütimeyer L. 1916. Vermessungen am Rhonegletscher: Mensurations au glacier du Rhône. 1874-1915. Zürcher & Furrer
Nakawo M, Rana B. 1999. Estimate of Ablation Rate of Glacier Ice under a Supraglacial Debris Layer. Geografiska Annaler: Series A, Physical Geography **81**: 695-701. DOI: 10.1111/1468-0459.00097
Nakawo M, Yabuki H, Sakai A. 1999. Characteristics of Khumbu Glacier, Nepal Himalaya: recent change in the debris-covered area. Annals of Glaciology **28**: 118-122
Nicholson L, Benn DI. 2006. Calculating ice melt beneath a debris layer using meteorological data. Journal of Glaciology **52**: 463-470. DOI: 10.3189/172756506781828584
NPI. 2014. Terrengmodell Svalbard: NP_S0_DTM5_2010_13828_33. Tromso, Norway. https://data.npolar.no/dataset/dce53a47-c726-4845-85c3-a65b46fe2fea
Nuth C, Kääb A. 2011. Co-registration and bias corrections of satellite elevation data sets for quantifying glacier thickness change. The Cryosphere **5**: 271-290
Nuth C, Kohler J, Aas HF, Brandt O, Hagen JO. 2007. Glacier geometry and elevation changes on Svalbard (1936-90): a baseline dataset. Annals of Glaciology **46**: 106-116. DOI: 10.3189/172756407782871440
Paul F, Kääb A, Haeberli W. 2007. Recent glacier changes in the Alps observed by satellite: Consequences for future monitoring strategies. Global and Planetary Change **56**: 111-122. DOI: 10.1016/j.gloplacha.2006.07.001

Quincey DJ, Luckman A, Benn D. 2009. Quantification of Everest region glacier velocities between 1992 and 2002, using satellite radar interferometry and feature tracking. Journal of Glaciology **55**: 596-606. DOI: 10.3189/002214309789470987
Reid T, Brock B. 2014. Assessing ice-cliff backwasting and its contribution to total ablation of debris-covered Miage glacier, Mont Blanc massif, Italy. Journal of Glaciology **60**: 3. DOI: 10.3189/2014JoG13J045
Reznichenko N, Davies T, Shulmeister J, McSaveney M. 2010. Effects of debris on ice-surface melting rates: an experimental study. Journal of Glaciology **56**: 384-394. DOI: 10.3189/002214310792447725
Roderik JW, Van De Wal S. 1998. Sensitivity of Rhonegletscher, Switzerland, to climate change: experiments with a one-dimensional flowline model. Journal of Glaciology **44**: 383-393
Röhl K. 2008. Characteristics and evolution of supraglacial ponds on debris-covered Tasman Glacier, New Zealand. Journal of Glaciology **54**: 867-880. DOI: 10.3189/002214308787779861
Sakai A, Takeuchi N, Fujita K, Nakawo M. 2000. Role of supraglacial ponds in the ablation process of a debris-covered glacier in the Nepal Himalayas. IAHS PUBLICATION: 119-132
Silverio W, Jaquet J-M. 2005. Glacial cover mapping (1987–1996) of the Cordillera Blanca (Peru) using satellite imagery. Remote Sensing of Environment **95**: 342-350. DOI: 10.1016/j.rse.2004.12.012
Soruco A, Vincent C, Rabatel A, Francou B, Thibert E, Sicart JE, Condom T. 2015. Contribution of glacier runoff to water resources of La Paz city, Bolivia (16 S). Annals of Glaciology **56**: 147-154. DOI: 10.3189/2015AoG70A001
Sugiyama S, Bauder A, Zahno C, Funk M. 2007. Evolution of Rhonegletscher, Switzerland, over the past 125 years and in the future: application of an improved flowline model. Annals of Glaciology **46**: 268-274
Surazakov A, Aizen V, Aizen E, Nikitin S. 2007. Glacier changes in the Siberian Altai Mountains, Ob river basin,(1952–2006) estimated with high resolution imagery. Environmental Research Letters **2**: 045017. DOI: 10.1088/1748-9326/2/4/045017
Thompson S, Benn DI, Mertes J, Luckman A. 2016. Stagnation and mass loss on a Himalayan debris-covered glacier: processes, patterns and rates. Journal of Glaciology: 1-19. DOI: 10.1017/jog.2016.37
Thorsteinsson T, Jóhannesson T, Snorrason Á. 2013. Glaciers and ice caps: Vulnerable water resources in a warming climate. Current Opinion in Environmental Sustainability **5**: 590-598. DOI: 10.1016/j.cosust.2013.11.003
Unger-Shayesteh K, Vorogushyn S, Farinotti D, Gafurov A, Duethmann D, Mandychev A, Merz B. 2013. What do we know about past changes in the water cycle of Central Asian headwaters? A review. Global and Planetary Change **110**: 4-25. DOI: 10.1016/j.gloplacha.2013.02.004
Wallinga J, Wal RSWVD. 1998. Sensitivity of Rhonegletscher, Switzerland, to climate change: experiments with a one-dimensional flowline model. Journal of Glaciology **44**: 383-393. DOI: 10.3198/1998JoG44-147-383-393

Wang S, Liu H, Yu B, Zhou G, Cheng X. 2016. Revealing the early ice flow patterns with historical Declassified Intelligence Satellite Photographs back to 1960s. Geophysical Research Letters **43**: 5758-5767. DOI: 10.1002/2016GL068990
Watanabe O, Iwata S, Fushimi H. 1986. Topographic characteristics in the ablation area of the Khumbu Glacier, Nepal Himalaya. Annals of Glaciology **8**: 177-180
Yabuki H, Secretary Office, 2011, Aerial photographs of glaciers in the Nepal Himalayas obtained during the Glaciological Expedition in Nepal (GEN) at 1978g #1., 1.00, CrDAP, JAMSTEC, https://ads.nipr.ac.jp/dataset/C20121022-020
Yabuki H, GEN-(Nagoya University TJSoSaI, 2012. Aerial photographs of glaciers in Nepal Himalaya obtained during the Glaciological Expedition in Nepal from 1974 to 1978. CrDAP J (ed). distributed by CrDAP, Digital media: Yokosuka, Japan

Chapter 4. A Conceptual Model of Supraglacial Lake Formation on Debris-covered Glaciers based on GPR Facies Analysis[4]

Abstract

Supraglacial lakes and ponds can create hotspots of mass loss on debris-covered glaciers. While much research has been directed at understanding lateral lake expansion, little is known about the rates or processes governing lake deepening. To a large degree, this knowledge gap persists due to sparse observations of lake beds. Here we report on the novel use of ground penetrating radar (GPR) surveys to simultaneously collect supraglacial lake bathymetry and bottom composition data from Spillway Lake (surface area of 2.4 x 10^5 m^2; volume of 9.5 x10^4 m^3), which is located in the terminus region of the Ngozumpa Glacier in the Khumbu region of the Nepal Himalaya. We identified two GPR bottom signals corresponding to two sedimentary facies of (1) sub-horizontal layered fine sediment drape and (2) coarse blocky diamict. We provide an understanding of the changes in subaqueous debris distribution that occur through stages of lake expansion by combining the GPR results with *in situ* observations of shoreline deposits matching the interpreted facies. From this, we present an updated conceptual model of supraglacial lake evolution, with the addition of data on the evolving debris environment, showing how dominant depositional processes can change as lakes evolve from perched lakes to multi-basin base-level lakes and finally onto large moraine-dammed lakes. Throughout lake evolution, processes such as shoreline steepening, lakebed collapse into voids and conduit interception, subaerial and subaqueous calving and rapid areal

[4] The material in this chapter was previously published in the journal Earth Surface Processes and Landforms, 19th October 2016.

expansion alter the spatial distribution and makeup of lakebed debris and sediments forcing a number of positive and negative feedbacks on lake expansion.

Introduction

Thick layers of debris on debris-covered glacier tongues have been proposed to insulate debris-covered glaciers from mass loss in response to climate warming by decreasing heat flux to the underlying ice surface (Østrem, 1959, Nakawo and Rana, 1999, Nicholson and Benn, 2006, Reid and Brock, 2010, Reznichenko et al., 2010). However, mass loss on debris-covered glaciers has been shown to be keeping pace with adjacent clean ice glaciers (Gardelle et al., 2012, Kääb et al., 2012). This phenomenon may be attributed to irregular surface evolution due to uneven sub-debris melting leading to the presence of features such as supraglacial lakes and ice cliffs, which act as localized hotspots of melting. These hotspots have been shown to contribute to mass loss significantly, though only making up a very small part of the glacier surface area (Sakai et al., 2000b, Sakai et al., 2002, Reid and Brock, 2014, Buri et al., 2015, Miles et al., 2016, Thompson et al., 2016). Through time however, the growth of supraglacial lakes and the rapid backwasting of bordering ice cliffs, can eventually lead to coalescence with nearby lakes, and increased chances to form potentially dangerous moraine-dammed lakes (Sakai et al., 2000a, Watanabe et al., 2009).

Supraglacial lakes contribute to glacier mass loss by driving melt in the tongues of stagnant, debris-covered glaciers where surface slopes are generally < 2° (Reynolds, 2000, Sakai et al., 2002, Immerzeel et al., 2014, Reid and Brock, 2014, Thompson et al., 2016). With low glacier surface slopes, meltwater and rainfall accumulate in topographic

depressions where they contribute to melt by absorbing and storing incoming radiation as heat (Kirkbride, 1993, Benn et al., 2000, Reynolds, 2000, Sakai et al., 2000b, Benn et al., 2001, Röhl, 2008, Miles et al., 2016). Circulation of warm lake water increases melt around lake margins and stored heat drives subaqueous melting, even when ambient temperatures have decreased below freezing (Sakai et al., 2000a). In addition to melt within lake basins, interception with englacial conduits can transfer warm water to the interior of the glacier contributing to internal ablation (Kirkbride, 1993, Benn et al., 2012, Miles et al., 2016, Thompson et al., 2016).

Much of what is known about the evolution of supraglacial lakes concerns areal expansion and the rates and fundamental processes underpinning areal lake expansion are well established from remote sensing and surface surveys (Mool, 1995, Quincey et al., 2007, Komori, 2008, Fujita et al., 2009, Watanabe et al., 2009, Bajracharya and Mool, 2010, Gardelle et al., 2011, Sawagaki et al., 2012, Thompson et al., 2012, Liu et al., 2015, Wang et al., 2015, Thompson et al., 2016). Far less, however, is known about rates of, and processes controlling, lake deepening. To a large degree, this is because the remote sensing techniques used to measure lake depth on clean ice glaciers (Sneed and Hamilton, 2007, Fitzpatrick et al., 2014), where lakes are clear, do not work in the turbid lakes that are characteristic of debris-covered glaciers. As a result, much of what is known about lake bathymetry has been determined from labor intensive field campaigns which have typically been conducted at irregular intervals.

While many details of lake deepening remain unknown, two physical processes are thought to dominate: subaqueous calving (Röhl, 2008) and direct lakebed melting

(Chikita et al., 1999, Sakai et al., 2000b, Chikita et al., 2001). Subaqueous calving has been observed to remove large volumes of ice from lake beds at a number of glaciers in New Zealand (Kirkbride and Warren, 1997, Warren and Kirkbride, 2003, Röhl, 2008). However, the mechanism relies in part on the buoyancy of ice and doubt remains as to the impact of the subaqueous debris layer (Benn et al., 2012). Melt rates of lakebeds are critically dependent on water temperature as well as the presence or absence of lake bed debris. For example, on the Lirung Glacier, Nepal, low subaqueous melt rates of < 0.01 cm d^{-1} occurred in lake beds covered in sediments, but where lakes were floored with bare ice, subaqueous melt rates were 2-4 cm d^{-1} (Miles et al., 2016).

Improved understanding of the rates and processes of lake deepening requires a detailed temporal and spatial record of lake bathymetric evolution, as well as an understanding of debris distribution and physical characteristics. Most bathymetric survey techniques rely on weighted lines or hand-held electronic sonar devices (Yamada and Sharma, 1993, Kadota, 1994, Benn et al., 2001, Sakai et al., 2003, Yamada et al., 2004, Sakai et al., 2005, Fujita et al., 2009, Sawagaki et al., 2012, Thompson et al., 2012, Somos-Valenzuela et al., 2014, Horodyskyj, 2015, Thompson et al., 2016). These techniques are time consuming and labor intensive, lack fine spatial resolution and provide little to no information about bottom compositions. Improved spatial resolution was obtained from surveys conducted using remotely operated underwater vehicles (ROVs) outfitted with sonar transducers (Horodyskyj, 2015), and sonar data can be analyzed to provide some information about bottom hardness and texture (Kenny et al., 2003) but most commercial sonar systems cannot provide information about debris thickness.

Ground penetrating radar (GPR) is an underutilized tool for characterizing supraglacial lake bathymetry as well as bottom composition and thickness. While GPR has been used to measure glacier depths and ice volume for bathymetric and geological mapping of non-supraglacial lakes (Haeni et al., 1987, Sellmann et al., 1992, Moorman and Michel, 1997, Schwamborn et al., 2002, Arcone et al., 2006, Banks and Johnson, 2011, Sambuelli and Bava, 2012), few studies have used GPR to investigate lakes on debris-covered glaciers (Reynolds, 2011).

In this paper we present the results of GPR surveys of Spillway Lake, Ngozumpa Glacier, Nepal to demonstrate the potential of GPR as an investigative tool for characterization of supraglacial lake bathymetry and lake bed characteristics. We then use a combination of GPR facies analysis (e.g.,Bristow, 1995, Ruffell et al., 2004) and field observations to characterize and interpret the subaqueous debris distribution. Finally, we present an updated conceptual model of debris-covered glacier supraglacial lake evolution that is based on the facies analysis and a review of published literature on supraglacial lakes.

Study Site

Ngozumpa Glacier (27.97°N; 86.69°E) is located in the Khumbu Himal, Nepal, ~25 km west of Sagarmatha (Mt. Everest). The Ngozumpa Glacier flows down from Gyachung Kang (to the northeast) and Cho Oyu (to the northwest) (Figure 4.1). At ~20 km long, the glacier is one of the largest in Nepal, and the lower 15 km is extensively debris covered. Debris thickness is highly variable but generally increases from a thin, discontinuous cover just below the equilibrium line altitude (~5700 m) to the terminus, where it is continuous (excluding ice cliffs) and 1-3 m thick (Benn et al., 2012, Nicholson and Benn,

2012). This debris layer has affected the glacier mass balance and altered the distribution of ablation relative to a clean ice glacier; the maximum ablation now occurs up glacier from the terminus where the debris layer is thin, rather than at the terminus. This ablation pattern has caused a reduction in surface gradient and an associated decrease in the driving stresses (Bolch et al., 2008, Quincey et al., 2009). In recent decades the glacier has experienced substantial surface lowering, and, in the ablation area, the surface now lies >150 m below the Little Ice Age moraines (Sakai and Fujita, 2010). Decreases in surface gradient and driving stresses have ultimately lead to a reduction in glacier velocity which has caused the lower ~7 km of the glacier to become stagnant (Quincey et al., 2009, Thompson et al., 2016).

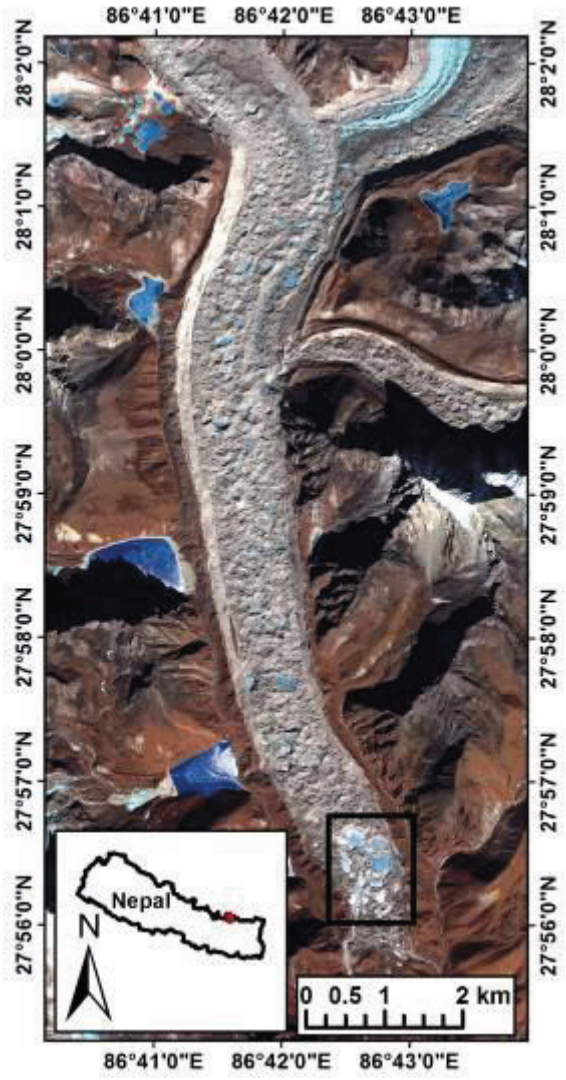

Figure 4.1: Overview Geoeye satellite image of Ngozumpa Glacier with Spillway Lake complex indicated in black rectangle.

The glacier has highly variable surface topography, consisting of large hummocks, ridgelines, lakes and ice cliffs. The surface relief is approximately 10s of meters around larger hummocks and lake ice cliff contacts. The mean surface slope of the lowest 5km has been measured previously at ~2° (Hands, 2004). This slope is within the range cited

as having potential for the formation of extensive supraglacial lakes (i.e. ≤2°) (Reynolds, 2000, Quincey et al., 2007, Röhl, 2008) an in the lowest ~2km where our study focuses, the overall slope decreases to <1°.

In the early 1990s a collection of lakes and ponds began to form at the hydrological base level of the Ngozumpa Glacier (Thompson et al., 2012). Since this time, the lake basins have continued to grow and coalesce to cover an area of 2.4×10^5 m^2 with a volume of 9.5×10^4 m^3 in 2014 (Thompson et al., 2016). This growing lake body is, informally referred to as Spillway Lake. The site has been the focus of a combination of studies using remote sensing, sonar measurements and extensive field mapping (Adhikary et al., 2000, Benn et al., 2001, Benn et al., 2012, Thompson et al., 2012, Horodyskyj, 2015, Thompson et al., 2016). Our new surveys, presented here, focus on two connected basins within the Spillway Lake system, adjacent to the eastern lateral moraine and the central lake basin (Figure 2.2 A, B).

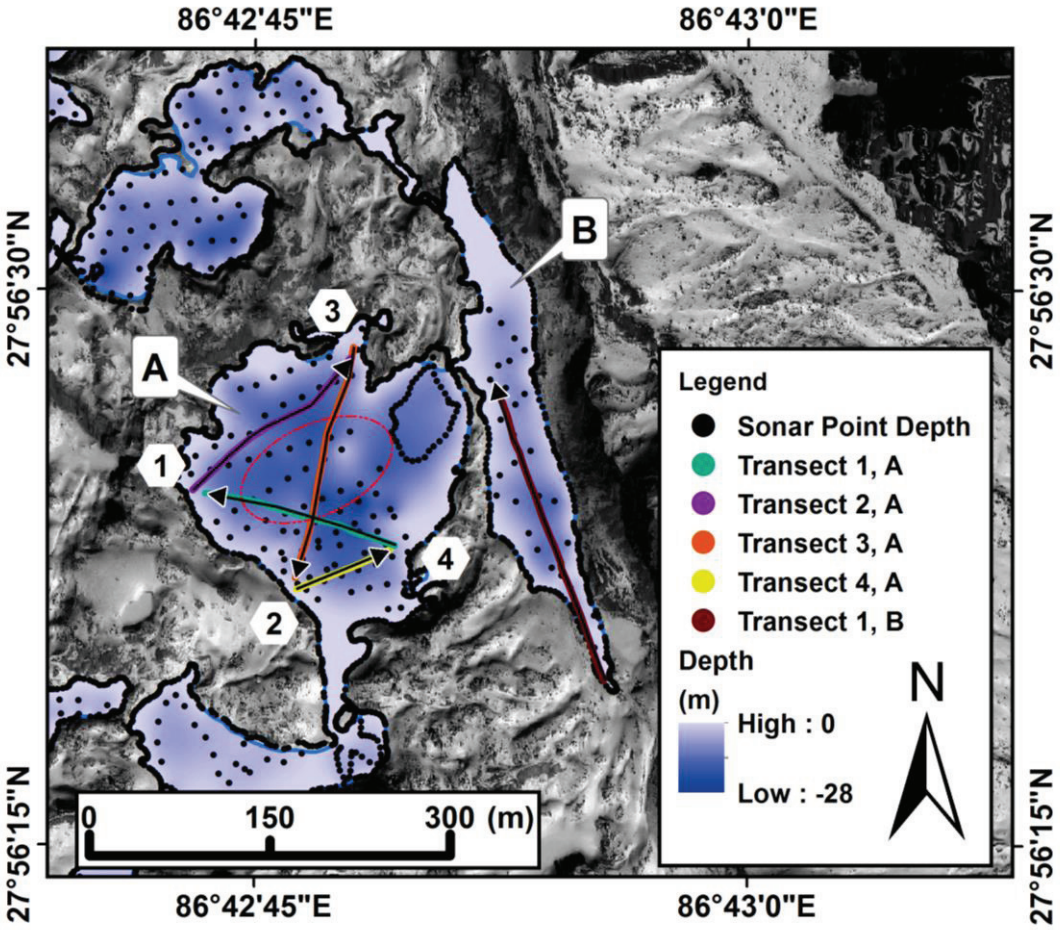

Figure 4.2: Spillway Lake (basins A & B) area of interest shown with interpolated depth map and overlay of sonar point depth locations and GPR transects. Red ellipse indicates area of sparse sonar point measurements along transect 3, A. White hexagons around numbers indicate locations of sediment samples seen near shoreline in Figures 4.9&4.10.

Methods

During December 2014, five GPR transects were surveyed on the frozen surface of Spillway Lake, using a Malå ProEx Professional Explorer GPR system linked to an unshielded Rough Terrain Antenna (RTA) of 25 MHz center frequency. The RTA is roughly 13 m long and houses a single pair of transmitter/receiver antennas separated by 6 m in an inline configuration. During acquisition, the system was connected to a Leica

Differential Global Positioning System (DGPS) rover, and set to record a trace every 0.3 s. The ProEX unit was placed inside an inflatable kayak behind which the RTA was towed. The system was towed on foot at an approximately constant speed of ~1 m s^{-1}. The interval between recorded traces was 0.26 ± 0.06 m, regularized (in Mathworks Matlab® software) to 0.2 m during processing. A bulk correction of 11 m (applied in the opposite direction to the profile heading) was applied to all positions to remove the offset between the DGPS antenna and the midpoint between the GPR antennas. Due to a battery failure in the Leica base station, GPS measurements cannot be post processed and corrected to centimeter accuracy. Therefore, to assure the most accurate transect positioning, we have used field video and photographic data to verify correct positioning of transect start-stop positions relative to high-resolution satellite imagery (~ 0.48 m pan-sharpened GeoEye-1) where possible. Uncorrected DGPS data from sonar surveys, conducted prior to the GPR survey, show errors on the scale of ±1-2 m in the x-y plane.

The effective depth of investigation of a GPR signal is substantially impeded in electrically conductive ground (e.g., high clay fraction and/or saline water content) as the electromagnetic energy of the GPR wavelet is more rapidly absorbed (Annan, 2004). Groundwater is therefore often considered an impediment to GPR surveying. Supraglacial lakes, however, can have very low electrical conductivities, with conductivities of ~2.3 mS m^{-1} to ~12 mS m^{-1} being reported from supraglacial lakes on debris-covered glaciers (Watanabe et al., 1995, Sambuelli and Bava, 2012). These conductivities are close to pure water and lakes should thus be transparent to radar.

The RTA used to conduct our GPR surveys allows for rapid data acquisition, but it does not allow common midpoint (CMP) surveys to be conducted for velocity analysis. As a result, GPR surveys reported here do not provide information about lakebed debris thickness. They can, however, provide information about bottom composition and water depth based on the first arrival of the GPR signal and its character immediately thereafter. In the absence of CMP-derived velocities, we assume a relative dielectric permittivity, ε_r, for water of 80 (Annan, 1992). Surface ice cover is ~0.2 m thick; therefore, our time-to-depth conversions assume a GPR velocity of 3.3×10^{-2} m ns^{-1} throughout. While ε_r can vary with temperature (e.g. Malmberg and Maryott (1956) measured $\varepsilon_r \approx 88$ at 0°C), the uncertainty in depth estimates is expected to be small and the difference in derived velocity, and therefore depth estimates, between ε_r values of 80 and 88 is < 5%. Hence, in the absence of lake water temperature measurements, we use $\varepsilon_r = 80$. We estimate the wavelength of the 25 MHz RTA wavelet to be 1.3 m; the ¼-wavelength criterion for vertical and (following migration) lateral resolution suggests that our limit of resolution is 0.3 m. Data processing steps, implemented in Sandmeier ReflexW© 7.5 software, are listed in Table 1.1. The data generally respond well to the imposed processing flow, although artefacts of normal moveout correction remain at early travel-times where the propagation path of GPR energy is comparable in length to the 6 m offset between the two antennas. Very few artefacts of migration remain; those that do are presumably caused by off-line scatter, and cannot be correctly migrated given the 2-D acquisition.

Table 4.1. Processing operations and parameters applied sequentially to profiles of GPR data.

Operation	**Parameters**
Dewow filter (removal of low-frequency component of trace)	Window length = 80 ns
Static correction (alignment of time-zero in traces)	All first-breaks synchronized to 20.6 ns (= 0.3 m/ns x 6.2 m)
Regularization of trace interval	Trace interpolation to 0.2 m
Normal moveout correction	Assumed velocity = 0.033 m/ns
Ormsby bandpass filter	Corner frequencies = 4-8-50-100 MHz
Constant velocity Kirchhoff migration	Migration aperture = 40 m Velocity = 0.033 m/ns
Median filter	Window = 3 traces x 3 samples
Amplitude gain	Gain function based on constant velocity geometrical spreading correction
Depth conversion	Constant velocity = 0.033 m/ns

By picking the first-break of lakebed reflections, we calculated bathymetry for each trace of the GPR dataset. This operation was straightforward in the deepest sections of the lake but was subject to greater uncertainty in shallower sections where the bed reflection was gradually more complex. Bed reflection characteristics are discussed in the Results section under “GPR Facies Classification”. In addition, the shallower areas are subject to distortions in our normal moveout correction (e.g. Figure 4.5, beginning of transect). Given the finite lateral resolution of the GPR wavelet, we picked bathymetry to be

deliberately smooth, and estimate that the uncertainty in the calculation of lake depth to be at maximum ±1 m.

The performance of the GPR depth conversion is assessed against the results of a separate sonar bathymetry point survey performed in December 2014 using a Hummingbird 385ci DualBeam™ sonar (Thompson et al., 2016). The grid spacing of sonar survey was ~20 m along track and 6-40 m between tracks (Figure 4.2), and results were spline interpolated with a shoreline polygon barrier in ESRI ArcMap to provide a map of lake bathymetry. However, because the sonar bathymetry survey was not conducted specifically for comparison with the GPR survey, the GPR survey lines do not directly overlap the sonar points. Thus, we expect there to be variability in the comparison and use this as a broad assessment of the GPR depth conversion, rather than an assessment of the superiority of methods. Sonar points located closer to the GPR profiles are likely to provide a better corroboration of the GPR data than those located at a greater distance. The source pulse of the echo-sounder blends frequencies of 85 and 200 kHz, which gives vertical and lateral resolution comparable to the GPR, assuming a sonic velocity of 1500 m s^{-1} in water. We therefore extracted interpolated sonar depth estimates along the radar transects to provide the necessary comparison between the two platforms.

Finally, we used GPR facies analysis to classify the lakebed from the processed GPR data. Facies analysis (Bristow, 1995, Ruffell et al., 2004) is a qualitative means of characterizing styles of reflectivity, thereby allowing the mapping of consistent features, which have similar reflection geometry. We applied this qualitative approach to classification, as a more quantitative analysis is not possible in the absence of CMP data.

Results

GPR bathymetry

In GPR transects from basin A (Figure 4.3; transects 1-4) and basin B (Figure 4.4), we interpret the first arrival after a transparent section of data to be the reflection from the lakebed. The maximum two-way travel-time of the lakebed reflection is ~ 1300 ns, corresponding to a maximum lake depth of ~ 21 m (Figure 4.3, transect 1). In Basin A, the lakebed geometry appears generally bowl-shaped, relatively flat in the deeper areas, sloping up to the shoreline at an angle of 20-30° relative to the lake surface. A prominent hummock occurs in the center of the basin in transects 1 and 3 (Figure 4.3). The hummock is inferred to be ~60 m wide at its base, with a topographic high point at a depth of ~ 9 m, ~ 16 m shallower than the surrounding lakebed. Transect 2 (Figure 4.3) also shows evidence of the hummock, but the shoreward slope is not well defined. In Basin B, lakebed geometry shows a gradual deepening from 1 m in the south to 6 m in the north over a distance of ~120 m, followed by rapid deepening to 15 m (Figure 4.4). The lake shallows again to depths of 3-7 m between distance of 220 m and 260 m along track. This section of the lake appears to have a more undulating bathymetry.

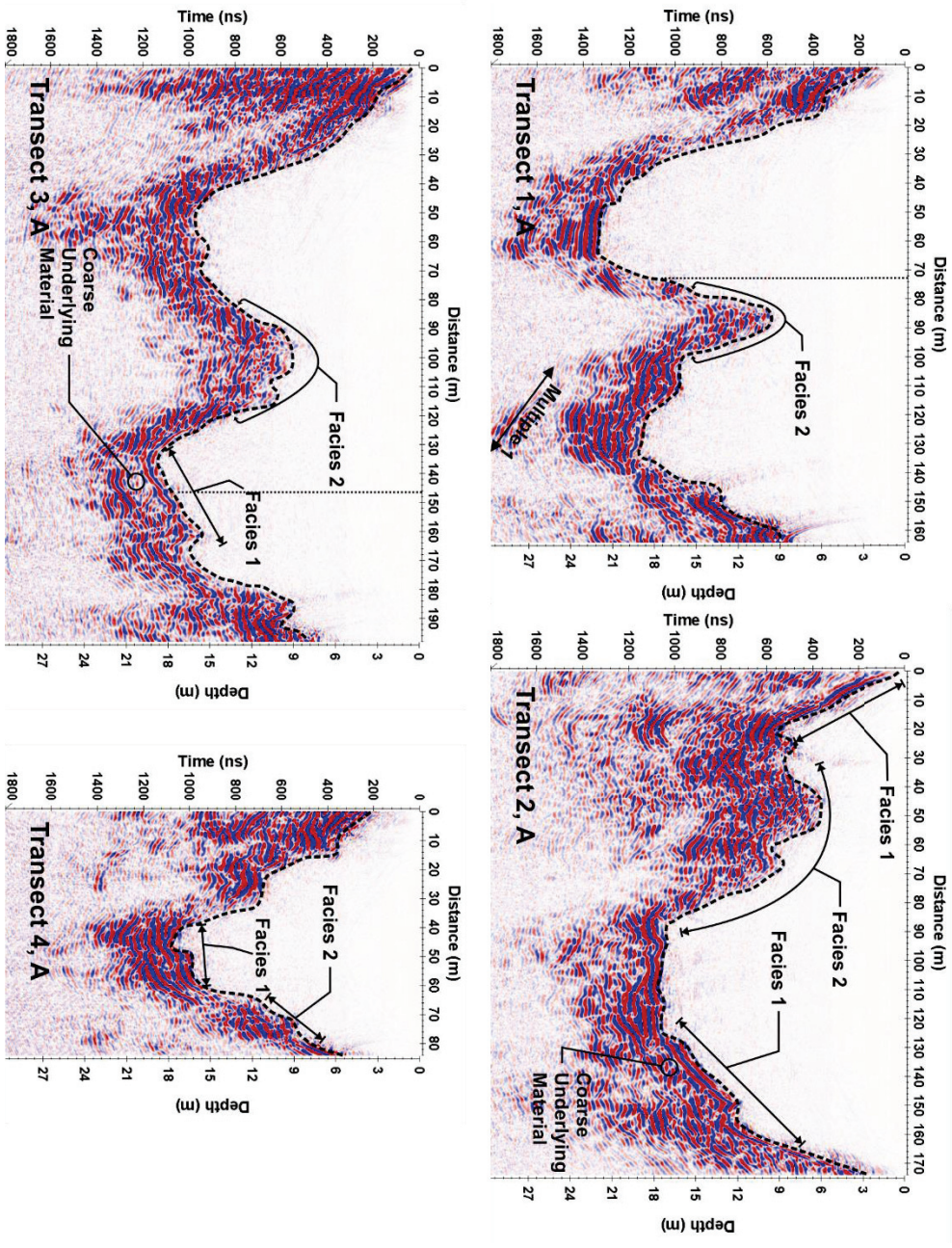

Figure 4.3: GPR transects 1-4, (basin A), post processed with dashed black line indicating lakebed and labeled multiples and locations of inferred facies. Vertical dotted line indicates crossing point of transects 1 and 3. Vertical exaggeration is roughly 5x. Direction of travel is from left to right.

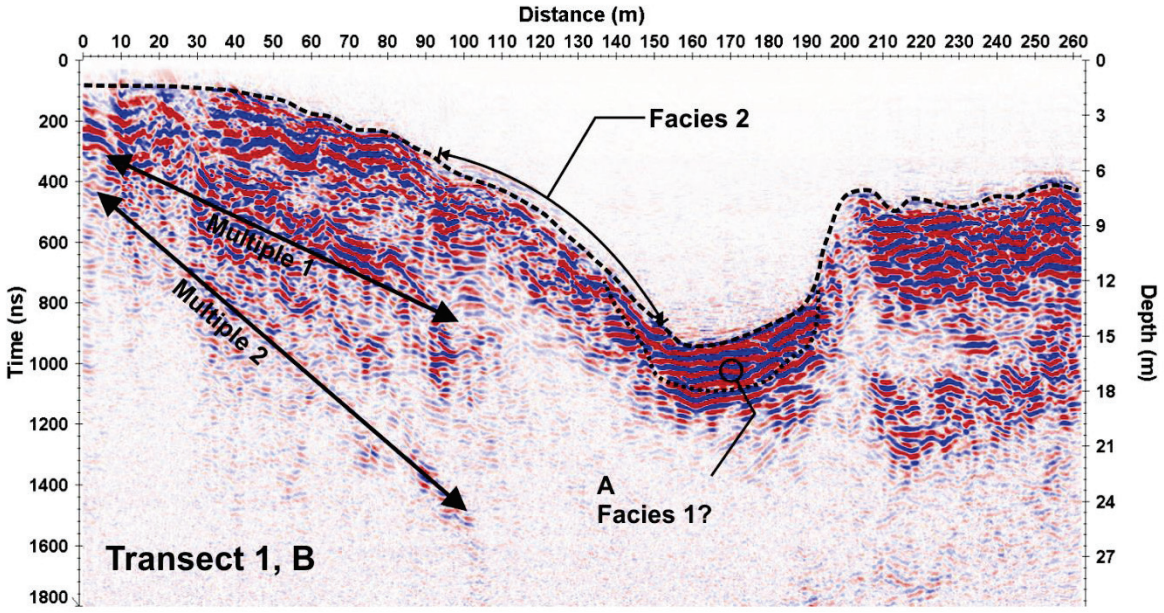

Figure 4.4: GPR Transect 1, (basin B), post processed with dashed black line indicating lakebed and labeled multiples and locations of inferred facies. Vertical exaggeration is roughly 5x. Direction of travel is from left to right.

Comparison with sonar data

Only six of the sonar survey points are located within a distance of ≤1 m from the GPR transects. The mean difference between these sonar point-depth measurements and the closest measured GPR-derived depths was 1.4m (Figure 4.5a). Differences between the GPR-derived depths and the interpolated sonar depths were generally larger, with positive differences ranging from 2.3 m-7.7 m and negative differences ranging from -1.1 m- -6.0 m (Figure 4.5b). Transects 2A, 4A and 1B, which roughly follow grid lines of the sonar measurements, all have differences less than ±5m with mean differences of 1.2 and standard deviation of ±1.2 m, -0.7 and standard deviation of ±1.7 m and -0.8 and standard deviation of ±1.4 m respectively (Figure 4.5b). Whereas, transects 1A and 3A, running oblique to sonar measurement grid, all have differences greater than 5 m and less than -4.3 m with means of -0.4 m, standard deviation of ±3.0 m, and 1.2 m, standard deviation

of ±3.8 m respectively (Figure 4.5b). The mean difference of all transects is 0.1 m, standard deviation of ±2.5 m.

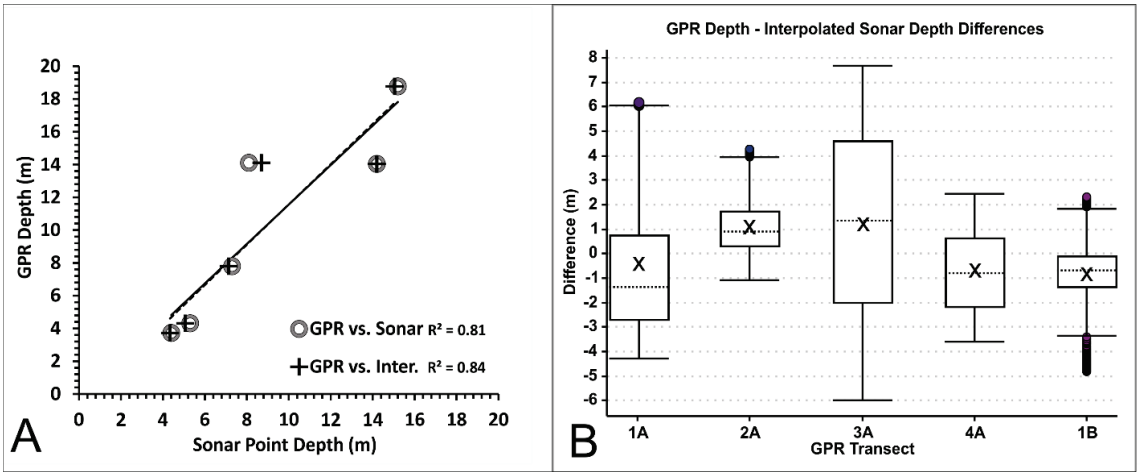

Figure 4.5: GPR depths compared to sonar point depths and interpolated sonar depth (A). Boxplot of differences between GPR depths and interpolated sonar depth (B). Transects 2A, 4A and 1B display a much smaller interquartile range indicating better agreement between depths, with averages from 1.3 to -1.4m (x).

GPR facies classification

Sediment appears to cover the entire surveyed parts of the lakebeds. Two facies can be distinguished based on the characteristics of the lakebed reflectors (Figure 4.6). Facies 1 shows coherent, sub horizontal reflectivity, with parallel events either side of incoherent responses (Figure 4.6a). Facies 1 is present in the deeper areas of both lake basins and around the lake flanks (Figure 4.3 and 4). Facies 2 shows low-amplitude, chaotic reflectivity, characteristic of structural complexity (Figure 4.6b). Facies 2 is most often associated with features such as the hummock in the center of basin A (Figure 4.3).

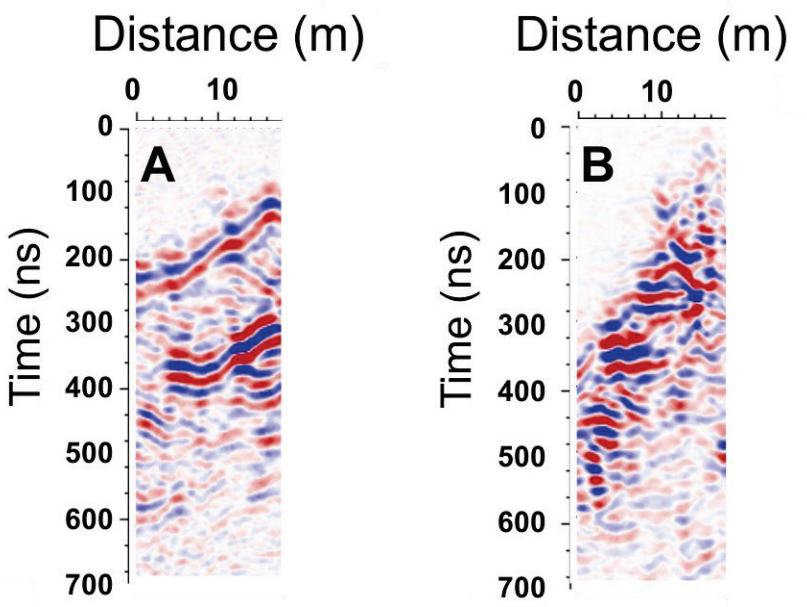

Figure 4.6: Subsets of distinct radar facies. (A) Coherent, sub-horizontal reflectivity, often comprising subparallel sets of reflections. (B) Typical low-amplitude and chaotic reflectivity, prone to migration noise suggesting structural complexity. Both facies plotted with equivalent amplitude scales.

Interpretation and discussion

GPR analysis and interpretation

Differences in point depth measurements made using GPR and sonar are smallest where distances between the measurements were smallest (Figure 4.5a). Similarity of depth measurements results from the GPR and sonar having similar un-migrated horizontal resolutions, with a mean difference of 0.52 m over the depth ranges in our study. Differences between GPR depths and interpolated sonar depths are likewise smallest along transects that have the largest number of proximate sonar point measurements, as well as where lake bathymetry is relatively flat. For example, transects 2A, 4A and 1B appear very similar to the interpolated sonar depths (Figure 4.7).

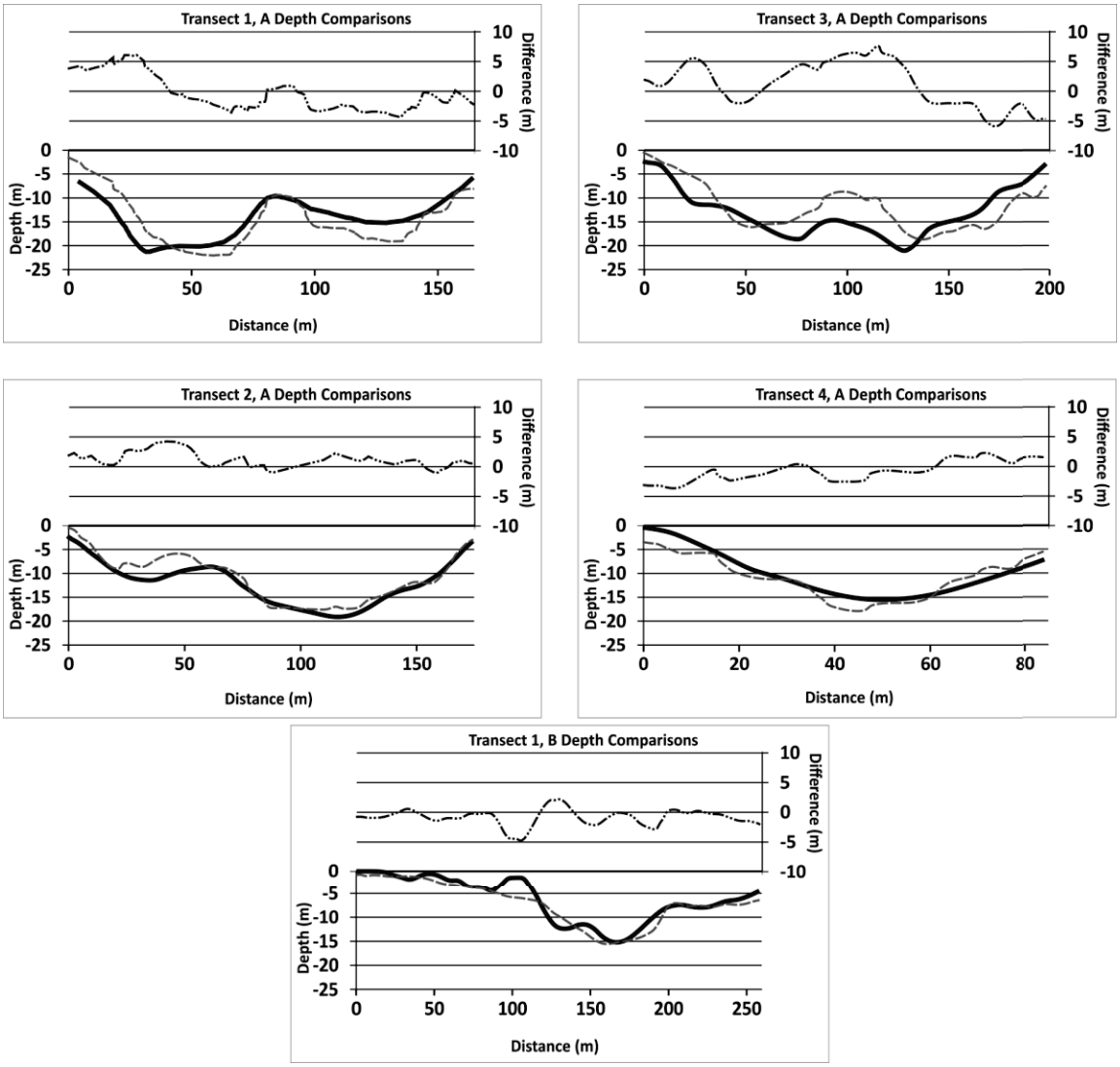

Figure 4.7: Comparison of GPR depths (gray dashed) and interpolated sonar depths (solid black), with differences (top dash-dot-dot). Note the areas of large difference in transects 1A and 3A, corresponding to areas where there is little overlap between the methods.

All three transects have a gradually changing bathymetry, with only a few regions of rapid change. GPR traces for these transects are located a mean distance of 8.4±2.8 m, 5.3±1.7 m and 7.2±3.5 m away from their nearest sonar point measurements respectively (Figure 4.8). The maximum and minimum distances for transects 2A and 4A are 12.9 –

2.6 m and 8.9 – 1.6 m respectively. Transect 1B, however, has a much larger range of distances with a maximum and minimum of 17.1 – 0.9 m. Transects 1A and 3A have similar mean distances to sonar measurements as 2A, yet overall there is considerably more variation in each, with maximum distances at 20.4 m and 20 m respectively (Figure 4.8).

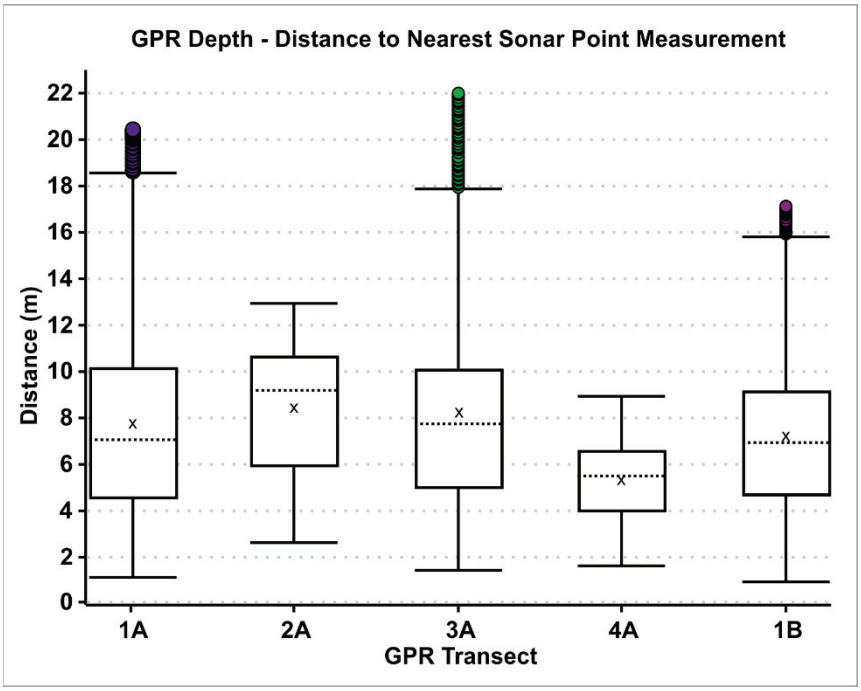

Figure 4.8: Boxplot of distance from GPR trace to nearest sonar point measurement.

The two sets of depth measurements become more divergent where lake bathymetry is more complex (e.g. Figure 4.7, transect 3A, 50-150 m) likely as the result of sparse point data to constrain interpolation. For example, the greatest differences between depth measurements occur in transects 1A and 3A, where point data are spaced further than 13 m apart (e.g. Figure 4.2 red ellipse) and interpolation errors are likely to be the greatest.

Similarly, transect 1B shows small variation in differences, yet has numerous outliers (Figure 4.5b) that correspond to large distances from sonar point measurements (Figure 4.8). These locations of larger difference are easily identifiable in Figure 4.7 and seen as the central area of basin B where data are again sparse. Small differences in depth measurements using the two techniques indicate GPR provides depth information that is roughly equivalent to sonar, but GPR has the added advantages of rapid data acquisition when collected on frozen lake surfaces and provides information about lakebed composition and structure.

Facies

Facies 1 is consistent with a more uniform scattering in which discontinuities are much smaller than the radar wavelength (i.e. 1.3 m). We interpret these sub-parallel sequences of reflectivity as layers of fine sediment, similar to the bedded sand deposits exposed around some lake margins (Figure 4.9). By contrast, Facies 2 is consistent with a chaotically scattering lakebed where discontinuities are on a spatial scale comparable with the radar wavelength (i.e., 1.3 m). We interpret Facies 2 as areas of the lakebed covered with coarse debris, including boulders and large clasts, similar to the widespread blocky diamict debris cover exposed on the glacier surface (Figure 4.9). Our facies classifications and identification agree well with the mapped distribution of bottom surface types found by Horodyskyj (2015), and is also consistent with the observation that bathymetry associated with Facies 1 is likely to have less abrupt changes than in areas where Facies 2 is found.

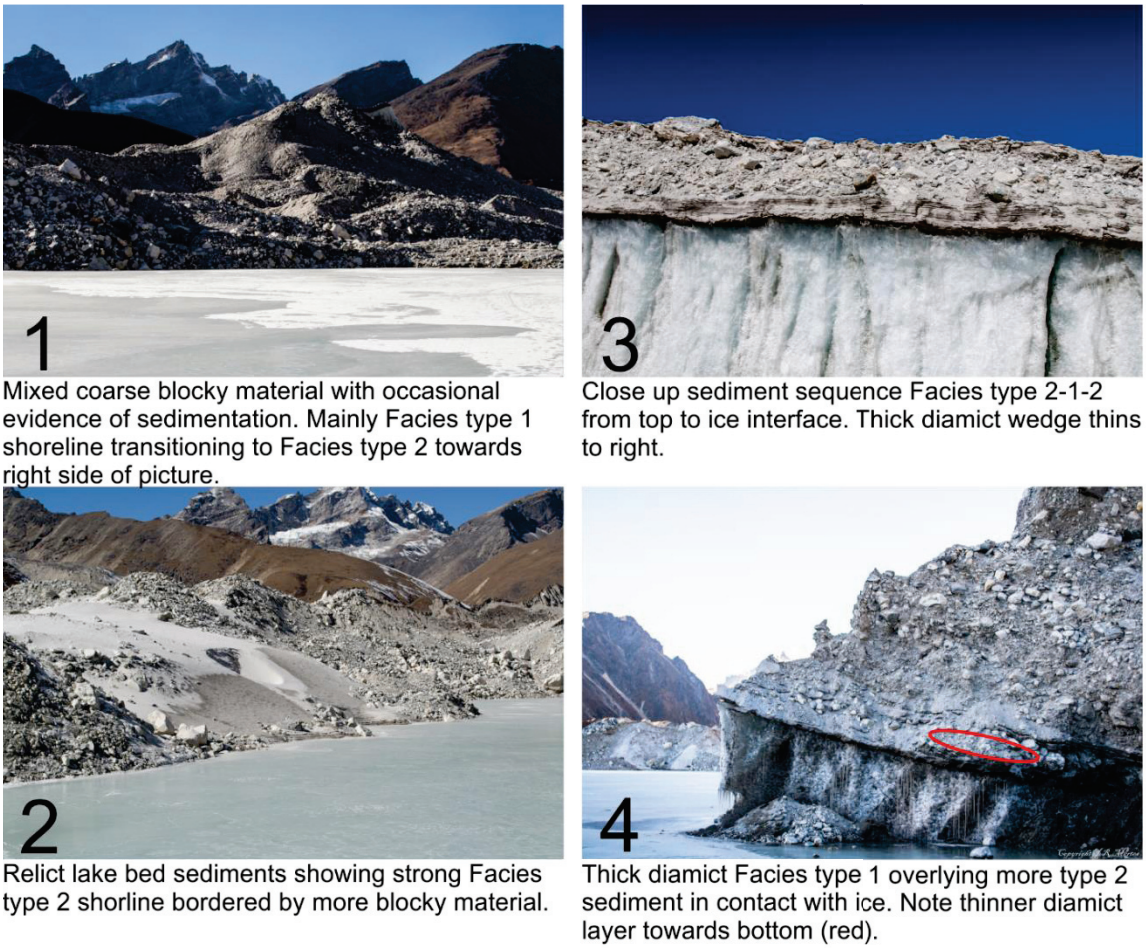

Figure 4.9: Examples of exposed shoreline facies marked in Figure 4.2 as white hexagons.

The lack of exposed ice in our lakebed surveys suggests that any bare ice in lake basins is rapidly covered by sediments. Facies sequences, however, suggest that bare ice is exposed at lakebeds at least transiently. For example, if Facies 2 is in contact with ice on the lakebed, it cannot be known if the sediments were deposited as part of a mass wasting event onto a bare ice bed following lake formation or if they reflect an original debris-covered ice surface that was submerged following surface downwasting. In contrast,

because Facies 1 suggests deposition by settling of finer grained materials, the superposition of Facies 1 with glacier ice at the lake bed strongly suggests the lake bed consisted of bare ice likely present prior to Facies 1 deposition (Figures 4.9 & 4.10). Facies relationships suggest that up 20% of our survey lines were initially composed of bare ice, but were later covered by Facies 1 sediments.

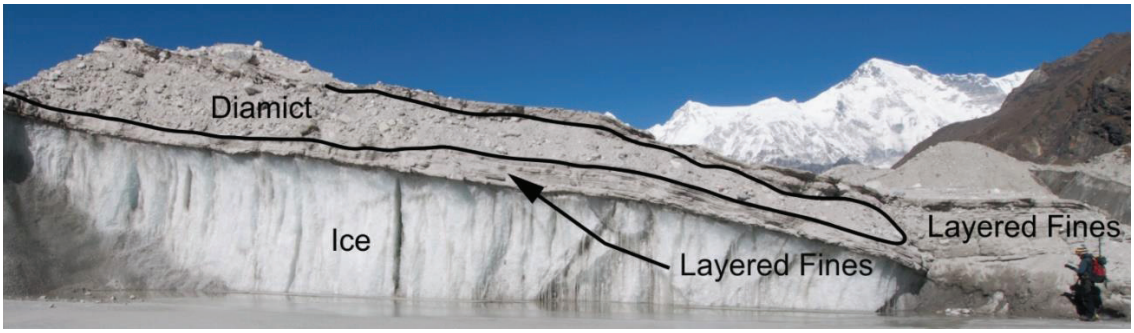

Figure 4.10: Overview of exposed large diamict wedge deposited between layered fines indicating debris redistribution onto relatively flat, sediment covered lakebed, followed by more fine deposition (Figure 4.2; 4.9 example 3).

Overlapping facies relationships demonstrate that the dominant sediment/debris delivery mechanisms to lakes can switch from mass wasting, toppling from ice cliffs and/or sliding from moraine ridges to settling of suspended fines, creating a transition from Facies 2 to Facies 1. For example, the upward transition from Facies 2 to Facies 1 (Figure 4.3) between 130 and 160 m in transect 3A, and between 120 to 160 m in transect 2A, indicate that the dominant sediment delivery mechanism switched from mass wasting to deposition of fines. Such a transition would be expected to occur as lakes expanded. Sediments would initially be deposited via mass wasting occurring as ice cliffs retreated around the lakeshore, causing small landslides of sediments into lakes. As lake area

expanded, and sources of sliding debris move further away, sedimentation changes to settling of fines.

Transitions from Facies 1 to Facies 2 require a different explanation. We did not find distinct evidence for this transition in our GPR data, but it was observed in sediment packages associated with a drained lake basin ~60 m north of lake basin A (Figure 4.2 location yellow star, Figure 4.9, 3). Based on freely available declassified KH-9 and Landsat imagery of the AOI, it can be seen that between 1964 and 1967 a perched lake and backwasting ice cliff located ~60-70 m north in 1964 was expanding and most likely intercepted this location. Throughout the mid-late 1970s the area appears to be submerged but towards the beginning of the early 1980s, it is once again exposed. As Spillway Lake began to form and expand, this location was once again submerged, sometime in 2005-2006, and subsequently was re-exposed in the 10/15/2009 Landsat image. A stratigraphic sequence of fine-grained sediments deposited near- parallel with a bare ice surface was exposed over an ice cliff at the lakeshore, indicating deposition onto submerged bare glacier ice. There is an abrupt change from fine sediment to a coarse-grained diamict wedge 1.5 m thick, which extends part way across the underlying fines. Fine-grained material has also been deposited on top of the diamict, supporting the characterization of this sequence in the lake environment, and was the result of a subaqueous debris slumping event (Figure 4.10).

A conceptual model of supraglacial lake evolution for debris-covered glaciers

Here we present a conceptual model of supraglacial lake evolution, the basis of which is a consolidation of the literature investigating lake formation and expansion, with the

addition of the facies relationships observed in our study. Facies transitions suggest that the spatial distribution of debris and depositional processes change as supraglacial lakes grow. These changes reflect varying environmental factors such as proximity to ice cliffs and debris-covered slopes, initiation of calving, interception with englacial conduits or voids and subaqueous and subaerial mass movement events. These relationships provide the addition of the evolving debris environment to the model of an expanding supraglacial lake, highlighting the changing debris-related constraints and feedbacks as a supraglacial lake evolves.

During early stages of lake growth, water accumulates in small, isolated lake basins that are perched above base level and not connected to supraglacial streams or englacial conduits (Benn et al., 2001) (Figure 4.11, A). The surrounding shoreline likely consists primarily of low gradient, stable debris-covered slopes. Prior to infilling, the lakebed is likely composed of similar diamict as is found above the lake surface (Facies 2). During lake infilling, sedimentation rates in the lake would be low, because sediments would be sourced primarily from windblown dusts or fine-grained materials leached from the surrounding diamict by percolating meltwaters (Facies 1). Consequently, Facies 1 is deposited over Facies 2.

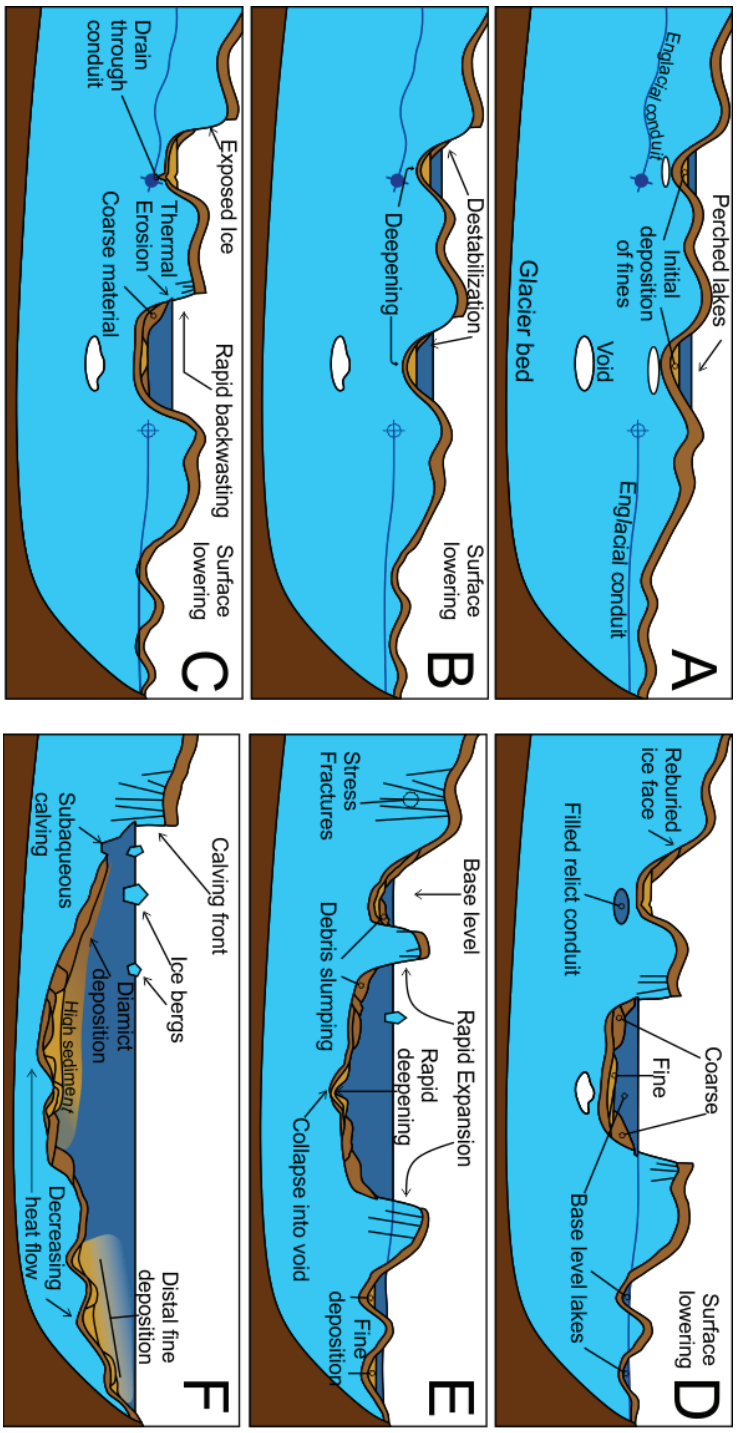

Figure 4.11: A conceptual model of supraglacial lake evolution on debris covered glaciers with additional changes in sediment depositional processes affecting lakebed spatial debris distribution. (A) Isolated perched lakes, not connected to supraglacial

streams or englacial conduits. (B) As perched lakes expand, debris slumping becomes more likely. (C) Some perched lakes may drain due to intersection with englacial conduits, potentially evacuating some lakebed sediment. (D) Ice cliff expansion and lake bed deepening lead to the intersection of the largest lake with a base level conduit. (E) Continued expansion of lakes in the area cause all to connect either through surface drainage networks or near surface conduits. (F) Lake expansion and coalescing leads to the formation of a single base-level moraine dammed lake.

Expansion of small, perched lake basins occurs by slow melting of subaqueous ice around the lake margins, or possibly collapse into englacial voids, which steepens the lakebed slopes, eventually forming steep bare ice faces or ice cliffs (Benn et al., 2001, Röhl, 2008, Thompson et al., 2012) (Figure 4.11, B). Bare ice faces and ice cliffs increase rates of lake expansion and trigger a change in deposition. Bare ice faces often have a thin coating of dark, wet mud which reduces the surface albedo and increases absorption of solar radiation, creating localized hot spots of enhanced melting (Benn et al., 2001). Ice cliffs can lead to rapid lake expansion through calving, as thermo-erosional notching at the waterline leads to fracturing (Benn et al., 2001, Röhl, 2008, Miles et al., 2016). Lake expansion by melt retreat of steep, bare ice faces and calving would cause Facies 2 type sediments to be deposited by slumping around the expanding lake margin, with deposition of fine-grained Facies 1 sediments in the central deeper areas of the lake.

Sediment deposition can force a positive feedback on lake expansion. Slumping provides a constant influx of diamict, which helps keep turbidity high. This increase in turbidity can decrease lake surface albedo, thereby increasing absorbed solar radiation, which keeps surface temperatures high. Conversely, a negative feedback results from deposited fine sediments (Facies 1) on the lakebed insulating underlying ice from melt, decreasing

bottom water cooling. These effects combine to promote melting along lake perimeters, thereby enhancing areal expansion.

Perched lake expansion and sedimentation is halted when lakes intercept englacial conduits or sediment filled crevasse traces and rapidly drain (Figure 4.11, C) (Benn et al., 2001, Wessels et al., 2002, Gulley and Benn, 2007, Röhl, 2008, Benn et al., 2009, Benn et al., 2012, Thompson et al., 2012). While conduits temporarily drain small perched lakes, they play an important role in glacier surface lowering and the development of larger lakes (Kirkbride, 1993, Immerzeel et al., 2014, Thompson et al., 2016). Conduit collapse creates new depressions with new bare ice faces where enhanced melting can continue and lakes may eventually be recharged with water from up glacier. In addition, water transported from a lake drainage event loses heat to conduit walls, thereby adding to mass loss through internal ablation (Kirkbride, 1993, Benn et al., 2012, Miles et al., 2016, Thompson et al., 2016) and promotes future collapse by widening conduits (Gulley and Benn, 2007). The presence of Facies 1 in direct contact with glacier ice may be due to a collapse and drainage event that flushed lakebed sediments out of the lake basin, leaving a bare ice surface exposed to melt and sedimentation.

Cycles of lake expansion, drainage by conduits and collapse, and refilling allow smaller, isolated lakes to coalesce behind the terminal moraine to form a large, moraine dammed lake; examples include Imja Tsho, or Tsho Rolpa (Nepal Himalaya) (Figure 4.11, D-F). While the physical processes driving the change from a series of perched lakes, like Spillway Lake reported here, to a large moraine dammed lake remain poorly understood, it is thought that coalescence of small lakes into a larger one triggers rapid lake expansion

through subaerial slab calving, and increased subaqueous waterline melting (Kirkbride, 1993, Sakai et al., 2009) (Figure 4.11, E). While slab calving of exposed ice cliffs can cause rapid lake expansion, deposition of subaerial debris located along the top of ice cliffs onto the lakebed can force a negative feedback on lake expansion (Figure 4.11, E). Accumulation of debris at the base of ice cliffs has been observed to separate the ice cliff from the lake, halting calving and lake expansion at that location (Thompson et al., 2016).

Lake-bed disintegration has been proposed as a key trigger to initiation of full front calving and rapid retreat (Kirkbride, 1993). However, more recent work suggests rapid lake expansion by calving does not require the lake to deepen to the glacier bed (Figure 4.11, F). Robertson et al. (2012) observed subaqueous debris layers between 5-10 m in thickness at the calving margins of Mueller, Hooker and Tasman glaciers. Using a CHIRP sonar, they were able to visualize the calving margin where they found a debris-covered sloping ice foot projecting into the lake at an angle of about 40º, indicating the calving front did not reach to the glacier bed (Robertson et al., 2012). Similarly, a GPR study at Imja Tsho, found glacier ice just up-glacier from the calving front was ~80 m deeper than the deepest point in the lake, indicating that glacier ice was present below the lake bed (Somos-Valenzuela et al., 2014). Despite debris cover, data from Imja Tsho indicates that some lakebed deepening still occurs. Taking into consideration that the lake level has been stable for the past decade, at roughly 5010 m a.s.l., the mean rate of deepening at Imja Tsho (2002-2012) was roughly 0.86 my^{-1}, with maximum depths increasing from 98 m to 116 m (Somos-Valenzuela et al., 2014). Deepening was faster

near the calving front and slower nearer the terminus. Some of this deepening may be due to sub-debris melting, but some is due to subaqueous calving (Somos-Valenzuela et al., 2013, Somos-Valenzuela et al., 2014).

In summary, using the GPR facies relationships identified in our surveys with field observations, we were able to infer feedbacks between processes controlling supraglacial lake growth and sediment deposition. We have developed a conceptual model of how dominant depositional processes can change as lakes evolve from perched lakes to multi-basin base-level lakes and finally onto large moraine-dammed lakes. Throughout lake evolution, processes such as shoreline steepening, lakebed collapse into voids and conduit interception, subaerial and subaqueous calving and rapid areal expansion alter the spatial distribution and makeup of lakebed debris and sediments which, in turn, can control rates of deepening by enhancing or diminishing heat conduction to the underlying ice.

Conclusion

The results of our GPR surveys not only provide high resolution bathymetric information (beneath the survey lines) allowing us to map the morphology of the lake bed but the additional facies interpretation provided a detailed lakebed debris characterization. This work demonstrates the applicability of GPR as a tool for supraglacial lake investigation and monitoring. We found that lake depth surveys can be completed rapidly with GPR when lake surfaces are frozen. While studies of supraglacial lakes have traditionally relied primarily on sonar, we showed that GPR provides depth information that is equivalent to sonar, with added information about sediment types on lakebeds. Facies

analysis highlights the additional information that can be derived from lakebed surveys using GPR. Sonar data can provide some information about bottom composition, such as surface hardness and texture (Horodyskyj, 2015) but cannot provide the facies information as reported here. Selecting GPR units with CMP survey capability would further expand the utility of GPR, as CMP surveys can provide measurement of the velocity through the debris, allowing one to calculate sediment layer thicknesses, an important parameter for modelling subaqueous heat flux and lake deepening. Further, conducting paired CMP surveys would allow for debris thicknesses to be mapped by determining the material velocity of different facies types, ultimately leading to a much more complete understanding of the spatial distribution, quantity and makeup of lakebed debris.

Future investigations should aim to perform repeat 3-D GPR surveys, which will allow not only detailed changes in lake bathymetry and bed morphology to be measured but also changes in debris distribution. Knowledge such as this is of paramount importance for modelling potential subaqueous lake expansion and understanding the specific thresholds that trigger rapid growth from supraglacial lakes to moraine-dammed lake.

Acknowledgements

Jordan R. Mertes acknowledges funding from Michigan Technological University and The Michigan Technological University 2016 Fall Finishing Fellowship. Sarah S. Thompson acknowledges funding from the University Centre in Svalbard (UNIS) and the European Commission FP7-MC-IEF. We thank Rijan Bhakta Kayastha for assistance in obtaining research permits, Endra Rai Bahing, Ani Bhattarai and Sujan Bhattarai for

logistical support and Lhakpa Nuru Sherpa and the staff at the Cho La Pass Resort for hospitality, logistical support and assistance with fieldwork. We give a huge dhanyabad to Passang Wes for his hard work, without which much of the fieldwork would have been exhausting. We would also like to thank the editor and two anonymous reviewers for constructive reviews that helped us to better organize this manuscript and see it through to fruition.

References

Adhikary S, Nakawo M, Seko K, Shakya B. 2000. Dust influence on the melting process of glacier ice: experimental results from Lirung Glacier, Nepal Himalayas. IAHS PUBLICATION: 43-52

Annan AP, 1992. Ground penetration radar workshop notes. Sensors and Software Inc., Mississauga. p 130, internal report

Annan AP. 2004. Ground penetrating radar principles, procedures and applications

Arcone SA, Finnegan DC, Liu L. 2006. Target interaction with stratigraphy beneath shallow, frozen lakes: Quarter-wave resonances within GPR profiles. Geophysics **71**: K119-K131. DOI: 10.1190/1.2358404

Bajracharya SR, Mool P. 2010. Glaciers, glacial lakes and glacial lake outburst floods in the Mount Everest region, Nepal. Annals of Glaciology **50**: 81-86. DOI: 10.3189/172756410790595895

Banks WSL, Johnson CD, 2011. Collection, processing, and interpretation of ground-penetrating radar data to determine sediment thickness at selected locations in Deep Creek Lake, Garrett County, Maryland, 2007. US Geological Survey

Benn D, Gulley J, Luckman A, Adamek A, Glowacki PS. 2009. Englacial drainage systems formed by hydrologically driven crevasse propagation. Journal of Glaciology **55**: 513-523. DOI: 10.3189/002214309788816669

Benn DI, Bolch T, Hands K, Gulley J, Luckman A, Nicholson LI, Quincey D, Thompson S, Toumi R, Wiseman S. 2012. Response of debris-covered glaciers in the Mount Everest region to recent warming, and implications for outburst flood hazards. Earth-Science Reviews **114**: 156-174. DOI: 10.1016/j.earscirev.2012.03.008

Benn DI, Wiseman S, Hands KA. 2001. Growth and drainage of supraglacial lakes on debrismantled Ngozumpa Glacier, Khumbu Himal, Nepal. Journal of Glaciology **47**: 626-638. DOI: 10.3189/172756501781831729

Benn DI, Wiseman S, Warren CR. 2000. Rapid growth of a supraglacial lake, Ngozumpa Glacier, Khumbu Himal, Nepal. IAHS PUBLICATION: 177-186

Bolch T, Buchroithner M, Peters J, Baessler M, Bajracharya S. 2008. Identification of glacier motion and potentially dangerous glacial lakes in the Mt. Everest region/Nepal using spaceborne imagery. Natural Hazards and Earth System Science **8**: 1329-1340. DOI: 10.5194/nhess-8-1329-2008

Bristow C. 1995. Facies analysis in the Lower Greensand using ground-penetrating radar. Journal of the Geological Society **152**: 591-598. DOI: 10.1144/gsjgs.152.4.0591

Buri P, Pellicciotti F, Steiner JF, Miles ES, Immerzeel WW. 2015. A grid-based model of backwasting of supraglacial ice cliffs on debris-covered glaciers. Annals of Glaciology:

Chikita K, Jha J, Yamada T. 1999. Hydrodynamics of a supraglacial lake and its effect on the basin expansion: Tsho Rolpa, Rolwaling Valley, Nepal Himalaya. Arctic, Antarctic, and Alpine Research: 58-70. DOI: 10.2307/1552623

Chikita K, Jha J, Yamada T. 2001. Sedimentary effects on the expansion of a Himalayan supraglacial lake. Global and Planetary Change **28**: 23-34. DOI: 10.1016/S0921-8181(00)00062-X

Fitzpatrick AAW, Hubbard AL, Box JE, Quincey DJ, Van As D, Mikkelsen APB, Doyle SH, Dow CF, Hasholt B, Jones GA. 2014. A decade (2002–2012) of supraglacial lake volume estimates across Russell Glacier, West Greenland. The Cryosphere **8**: 107-121. DOI: 10.5194/tc-8-107-2014

Fujita K, Sakai A, Nuimura T, Yamaguchi S, Sharma RR. 2009. Recent changes in Imja Glacial Lake and its damming moraine in the Nepal Himalaya revealed by in situ surveys and multi-temporal ASTER imagery. Environmental Research Letters **4**: 045205. DOI: 10.1088/1748-9326/4/4/045205

Gardelle J, Arnaud Y, Berthier E. 2011. Contrasted evolution of glacial lakes along the Hindu Kush Himalaya mountain range between 1990 and 2009. Global and Planetary Change **75**: 47-55. DOI: 727 10.1016/j.gloplacha.2010.10.003

Gardelle J, Berthier E, Arnaud Y. 2012. Slight mass gain of Karakoram glaciers in the early twenty-first century. Nature Geoscience **5**: 322-325. DOI: 10.1038/ngeo1450

Gulley J, Benn DI. 2007. Structural control of englacial drainage systems in Himalayan debris-covered glaciers. Journal of Glaciology **53**: 399-412. DOI: 10.3189/002214307783258378

Haeni F, McKeegan DK, Capron DR, 1987. Ground-penetrating radar study of the thickness and extent of sediments beneath Silver Lake, Berlin and Meriden, Connecticut. In *Water-Resources Investigations Report*. US Geological Survey, WRD

Hands K. 2004. Downwasting and supraglacial pond evolution on the debris-mantled Ngozumpa Glacier, Khumbu Himal, Nepal. University of St Andrews. PHD. http://research-repository.st-andrews.ac.uk/. St. Andrews

Horodyskyj UN. 2015. Contributing factors to ice mass loss on Himalayan debris-covered glaciers. University of Colorado at Boulder. Department of Geological Sciences. Ph.D. 1321773196. http://search.proquest.com/docview/1690497550. UMI Disseratation Publishing

Immerzeel W, Kraaijenbrink P, Shea J, Shrestha A, Pellicciotti F, Bierkens M, De Jong S. 2014. High-resolution monitoring of Himalayan glacier dynamics using unmanned aerial vehicles. Remote Sensing of Environment **150**: 93-103. DOI: 10.1016/j.rse.2014.04.025

Kääb A, Berthier E, Nuth C, Gardelle J, Arnaud Y. 2012. Contrasting patterns of early twenty-first-century glacier mass change in the Himalayas. Nature **488**: 495-498. DOI: 10.1038/nature11324

Kadota T. 1994. Report for the field investigation on the Tsho Rolpa glacier lake, Rolwaling Valley, February 1993–June 1994. WECS Report N **551.489 KAD**:

Kenny A, Cato I, Desprez M, Fader G, Schüttenhelm R, Side J. 2003. An overview of seabed-mapping technologies in the context of marine habitat classification. ICES Journal of Marine Science: Journal du Conseil **60**: 411-418. DOI: 10.1016/S1054-3139(03)00006-7

Kirkbride MP. 1993. The temporal significance of transitions from melting to calving termini at glaciers in the central Southern Alps of New Zealand. The Holocene **3**: 232-240. DOI: 10.1177/095968369300300305

Kirkbride MP, Warren CR. 1997. Calving processes at a grounded ice cliff. Annals of Glaciology **24**: 116-121

Komori J. 2008. Recent expansions of glacial lakes in the Bhutan Himalayas. Quaternary International **184**: 177-186. DOI: 10.1016/j.quaint.2007.09.012
Liu Q, Mayer C, Liu S. 2015. Distribution and interannual variability of supraglacial lakes on debris-covered glaciers in the Khan Tengri-Tumor Mountains. Central Asia. Environ Res Lett **10**: 014014. DOI: 10.5194/tcd-7-4545-2013
Malmberg C, Maryott A. 1956. Dielectric Constant of Water from 0^0 to 1000^0 C. Journal of Research of the National Bureau of Standards **56**: 1-8. DOI: 10.6028/jres.056.001
Miles ES, Pellicciotti F, Willis IC, Steiner JF, Buri P, Arnold NS. 2016. Refined energy-balance modelling of a supraglacial pond, Langtang Khola, Nepal. Annals of Glaciology **57**: 29. DOI: 10.3189/2016aog71a421
Mool P. 1995. Glacier lake outburst floods in Nepal. Journal of Nepal Geological Society **11**: 273-280
Moorman BJ, Michel FA. 1997. Bathymetric mapping and sub-bottom profiling through lake ice with ground-penetrating radar. Journal of Paleolimnology **18**: 61-73. DOI: 10.1023/A:1007920816271
Nakawo M, Rana B. 1999. Estimate of Ablation Rate of Glacier Ice under a Supraglacial Debris Layer. Geografiska Annaler: Series A, Physical Geography **81**: 695-701. DOI: 10.1111/1468-0459.00097
Nicholson L, Benn DI. 2006. Calculating ice melt beneath a debris layer using meteorological data. Journal of Glaciology **52**: 463-470. DOI: 10.3189/172756506781828584
Nicholson L, Benn DI. 2012. Properties of natural supraglacial debris in relation to modelling sub-debris ice ablation. Earth Surface Processes and Landforms. DOI: 10.1002/esp.3299
Østrem G. 1959. Ice melting under a thin layer of moraine, and the existence of ice cores in moraine ridges. Geografiska Annaler **41**: 228-230
Quincey DJ, Luckman A, Benn D. 2009. Quantification of Everest region glacier velocities between 1992 and 2002, using satellite radar interferometry and feature tracking. Journal of Glaciology **55**: 596-606. DOI: 10.3189/002214309789470987
Quincey DJ, Richardson SD, Luckman A, Lucas RM, Reynolds JM, Hambrey MJ, Glasser NF. 2007. Early recognition of glacial lake hazards in the Himalaya using remote sensing datasets. Global and Planetary Change **56**: 137-152. DOI: 10.1016/j.gloplacha.2006.07.013
Reid T, Brock B. 2014. Assessing ice-cliff backwasting and its contribution to total ablation of debris-covered Miage glacier, Mont Blanc massif, Italy. Journal of Glaciology **60**: 3. DOI: 10.3189/2014JoG13J045
Reid TD, Brock BW. 2010. An energy-balance model for debris-covered glaciers including heat conduction through the debris layer. Journal of Glaciology **56**: 903-916. DOI: 10.3189/002214310794457218
Reynolds JM. 2000. On the formation of supraglacial lakes on debris-covered glaciers. IAHS PUBLICATION: 153-164
Reynolds JM. 2011. An introduction to applied and environmental geophysics. John Wiley & Sons

Reznichenko N, Davies T, Shulmeister J, McSaveney M. 2010. Effects of debris on ice-surface melting rates: an experimental study. Journal of Glaciology **56**: 384-394. DOI: 10.3189/002214310792447725
Robertson CM, Benn DI, Brook MS, Fuller IC, Holt KA. 2012. Subaqueous calving margin morphology at Mueller, Hooker and Tasman glaciers in Aoraki/Mount Cook National Park, New Zealand. Journal of Glaciology **58**: 1037-1046. DOI: 10.3189/2012JoG12J048
Röhl K. 2008. Characteristics and evolution of supraglacial ponds on debris-covered Tasman Glacier, New Zealand. Journal of Glaciology **54**: 867-880. DOI: 10.3189/002214308787779861
Ruffell A, Geraghty L, Brown C, Barton K. 2004. Ground-penetrating radar facies as an aid to sequence stratigraphic analysis: application to the archaeology of Clonmacnoise Castle, Ireland. Archaeological Prospection **11**: 247-262. DOI: 10.1002/arp.240
Sakai A, Chikita K, Yamada T. 2000a. Expansion of a moraine-dammed glacial lake, Tsho Rolpa, in Rolwaling Himal, Nepal Himalaya. Limnology and Oceanography **45**: 1401-1408. DOI: 10.4319/lo.2000.45.6.1401
Sakai A, Fujita K. 2010. Formation conditions of supraglacial lakes on debris-covered glaciers in the Himalaya. Journal of Glaciology **56**: 177-181. DOI: 10.3189/002214310791190785
Sakai A, Fujita K, Yamada T. 2005. Expansion of the Imja Glacier Lake in the East Nepal Himalayas. In *Glacier Caves and Glacial Karst in High Mountains and Polar Regions*, Mavlyudov BR (ed). Institute of geography of the Russian Academy of Sciences: Moscow; 74-79
Sakai A, Nakawo M, Fujita K. 2002. Distribution Characteristics and Energy Balance of Ice Cliffs on Debris-Covered Glaciers, Nepal Himalaya. Arctic, Antarctic, and Alpine Research **34**: 12-19. DOI: 10.2307/1552503
Sakai A, Nishimura K, Kadota T, Takeuchi N. 2009. Onset of calving at supraglacial lakes on debris-covered glaciers of the Nepal Himalaya. Journal of Glaciology **55**: 909-917. DOI: 10.3189/002214309790152555
Sakai A, Takeuchi N, Fujita K, Nakawo M. 2000b. Role of supraglacial ponds in the ablation process of a debris-covered glacier in the Nepal Himalayas. IAHS PUBLICATION: 119-132
Sakai A, Yamada T, Fujita K, 2003. Volume change of Imja glacial lake in the Nepal Himalayas. In *Disaster Mitigation & Water Management*: Niigata, Japan
Sambuelli L, Bava S. 2012. Case study: A GPR survey on a morainic lake in northern Italy for bathymetry, water volume and sediment characterization. Journal of Applied Geophysics **81**: 48-56
Sawagaki T, Lamsal D, Byers A, Watanabe T. 2012. Changes in surface morphology and glacial lake development of Chamlang South Glacier, eastern Nepal Himalaya, since 1964. Tokyo. Global Environ Res **16**: 83-94
Schwamborn G, Dix J, Bull J, Rachold V. 2002. High-resolution seismic and ground penetrating radar–geophysical profiling of a thermokarst lake in the western Lena Delta, Northern Siberia. Permafrost and Periglacial Processes **13**: 259-269

Sellmann PV, Delaney AJ, Arcone SA. 1992. Sub-bottom surveying in lakes with ground-penetrating radar.
Sneed WA, Hamilton GS. 2007. Evolution of melt pond volume on the surface of the Greenland Ice Sheet. Geophysical Research Letters **34**:
Somos-Valenzuela M, McKinney D, Rounce D, Byers A. 2014. Changes in Imja Tsho in the Mount Everest region of Nepal. The Cryosphere **8**: 1661-1671
Somos-Valenzuela M, McKinney DC, Byers AC, Rounce DR, 2013. Bathymetric survey of Imja Lake, Nepal in 2012. Center for Research in Water Resources, University of Texas at Austin
Thompson S, Benn DI, Mertes J, Luckman A. 2016. Stagnation and mass loss on a Himalayan debris-covered glacier: processes, patterns and rates. Journal of Glaciology: 1-19. DOI: 10.1017/jog.2016.37
Thompson SS, Benn DI, Dennis K, Luckman A. 2012. A rapidly growing moraine-dammed glacial lake on Ngozumpa Glacier, Nepal. Geomorphology **145**: 1-11. DOI: 10.1016/j.geomorph.2011.08.015
Wang W, Gao Y, Anacona PI, Lei Y, Xiang Y, Zhang G, Li S, Lu A. 2015. Integrated hazard assessment of Cirenmaco glacial lake in Zhangzangbo valley, Central Himalayas. Geomorphology. DOI: 10.1016/j.geomorph.2015.08.013
Warren CR, Kirkbride MP. 2003. Calving speed and climatic sensitivity of New Zealand lake-calving glaciers. Annals of Glaciology **36**: 173-178. DOI: 10.3189/172756403781816446
Watanabe T, Kameyama S, Sato T. 1995. Imja glacier dead-ice melt rates and changes in a supra-glacial lake, 1989-1994, Khumbu Himal, Nepal: Danger of lake drainage. Mountain Research and Development: 293-300. DOI: 10.2307/3673805
Watanabe T, Lamsal D, Ives JD. 2009. Evaluating the growth characteristics of a glacial lake and its degree of danger of outburst flooding: Imja Glacier, Khumbu Himal, Nepal. Norsk Geografisk Tidsskrift - Norwegian Journal of Geography **63**: 255-267. DOI: 10.1080/00291950903368367
Wessels RL, Kargel JS, Kieffer HH. 2002. ASTER measurement of supraglacial lakes in the Mount Everest region of the Himalaya. Annals of Glaciology **34**: 399-408. DOI: 10.3189/172756402781817545
Yamada T, Naito N, Kohshima S, Fushimi H, Nakazawa F, Segawa T, Uetake J, Suzuki R, Sato N, Chhetri IK. 2004. Outline of 2002: Research activities on glaciers and glacier lakes in Lunana region, Bhutan Himalayas. Bulletin of Glaciological Research **21**: 79-90
Yamada T, Sharma C. 1993. Glacier lakes and outburst floods in the Nepal Himalaya. IAHS Publications-Publications of the International Association of Hydrological Sciences **218**: 319-330

Synthesis & Conclusion

Observing, quantifying and monitoring spatial and temporal changes occurring within different systems is one of the most important aspects of science. Without these observations, we would have little understanding of the processes controlling dynamic systems, driving rates at which changes occur and we would be limited in our ability to predict future trends. As technology advances, so do the tools we use to perform our measurements and observations. Of course, deciding which tools and techniques to use is often the most important question and is dictated by factors such as cost, efficiency and data quality.

In this dissertation, I have presented the results from four studies, each demonstrating that technological developments and new and innovative applications of techniques can provide significant improvements not only to the spatial extent and quality of observations, but also to the temporal series and thus to our overall ability to detect changes. By taking advantage of techniques and tools such as SfM and GPR, and by applying them to new areas I have advanced knowledge and understanding in two distinct fields. In the subaqueous environment, mapping SCRs and using GPR to see through turbid supraglacial lakes, and in the terrestrial environments, using SfM to extract spatial information from historic datasets, have allowed us to observe these systems in new ways and quantify changes in a more detailed and efficient fashion.

Our application of SfM to the video survey footage of the *Home*, *Hetty Taylor*, and the *Wisconsin* has illustrated that this technique is not only a viable option for mapping and measuring large SCRs, but that the end result yields a highly-valuable dataset containing

detailed geometric information as well as high-resolution orthomosaics (Mertes et al., 2014, Mertes et al., In Review). Considering traditional maritime archaeological surveys often require numerous days in the field, a multitude of divers and rely on individual hand measurements for the production of planimetric site maps (Bass, 1966), using video/photographic surveys acquired by one-two person teams within the duration of a single dive can greatly reduce costs associated with field work and limits the amount of time in which divers are subjected to the harsh subaqueous environment. What's more, 3-D models of these SCRs can be manipulated, viewed from many angles, measured and studied all from an office in a digital environment. Using archival footage as a source, with the exception of the 2015 *Wisconsin* model, has demonstrated the value of SfM in extending our temporal observations, allowing us to extract spatial information from datasets created prior to the development of the SfM technique. Datasets used to generate down-looking mosaics can be used to create a baseline DEM of a SCR as was done with the 2005 *Wisconsin* survey footage. Using this model as a starting point, it was possible to quickly and efficiently gather new data, process it using SfM, and compare it to this earlier survey in order to rapidly quantify spatio-temporal changes occurring due to environmental and anthropogenic effects (e.g. artefact theft, structural damage, colonization of invasive species) (Mertes et al., In Review).

The mapped spatial changes give great insight into how the *Wisconsin* is responding to the effects of the surrounding environment. For instance, many metal SCRs in the Great Lakes have been noted as undergoing inward collapse through time (Thomsen et al., 2014, Zant et al., 2015, Meverden et al., 2016), indeed this was thought to be the case for

the *Wisconsin* (Thomsen and Meverden, 2010), however the DEM differencing illustrates a pattern of outward collapse and deterioration (Mertes et al., In Review). In addition, the orthomosaic generated allows for visual inspection of the SCR and identification of shifting material as well as colonization of mussels.

By using SfM for the rapid creation of SCR models on a regular basis, these datasets can be used by managers to actively monitor rates of deterioration at individual sites and inform conservation efforts. Installation and trilateration of immovable GCP markers around a SCR can also aid managers and archaeologists by making model alignment much easier while potentially helping to improve DEM differencing accuracy.

In the terrestrial environment, we have demonstrated the possibilities of the SfM technique to help fill spatio-temporal gaps in glacier records. For recent years, satellite data offers unparalleled opportunities for observation and monitoring but prior to this, datasets exist that now have potential for use with SfM, such as aerial and terrestrial photos. While the three case study glaciers in Chapter 3 are accessible today and have in the past had sporadic measurements performed on them, there are large gaps in the observation records pertaining to the spatial extent and health of these glaciers.

Although archival imagery may have been acquired for a variety of purposes, e.g. for early topographic map production (i.e. Brøggerhalvøya), terrestrial documentation (i.e. Rhone) or even hand held imagery shot for the purpose of later visual interpretation (i.e. Khumbu), we have successfully extracted high-resolution DEMs of each site. The DEMs

have allowed us to quantify changes that have occurred to these glacier surfaces over the last 40-120 years.

Historical changes in glacier systems have been documented using other methods such as repeated field surveying (e.g. Haefeli, 1962), differencing of more recent remote sensing data (e.g. Kääb et al., 2012, Thompson et al., 2016) and even digitization of early topographic maps (e.g. Nuth et al., 2007, Sugiyama et al., 2007), but in most cases, changes mapped using older data have a much lower spatial or temporal resolution. For example, the digitization of the Svalbard 1936/38 topographic map by Nuth et al. (2007), still only resulted in a DEM with a resolution equal to the contour interval of 50 m. DEM differencing of the Ngozumpa glacier by Thompson et al. (2016) used three high-resolution DEMs, but only covered a period of 5 years from 2010-2015. The time involved in creating topographic maps of whole glaciers at resolutions equal to the DEMs extracted in Chapter 3 would have been unrealistic in the early to mid-20th century. SfM has opened a new door to easily and efficiently extract this crucial information, extending our time series of glacial observations further into the past.

The DEM differencing results show highly contrasting patterns of surface lowering amongst all sites. Most notably is the difference between the heavily debris-covered Khumbu and the clean ice valley glaciers, where the presence of debris has caused more of a downwasting pattern of melt as opposed to terminus retreat. Being able to extend our temporal observation back to these periods provides a more detailed record of past glacier dynamics and response to changes in climate and our observations enhance the record of

spatial change at these sites. Understanding the past trends in glacier changes can help us to predict future outcomes.

Traditional photogrammetric techniques require information of interior and exterior orientation to make data extraction possible (Wolf and Dewitt, 2000) but the SfM technique can be applied without the need for this *a priori* information. The availability of modern high-resolution imagery and DEMs make it possible to acquire GCPs for SfM georeferencing and alignment. What's more, the overall accuracy of resulting models is such that when quantifying the patterns of long term glacier spatial extent, the error and uncertainty is small.

In areas where visual inspection is limited, photographic surveying combined with SfM model extraction does not perform well. Supraglacial lakes, found increasingly on debris-covered glaciers, play a significant role in the glacier response to climate change and can pose significant hazards. The lakes are highly turbid, precluding any kind of visual surveying technique. Yet, very little is known about the subaqueous environment in supraglacial lakes. To date, most supraglacial lake studies have employed weighted line or point-sonar depth measurements which can result in coarsely spaced bathymetric maps with little insight into the composition and spatial distribution of lakebed debris (Kadota, 1994, Chikita, et al., 1999, Benn, et al., 2001, Röhl, 2008, Thompson, et al., 2012). To further our knowledge of the subaqueous system of supraglacial lakes, GPR surveys were performed over the frozen surface of Spillway Lake, Nepal. By using a towable GPR system it was possible to gather densely spaced data within two basins in a matter of minutes, greatly reducing the overall time required to survey a lake in

comparison to point measurements. The data acquired using GPR reveals not only depth information but also information pertaining to the lakebed debris distribution, allowing facies analysis

Unlike freshwater lakes, supraglacial lakes experience drastic spatial changes associated with sub-lake ice melt, shoreline calving and debris transportation and even rapid deepening through subaqueous calving and collapse into relict conduits (Benn et al., 2001, Röhl, 2008, Thompson et al., 2012, Thompson et al., 2016). These processes can lead to deepening, shallowing, redistribution of lakebed debris and possibly exposure of underlying ice. What's more, the rapid expansion of baselevel supraglacial lakes can increase the likelihood of potentially hazardous glacial lake outburst floods.

The results of the facies analysis show varying patterns of debris distribution which can be attributed to both larger scale debris transportation events as well as areas of finer sediment drape coming out of suspension. Identifying similar subaerial sediment packages along the nearby shorelines has strengthened these interpretations and allowed for the conceptualization of a new model for supraglacial lake growth (Mertes et al., 2016). This new model incorporates the established shoreline processes (e.g. calving, backwasting) and transition from perched lake to base-level lake, but it also incorporates the dynamic subaqueous system as well. Changes occurring in this system can have rapid positive or negative feedbacks on the rates and direction of lake growth and deepening with implications for large moraine-dammed lake development, glacial lake outburst risks as well as glacial downwasting rates. Understanding that supraglacial lakebeds are not static, and that the positions of and thickness of debris can change rapidly means that

in order to be able to better predict future trends, detailed surveys using tools such as GPR are invaluable.

Each of the studies presented in this dissertation have successfully applied techniques in innovative new ways or to new systems and datasets, in an attempt to improve our ability to observe and quantify spatio-temporal changes, important in the fields of glaciology and maritime archaeology. The significance of this work is twofold, firstly I have successfully demonstrated new applications of SfM and GPR to glacial and subaqueous systems allowing

1. More efficiently map and measure larger SCR using both archival and recently acquired imagery and the SfM technique.

2. Improve the quality and quantity of data gathered during SCR surveying from a collection of sparse measurements to higher-resolution surface models.

3. Unlock the past through the use of historic glacial imagery which had only previously been used for lower resolution spatial information.

4. Demonstrate the effectiveness of using GPR for the mapping of base-level supraglacial lakes on debris-covered glaciers.

Secondly, the successful application of these techniques provided the opportunity to make interesting contributions in understanding change in both glacial and subaqueous systems through

1. Quantifying the spatio-temporal changes occurring on larger SCRs in such a way that could be implemented in many monitoring programs throughout the world.

2. Improving our understanding of the subaqueous environment on supraglacial lakes, thereby adding to the knowledge of lake growth and lakebed dynamics.

3. Updating the conceptual model of supraglacial lake growth to include dynamic lakebed changes which is a crucial factor which needs incorporation into lake growth modelling.

4. Successfully quantifying long-term glacier surface lowering trends on a multitude of glaciers from numerous geographic regions, illustrating the drastic differences between climatic responses between clean-ice and debris-covered glaciers.

Further development and improvement of the techniques used will allow for a more complete understanding of the processes controlling observed changes. In addition, the nature of the resulting datasets (i.e. 3-D models, radargrams) can not only be used for scientific purposes, but also for better visualization and display for funding agencies, government and public outreach.

References

Bass GF. 1966. Archaeology under water. Frederick A. Praeger: New York
Benn DI, Wiseman S, Hands KA. 2001. Growth and drainage of supraglacial lakes on debrismantled Ngozumpa Glacier, Khumbu Himal, Nepal. Journal of Glaciology **47**: 626-638. DOI: 10.3189/172756501781831729
Haefeli R. 1962. The ablation gradient and the retreat of a glacier tongue. IASH Publication **58**: 49-59
Kääb A, Berthier E, Nuth C, Gardelle J, Arnaud Y. 2012. Contrasting patterns of early twenty-first-century glacier mass change in the Himalayas. Nature **488**: 495-498. DOI: 10.1038/nature11324
Mertes J, Thomsen T, Gulley J. 2014. Evaluation of Structure from Motion Software to Create 3D Models of Late Nineteenth Century Great Lakes Shipwrecks Using Archived Diver-Acquired Video Surveys. Journal of Maritime Archaeology **9**: 173-189. DOI: 10.1007/s11457-014-9132-x
Mertes JR, Thompson SS, Booth AD, Gulley JD, Benn DI. 2016. A conceptual model of supra-glacial lake formation on debris-covered glaciers based on GPR facies analysis. Earth Surface Processes and Landforms: n/a-n/a. DOI: 10.1002/esp.4068
Mertes JR, Zant CN, Gulley JD, Thomsen TL. In Review. Rapid, quantitative assessment of submerged cultural resource degradation using repeat video surveys and Structure from Motion. Journal of Maritime Archaeology:
Meverden KN, Thomsen TL, Zant CN, 2016. Senator Shipwreck (steam screw). In *In National register of historic places nomination form. Manuscript on file.* Wisconsin Historical Society: Division of Historic Preservation and Public History: Madison, Wisconsin
Nuth C, Kohler J, Aas HF, Brandt O, Hagen JO. 2007. Glacier geometry and elevation changes on Svalbard (1936-90): a baseline dataset. Annals of Glaciology **46**: 106-116. DOI: 10.3189/172756407782871440
Röhl K. 2008. Characteristics and evolution of supraglacial ponds on debris-covered Tasman Glacier, New Zealand. Journal of Glaciology **54**: 867-880. DOI: 10.3189/002214308787779861
Sugiyama S, Bauder A, Zahno C, Funk M. 2007. Evolution of Rhonegletscher, Switzerland, over the past 125 years and in the future: application of an improved flowline model. Annals of Glaciology **46**: 268-274
Thompson S, Benn DI, Mertes J, Luckman A. 2016. Stagnation and mass loss on a Himalayan debris-covered glacier: processes, patterns and rates. Journal of Glaciology: 1-19. DOI: 10.1017/jog.2016.37
Thompson SS, Benn DI, Dennis K, Luckman A. 2012. A rapidly growing moraine-dammed glacial lake on Ngozumpa Glacier, Nepal. Geomorphology **145**: 1-11. DOI: 10.1016/j.geomorph.2011.08.015
Thomsen T, Meverden K, 2010. Wisconsin Shipwreck (steam screw). In *National register of historic places nomination form. Manuscript on file.* Wisconsin Historical Society: Division of Historic Preservation and Public History: Madison, Wisconsin

Thomsen T, Reckner P, Stout M, 2014. Lakeland Shipwreck (steam screw). In *In National register of historic places nomination form. Manuscript on file.* Wisconsin Historical Society: Division of Historic Preservation and Public History: Madison, Wisconsin

Wolf PR, Dewitt BA. 2000. Elements of Photogrammetry: with applications in GIS. McGraw-Hill New York

Zant CN, Thomsen TL, Reckner P, Stout M, 2015. Milwaukee Shipwreck (steam screw). In *In National register of historic places nomination form. Manuscript on file.* Wisconsin Historical Society: Division of Historic Preservation and Public History: Madison, Wisconsin

Appendix A: Permission to use copyrighted materials

This letter is for Chapter 1.

SPRINGER LICENSE
TERMS AND CONDITIONS

Jan 24, 2017

This Agreement between Jordan R Mertes ("You") and Springer ("Springer") consists of your license details and the terms and conditions provided by Springer and Copyright Clearance Center.

License Number	4035241085961
License date	Jan 24, 2017
Licensed Content Publisher	Springer
Licensed Content Publication	Journal of Maritime Archaeology
Licensed Content Title	Evaluation of Structure from Motion Software to Create 3D Models of Late Nineteenth Century Great Lakes Shipwrecks Using Archived Diver-Acquired Video Surveys
Licensed Content Author	J. Mertes
Licensed Content Date	Jan 1, 2014
Licensed Content Volume Number	9
Licensed Content Issue Number	2
Type of Use	Thesis/Dissertation
Portion	Full text
Number of copies	5
Author of this Springer article	Yes and you are the sole author of the new work
Order reference number	
Title of your thesis / dissertation	Novel Methods for Quantifying Spatio-temporal Change in Glaciated and Subaqueous Environments
Expected completion date	Mar 2017
Estimated size(pages)	190
Requestor Location	Jordan R Mertes 3461 S. Lake Miltona Dr. NE MILTONA, MN 56354 United States Attn: Jordan R Mertes
Billing Type	Invoice
Billing Address	Jordan R Mertes 3461 S. Lake Miltona Dr. NE MILTONA, MN 56354 United States Attn: Jordan R Mertes
Total	0.00 USD
Terms and Conditions	

established by these terms and conditions and those established by CCC's Billing and Payment terms and conditions, these terms and conditions shall control.
Jurisdiction
All disputes that may arise in connection with this present License, or the breach thereof, shall be settled exclusively by arbitration, to be held in the Federal Republic of Germany, in accordance with German law.
Other conditions:
V 12AUG2015

This letter is for Chapter 4.

JOHN WILEY AND SONS LICENSE TERMS AND CONDITIONS

Jan 24, 2017

This Agreement between Jordan R Mertes ("You") and John Wiley and Sons ("John Wiley and Sons") consists of your license details and the terms and conditions provided by John Wiley and Sons and Copyright Clearance Center.

License Number	4035240818289
License date	Jan 24, 2017
Licensed Content Publisher	John Wiley and Sons
Licensed Content Publication	Earth Surface Processes and Landforms
Licensed Content Title	A conceptual model of supra-glacial lake formation on debris-covered glaciers based on GPR facies analysis
Licensed Content Author	Jordan R. Mertes,Sarah S. Thompson,Adam D. Booth,Jason D. Gulley,Douglas I. Benn
Licensed Content Date	Nov 29, 2016
Licensed Content Pages	1
Type of use	Dissertation/Thesis
Requestor type	Author of this Wiley article
Format	Print and electronic
Portion	Full article
Will you be translating?	No
Title of your thesis / dissertation	Novel Methods for Quantifying Spatio-temporal Change in Glaciated and Subaqueous Environments
Expected completion date	Mar 2017
Expected size (number of pages)	190
Requestor Location	Jordan R Mertes 3461 S. Lake Miltona Dr. NE MILTONA, MN 56354 United States Attn: Jordan R Mertes
Publisher Tax ID	EU826007151
Billing Type	Invoice
Billing Address	Jordan R Mertes 3461 S. Lake Miltona Dr. NE MILTONA, MN 56354 United States Attn: Jordan R Mertes
Total	0.00 USD
Terms and Conditions	

TERMS AND CONDITIONS

("Marks") of WILEY or its licensors is granted hereunder, and you agree that you shall not assert any such right, license or interest with respect thereto

- NEITHER WILEY NOR ITS LICENSORS MAKES ANY WARRANTY OR REPRESENTATION OF ANY KIND TO YOU OR ANY THIRD PARTY, EXPRESS, IMPLIED OR STATUTORY, WITH RESPECT TO THE MATERIALS OR THE ACCURACY OF ANY INFORMATION CONTAINED IN THE MATERIALS, INCLUDING, WITHOUT LIMITATION, ANY IMPLIED WARRANTY OF MERCHANTABILITY, ACCURACY, SATISFACTORY QUALITY, FITNESS FOR A PARTICULAR PURPOSE, USABILITY, INTEGRATION OR NON-INFRINGEMENT AND ALL SUCH WARRANTIES ARE HEREBY EXCLUDED BY WILEY AND ITS LICENSORS AND WAIVED BY YOU.

- WILEY shall have the right to terminate this Agreement immediately upon breach of this Agreement by you.

- You shall indemnify, defend and hold harmless WILEY, its Licensors and their respective directors, officers, agents and employees, from and against any actual or threatened claims, demands, causes of action or proceedings arising from any breach of this Agreement by you.

- IN NO EVENT SHALL WILEY OR ITS LICENSORS BE LIABLE TO YOU OR ANY OTHER PARTY OR ANY OTHER PERSON OR ENTITY FOR ANY SPECIAL, CONSEQUENTIAL, INCIDENTAL, INDIRECT, EXEMPLARY OR PUNITIVE DAMAGES, HOWEVER CAUSED, ARISING OUT OF OR IN CONNECTION WITH THE DOWNLOADING, PROVISIONING, VIEWING OR USE OF THE MATERIALS REGARDLESS OF THE FORM OF ACTION, WHETHER FOR BREACH OF CONTRACT, BREACH OF WARRANTY, TORT, NEGLIGENCE, INFRINGEMENT OR OTHERWISE (INCLUDING, WITHOUT LIMITATION, DAMAGES BASED ON LOSS OF PROFITS, DATA, FILES, USE, BUSINESS OPPORTUNITY OR CLAIMS OF THIRD PARTIES), AND WHETHER OR NOT THE PARTY HAS BEEN ADVISED OF THE POSSIBILITY OF SUCH DAMAGES. THIS LIMITATION SHALL APPLY NOTWITHSTANDING ANY FAILURE OF ESSENTIAL PURPOSE OF ANY LIMITED REMEDY PROVIDED HEREIN.

- Should any provision of this Agreement be held by a court of competent jurisdiction to be illegal, invalid, or unenforceable, that provision shall be deemed amended to achieve as nearly as possible the same economic effect as the original provision, and the legality, validity and enforceability of the remaining provisions of this Agreement shall not be affected or impaired thereby.

- The failure of either party to enforce any term or condition of this Agreement shall not constitute a waiver of either party's right to enforce each and every term and condition of this Agreement. No breach under this agreement shall be deemed waived or excused by either party unless such waiver or consent is in writing signed by the party granting such waiver or consent. The waiver by or consent of a party to a breach of any provision of this Agreement shall not operate or be construed as a waiver of or consent to any other or subsequent breach by such other party.

- This Agreement may not be assigned (including by operation of law or otherwise) by you without WILEY's prior written consent.

- Any fee required for this permission shall be non-refundable after thirty (30) days from receipt by the CCC.
- These terms and conditions together with CCC's Billing and Payment terms and conditions (which are incorporated herein) form the entire agreement between you and WILEY concerning this licensing transaction and (in the absence of fraud) supersedes all prior agreements and representations of the parties, oral or written. This Agreement may not be amended except in writing signed by both parties. This Agreement shall be binding upon and inure to the benefit of the parties' successors, legal representatives, and authorized assigns.
- In the event of any conflict between your obligations established by these terms and conditions and those established by CCC's Billing and Payment terms and conditions, these terms and conditions shall prevail.
- WILEY expressly reserves all rights not specifically granted in the combination of (i) the license details provided by you and accepted in the course of this licensing transaction, (ii) these terms and conditions and (iii) CCC's Billing and Payment terms and conditions.
- This Agreement will be void if the Type of Use, Format, Circulation, or Requestor Type was misrepresented during the licensing process.
- This Agreement shall be governed by and construed in accordance with the laws of the State of New York, USA, without regards to such state's conflict of law rules. Any legal action, suit or proceeding arising out of or relating to these Terms and Conditions or the breach thereof shall be instituted in a court of competent jurisdiction in New York County in the State of New York in the United States of America and each party hereby consents and submits to the personal jurisdiction of such court, waives any objection to venue in such court and consents to service of process by registered or certified mail, return receipt requested, at the last known address of such party.

WILEY OPEN ACCESS TERMS AND CONDITIONS

Wiley Publishes Open Access Articles in fully Open Access Journals and in Subscription journals offering Online Open. Although most of the fully Open Access journals publish open access articles under the terms of the Creative Commons Attribution (CC BY) License only, the subscription journals and a few of the Open Access Journals offer a choice of Creative Commons Licenses. The license type is clearly identified on the article.

The Creative Commons Attribution License

The Creative Commons Attribution License (CC-BY) allows users to copy, distribute and transmit an article, adapt the article and make commercial use of the article. The CC-BY license permits commercial and non-

Creative Commons Attribution Non-Commercial License

The Creative Commons Attribution Non-Commercial (CC-BY-NC)License permits use, distribution and reproduction in any medium, provided the original work is properly cited and is not used for commercial purposes.(see below)

Creative Commons Attribution-Non-Commercial-NoDerivs License

The Creative Commons Attribution Non-Commercial-NoDerivs License (CC-BY-NC-ND) permits use, distribution and reproduction in any medium, provided the original work is properly cited, is not used for commercial purposes and no modifications or adaptations are made. (see below)

Use by commercial "for-profit" organizations

This letter is for use of aerial images from Toposvalbard in figure 3.2.

From: Harald Faste Aas
Sent: Monday, March 7, 2016 12:09 PM
To: Jordan Robert Mertes
Cc: Sara Mollie Cohen
Subject: RE: Toposvalbard 1936 Aerials

Hi Jordan

The online images available on TopoSvalbard has generated and stored as cashed-data. This is why you can zoom in to full resolution very quickly. If you can use them 'as is' you are welcome to include them as basement for you research work as well, but I guess you also want to use some images as illustrations in articles or reports as well? If so, that is OK as long as you use the publication terms that are presented in the contract with UNIS and NP. Please see the extraction from this contract below (in Norwegian only).

If you need to receive full resolution files/copies, this will initiate some preparation work and therefore we have a price of 500 NOK for preparation of delivery that takes less than 1 hour work. For 1 hour work or more we take NOK 995,- per hour. If you want to order lets, say 10 images, I could easily prepare them and add them to download for 500 NOK. If you need 50 or even 100 images, I will need more time for preparation as I need to chop up the delivery into handy blocks of files - or in worst case, send it on a disk (the price of the disk will be added). Conversion to jpg-format is possible if wanted – makes the file size more handy. Just check out your needs and I will try to calculate a price when I have an idea of the what you want to order. Final order should be done through Sara.

Any images that are not yet scanned needs scanning first and today the price will be near 200 NOK per images with a starting price of near 1200 NOK for the first images. This is calculated based on the time needed for scanning the images.

Hope this answer helps you a bit ☺

Best regards

Harald F. Aas

G. Publiseringsbetingelser.

G.1. Flybildene eller utsnitt av flybildene kan publiseres eller gjengis i vitenskapelige artikler, rapporter og lignende, eller annen form for offentlig visning, som er relatert til kurs- eller forskningsprogrammet på UNIS. Publisering/gjengivelse (utgitt som PDF eller lignende) må ha en oppløsning som er begrenset til det aktuelle formålet. F.eks. bør et flybilde eller utsnitt av dette ikke dekke mer enn en A4 side med oppløsning på maks 200 dpi.

Ved publisering eller annen form for offentlig visning skal Norsk Polarinstitutt og flybildets referansenummer oppgis sammen med fotografiet. Hvis det dreier seg om utsnitt må dette også oppgis. Eksempel: "Utsnitt av flybilde S90 3682, © Norsk Polarinstitutt"

G.2. For publisering på Internett eller Intranett skal aktuell illustrasjon maks være 700x700 piksler, enten for hele bildet eller aktuelt utsnitt. URL skal sendes til kartseksjonen på Norsk Polarinstitutt.

Permission to use Google Earth printed map in Chapter 2.

https://www.google.co.uk/permissions/geoguidelines.html#maps-print

USES IN PRINT

Google Maps and Google Earth have built-in print functionality. You may print Content for non-commercial use and enlarge it (for example, a map with directions). In all uses where you will distribute printed materials that include the Content, first make sure that you read the general guidelines above, especially with regard to fair use and attribution.

Proposed use	OK to use?	Additional information
Books	Yes	It's fine to use a handful of images, as long as you're not distributing more than 5,000 copies or using the Content in guidebooks.
Periodicals	Yes	This includes newspapers, magazines and journals.
Reports and presentations	Yes	This includes research papers, internal reports, presentations, proposals and other related professional documents.
Guidebooks	No	You may not use the Content as a core part of printed navigational material (for example, tour books).
Consumer goods	No	This includes retail products or retail product packaging (for example, t-shirts, beach towels, shower curtains, mugs, posters, stationery, etc.).
Print advertisements	No	See the advertisements section for more guidance on digital and TV uses.

Permission to use shipwreck maps and historical images in Chapters 1 & 2 i.e. Figures 1.1 and 2.2

From: TAMARA L THOMSEN
Sent: Thursday, March 30, 2017 6:43 PM
To: jrmertes@mtu.edu
Subject:

I, Tamara Thomsen, archaeologist with Wisconsin Historical Society Maritime Preservation and Archaeology Program, permit use of shipwreck site plans for the schooners *Hetty Taylor* and *Home,* as well as historic and underwater images of shipwrecks including the steamship Wisconsin to published by Jordan Mertes in his dissertation and used in associated programs, presentations, publications related to the collaborative work with our office.

Tamara Thomsen
Maritime Archaeologist

State Historic Preservation Office

Wisconsin Historical Society
523 Atlas Ave., Madison, WI 53714
608.221.5909 (Office), 608.221.5902 (FAX)

tamara.thomsen@wisconsinhistory.org

WisconsinShipwrecks.org

Wisconsin Historical Society

Collecting, Preserving, and Sharing Stories Since 1846